INFLUENCE OF THERMO-MECHANICAL TREATMENT AND LASER SURFACE MODIFICATION ON CORROSION BEHAVIOUR OF 7075 ALUMINUM ALLOY

A Thesis submitted in the partial fulfillment of the requirements for

the award of the degree of

DOCTOR OF PHILOSOPHY

By

A.C. UMA MAHESHWER RAO

(Roll No. 701209)

Under the supervision of

Dr. K.V.SAI SRINADH
Professor, Mechanical Engineering
Department, National Institute of
Technology Warangal.

Dr. V.VASU
Assistant Professor, Mechanical
Engineering Department, National
Institute of Technology Warangal.

DEPARTMENT OF MECHANICAL ENGINEERING

NATIONAL INSTITUTE OF TECHNOLOGY

WARANGAL (T.S) INDIA 506 004

JANUARY 2017

NATIONAL INSTITUTE OF TECHNOLOGY
WARANGAL (T.S) INDIA 506 004

CERTIFICATE

This is to certify that the thesis entitled **"Influence of Thermo-mechanical Treatment and Laser Surface Modification on Corrosion Behavior of 7075 Aluminum Alloy"** that is being submitted by **Mr. A.C. Uma Maheshwer Rao** in partial fulfillment for the award of Doctor of Philosophy (**Ph.D**) in the Department of Mechanical Engineering, National Institute of Technology, Warangal, is a record of bonafide work carried out by him under my guidance and supervision. The results of embodied in this thesis have not been submitted to any other Universities or Institutes for the award of any degree or diploma.

Dr. K.V.SAI SRINADH

Professor, Mechanical Engineering Department, National Institute of Technology Warangal.

Dr. V.VASU

Assistant Professor, Mechanical Engineering Department, National Institute of Technology Warangal.

DECLARATION

This is to certify that the work presented in the thesis entitled **"Influence of Thermo-mechanical Treatment and Laser Surface Modification on Corrosion Behavior of 7075 Aluminum Alloy"**, is a bonafied work done by me under the supervision of Prof. K.V. SAI SRINADH and Dr.V.VASU was not submitted elsewhere for the award of any degree.

I declare that this written submission represents my idea in my own words and where other's ideas or words have not been included. I have adequately cited and referenced the original sources. I also declare that I have adhered to all principles of academic honesty and integrity and have not misinterpreted or fabricated or falsified any idea/data/fact/source in my submission. I understand that any violation of the above will be a cause for disciplinary action by the Institute and can also evoke penal action from the sources which have thus not been properly cited or from whom proper permission has not taken when needed.

Date: **(A.C.Uma maheshwer Rao)**

Place: Warangal   Research Scholar,

                                                                       Roll No.701209

This thesis is dedicated to

my mother Smt. **Hemalatha** and my beloved friend **Pradeep** who are

heaven abode. They still live in my heart and hope I have made them

proud.

ACKNOWLEDGEMENT

Abstract

The 7075 Aluminum alloys are widely used as structural material in aerospace and engineering industries due to their inherent attractive properties such as high-strength-to-weight ratio coupled with ductility, toughness and fatigue resistance. Unfortunately, many-a-times, these alloys are prone to surface degradation and suffer localized corrosion under ambient conditions of use due to presence of detrimental coarse constituent particles in grains as well as grain boundaries of the bulk microstructure. To overcome the problem of localized corrosion, thermo-mechanical treatments and laser surface modification has been carried out in this work. In thermo-mechanical treatment, full-annealed 7075 Aluminum alloy undergoes series of deformation through cold rolling and was further subjected to final annealing with various temperatures. The corrosion properties were evaluated through the slow strain rate test (SSRT) and potentiodynamic polarization tests carried out in 3.5% NaCl solution with pH of 12. In laser surface modifications (LSM), the surface of 7075 Aluminum alloy was modified with the application of High power diode laser (HPDL). LSM has become a powerful tool to modify the surface by rapidly melting near surface layer by conduction and thereby producing a high degree homogeneous and refined microstructure in short duration without affecting the bulk. The HPDL system capable of producing large sized beam which can eliminate overlapping of laser tracks. Further, it can effectively avoid detrimental effects of overlapped regions and thereby enhance structural homogeneity in re-solidified layer and thereby reduce SCC and pitting corrosion effects. The LSM was carried out with various laser energy densities in the range of 80 J/mm^2 to 200 J/mm^2 and corrosion properties were evaluated by carrying out potentiodynamic polarization and electrochemical impedance spectroscopy (EIS) tests.

The results for the thermo-mechanically treated samples revealed that the sample with high cold reduction and annealed at high temperatures has the high corrosion resistance both in SSRT and potentiodynamic polarization tests. The high dislocation density generated in the matrix during cold rolling and the transformation of fine Ɲ' phase into coarser phases on subsequent annealing along the grain boundary attributed to enhanced corrosion resistance. In addition, the XRD and SEM –EDAX revealed that the corrosion products such as Cu_2O and

MgO are observed, which improved the corrosion resistance by providing effective barrier from further corrosion attack.

In the laser surface modification, the re-solidified laser-melted layer got refined with elimination of detrimental Al-Cu-Fe constituent particles and grain boundary network present in wrought structure. The comparative corrosion study determined by Potentiodynamic Polarization measurements in 3.5 % sodium chloride solution showed reduced corrosion current in laser melted surface specimen compared to untreated specimen. Elimination of coarse constituent particles in refined melted microstructure indeed provided adequate protection against corrosion attack at particle-matrix boundaries. Electrochemical impedance measurements taken during the corrosion test showed high film resistance in laser melted layer as compared to untreated substrate specimen. Unfortunately, it was observed that in LSM surface hardness was reduced in melted region as compared to that of untreated substrate owing to reduction in hard constituent particles in microstructure. In order to enhance the surface hardness and maintaining corrosion resistance, laser surface cladding with various powders such as graphite, Al_2O_3 and B_4C has been carried out. It has been observed that the hardness has been increased as compared with the LSM samples and corrosion properties are well maintained.

Due to high coupling efficiency of HPDL with aluminum alloys, the temperature evolutions in the sample were hard to measure during experimentation. Using computer simulations the melt depth, temperature developed with various laser intensities and residual stresses generated were predicated and are validated with the experimental results. The theoretical model produced is shown to give a reasonable prediction of melt pool shape and can be usefully employed to help optimize overlap required for laser surface processing applications.

TABLE OF CONTENTS

CHAPTER 3   **Experimentation**

LIST OF FIGURES

work.

LIST OF TABLES

LIST OF ABBREVIATIONS

Abbreviations	Description
AA	Aluminum alloy
AD	Anodic dissolution
AIDE	Adsorption induced dislocation emission
AL	Aluminum
Al_2O_3	Aluminium oxide
Br	Bromine
BSI	Backscattered image
CELP	Corrosion enhanced localized plasticity
CF	Corrosion fatigue
Cr	Chromium
CO_2	Carbon dioxide
Cu	Copper
CW	Cold worked.
DCB	Double cantilever beam
e^-	Electron
e	Engineering strain
EAC	Environmental assisted cracking
E_{air}	Elongations of the samples tested in the air
EDS	Energy dispersive spectrometry
EB	Electron beam
E_{sol}	Elongations of the samples tested in the solution

Ecorr	Corrosion potential
EIC	Envirnomental induced cracking
Er,	Erbium
Fe	Iron
FSW	Friction stir welding
GBP	Grain boundary precipitates
GMA	Gas metal arc
GP zones	Guinier–preston zone
GTA	Gas tungsten arc
HAZ	Heat-affected zone
HELP	Hydrogen enhanced localized plasticity
HEDE	Hydrogen enhanced decohesion
HPDL	High power diode lasers
HIC	Hydrogen-induced cracking
Hv	Micro hardness
I	Iodine
Icorr	Corrosion curruent
kW	Kilo watt
LB	Laser beam
LSM	Laser surface melting
Li	Lithium
K	Strength coeeficient

KI$_{SCC}$	Stress intensity factor
Mg	Magnisium
MMC	Metal maatrix composites
MPY	Mils per inch
n	Strain hardening exponent
NaCl	Sodium chloride
Nd YAG	*Neodynium* -yttrium-aluminum-garnet lasers
O- tempered	Full annealed
PA	Plasma arc
pH	Potential of hydrogen
PFR	Passive film rupture
P.F.Z	Precipitate free zone
ReX	Recrystallization
RRA	Retrogression and reaging
s	Engineering stress
SC	Scandium
SCC	Stress corrosion cracking
SEI	Secondary electron image
SEM	Scanning electron microscope
SM	Starting materail
SSRT	Slow strain rate test
TMT	Thermo–mechanical treatments
TMZ	Thermomechanically affectedzone
T6	Solution heat treated then artificially aged.

T651	Solution heat treated, stress-relieved by stretching and arificially aged
T7	Over aging temper
UTS	Ultimate tensile strength
W	Watt
XRD	X- ray diffraction
Yb	Ytterbium
ys	Yeild strength
Z	Smooth heaviside function
Zr	Zirconium
Zn	Zinc
ε	True strain
σ	True stress
μm	Micro meter

CHAPTER 1

Introduction

1.1 Introduction

High strength 7075 aluminum alloy in peak aged condition is generally used in high stress bearing structures in aircraft and engineering applications owing its high strength-to-weight-ratio property. Regrettably, the material is highly susceptible for pitting corrosion and other modes of cracking associated with stress corrosion and intergranular corrosion when immersed in chloride medium [1, 2]. The alloying elements such as Zinc, magnesium, iron and copper can have great influences on the corrosion behavior of the alloy [3, 4]. The 7075-T6 Aluminum alloy contains number of intermetallic particles which are deliberately added, either to improve the mechanical properties or present as impurities that can contribute to corrosion such as pitting corrosion or intergranular corrosion attack [5, 6]

As a result, usage of the alloy under such severe environmental conditions restricts in many applications. Although, 7075 Al-alloy under peak-aged condition imparts maximum improvement in strength, degradation in resistance to stress corrosion cracking (SCC) was found to invariably occur**.** Additionally, some reports [7] on imparting other treatments also indicated improvement in resistance to SCC with enhanced strength, but at the expense reduction in fatigue life. Many researches [8] attempted alternative surface modification techniques like shock peening, re-aging and a combination of methods and obtained mixed results. Although such modified surfaces imparted significant reduction in SCC owing to diffusion acceleration associated with dislocations, attaining homogeneous structural integrity was found to be essential for corrosion protection. In some cases [9], SCC resistance improved by virtue of reduction in size and inter-particle distance of grain boundary precipitates (GBP) observed in the modified microstructures. However, maintaining structural integrity is still an obstacle to improve its corrosion resistance in conjunction with strength so that the material could be used in more economical aircraft designs.

It is well known that 7075 Al-alloy microstructure, depending on the treatment conditions, generally contain two different types of constituent particles, one such type consist of Fe, Cu, Si and Mn which are cathodic to Al-matrix. Constituent particles such as Al, Mg and Zn which are

anodic with respect to the matrix and readily dissolve whereas constituent particles cathodic to the matrix promote dissolution and as a result giving rise to galvanic effect and hence corrosion pits can readily develop at these particle interfaces [9]. Although, wide varieties of heat treatments are available for reducing the corrosion rates by virtue of their ability to resist hydrogen embrittlement and vast reduction in galvanizing effects, more often they are accompanied by a loss in strength of about 10 to 15 % owing to coarsening of the precipitates associated with their prolonged treatment schedules.

1.2   Stress-Corrosion Cracking (SCC)

Stress Corrosion Cracking (SCC) is degradation or crack process that occurs in susceptible alloys such as in certain Al alloys and in steels, and occurs when three situation must simultaneously present, namely, the elements of the material alloy must be susceptible to SCC, the tensile stresses should be higher than some threshold value and a particular crack-promoting surroundings environment .This failure occurs in potentially susceptible structural alloys and under service conditions, which can result, often without any prior warning, and leads to catastrophic failure.

The main factor, which has vital effect on the SCC behavior, is the alloy composition. The composition of the material affects the formation and stability of a protecting film on the surface of the alloy. In addition, these alloying elements may influence the strength, grain boundaries, grain size and orientation, grain-boundary segregation, and residual stresses within the material.

SCC takes place in aggressive environment such as in aqueous Cl^-, Br^- and I^- solutions and also in moist air and distill water. The environmental parameters must be in specific ranges for cracking to occur. The environmental parameters are temperature, pH, electrochemical potential, solute species, solute concentration and oxygen concentration. To activate SCC a critical threshold stress must be present. This critical threshold stress may be considered as internal stress or residual stress or external stress. The SCC process consists of two different

phenomenon that are crack initiation and crack propagation. The cracking rate is strongly reliant on the applied stress intensity throughout the crack propagation stage, and can be further divided in to three different stages, as illustrated in Figure 1.1.

During the crack initiation stage in the material, stress intensity or mechanical stress and corrosion environment interacts with each other until the local conditions at the crack tip region reach a critical state that promotes the propagation of cracks. This stage is usually known as "incubation period" and related with a period of time with no apparent crack growth [10]. Usually surface discontinuities and corrosion pits are the main cause for the SCC initiation which is illustrated in Figure 1.2 [11].

SCC initiated form surface discontinuities such as laps, grooves, burrs and cracking of inclusions resulting from machining or fabrication process, as well as pre-existing cracks and grain boundaries that have significantly different electrochemical properties as the bulk material. SCC can also initiate from pits formed due to corrosion, where the local environment within the pits can be much harsher compared with the bulk environment, reducing the protective effect of oxide films and promoting the transition from crack initiation to crack propagation. This type of crack initiation was further discussed by many other researchers [12].
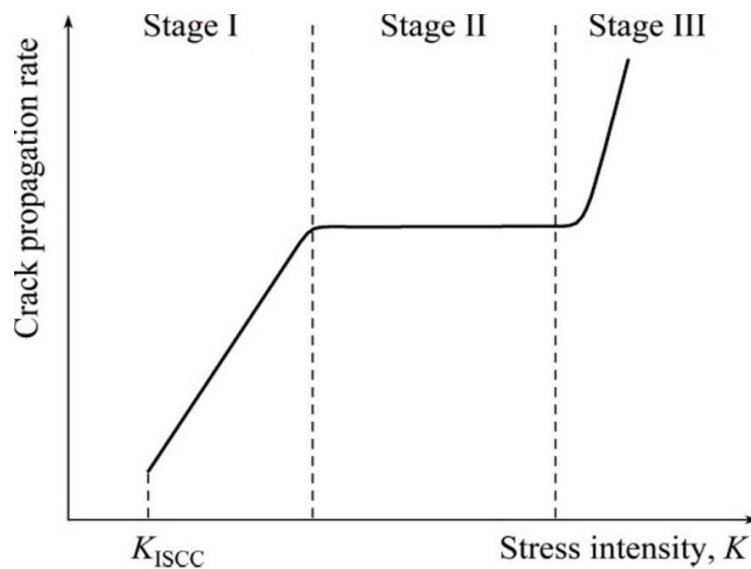
Figure 1.1: Three stages of stress corrosion crack propagation.
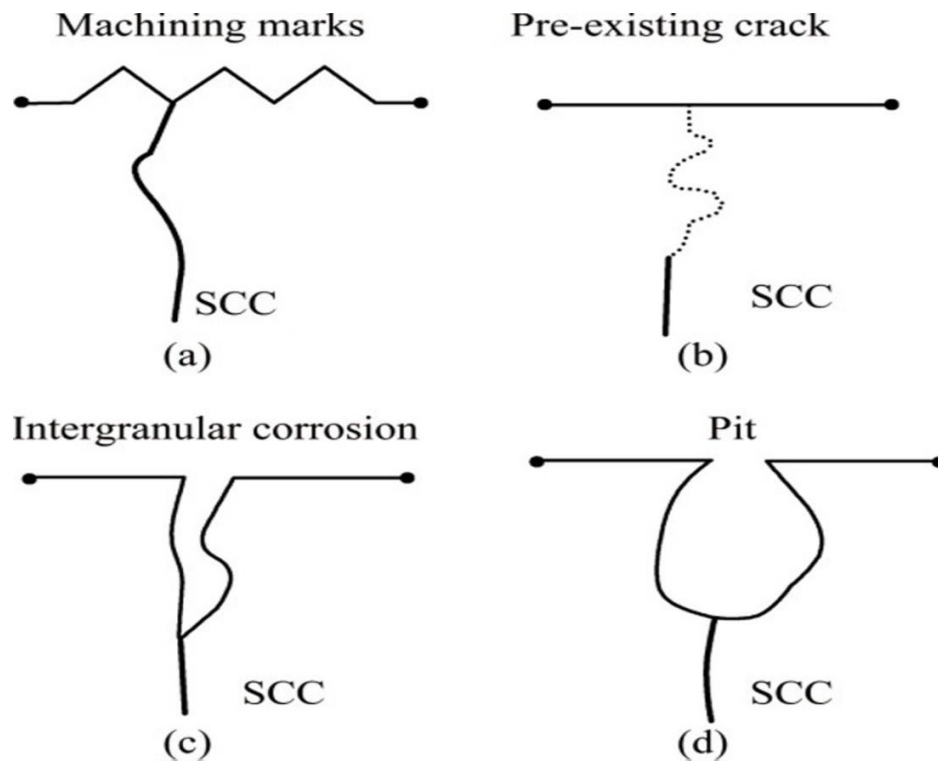
Figure 1.2: Two types of crack initiation sites. (a), (b), and (c) various types of surface discontinuities; (d) pit.

When the stress corrosion crack starts to propagate, the cracking rate becomes dependent on the applied stress intensity. However, based on strong changes in the stress intensity dependence, the cracking rate vs. stress intensity graph consists of three distinct stages, Stage I, II, and III, respectively. As shown in Fig. 1.1, in Stage I crack propagation, when the stress intensity is higher than the threshold value K_{ISCC}, the crack propagation rate has large stress intensity dependence and can be approximated by an exponential function, i.e. a straight line in a logarithmic-linear plot. The crack propagation enters Stage II at higher stress intensity levels. In this stage, the crack rate is freelance of the applied stress intensity and is usually represented as a "plateau". There are many other factors that can affect this "plateau" crack propagation rate, such as loading mode (Mode I or Mode III), chemistry of the corrosive solution, electrochemical potential, and relative humidity [13]. When the stress intensity becomes even higher, the crack

propagation rate becomes stress intensity dependent again. However, cracking at this stage is more related to mechanical fracture rather than SCC.

They are many SCC mechanisms, which ultimately lead to failure. Until now, the reported SCC mechanisms are hydrogen enhanced localized plasticity (HELP), film induced cleavage, hydride formation, slip dissolution, hydrogen enhanced decohesion (HEDE), corrosion enhanced localized plasticity (CELP) and adsorption induced dislocation emission (AIDE). The specific mechanism that is operative depends on the type of material, environment, and loading conditions. Most of the researchers reported that SCC mechanisms in high strength Al-alloys are hydrogen induced cracking [14, 15] anodic dissolution assisted cracking and passive film rupture as shown in figure.1.3 [16-18].
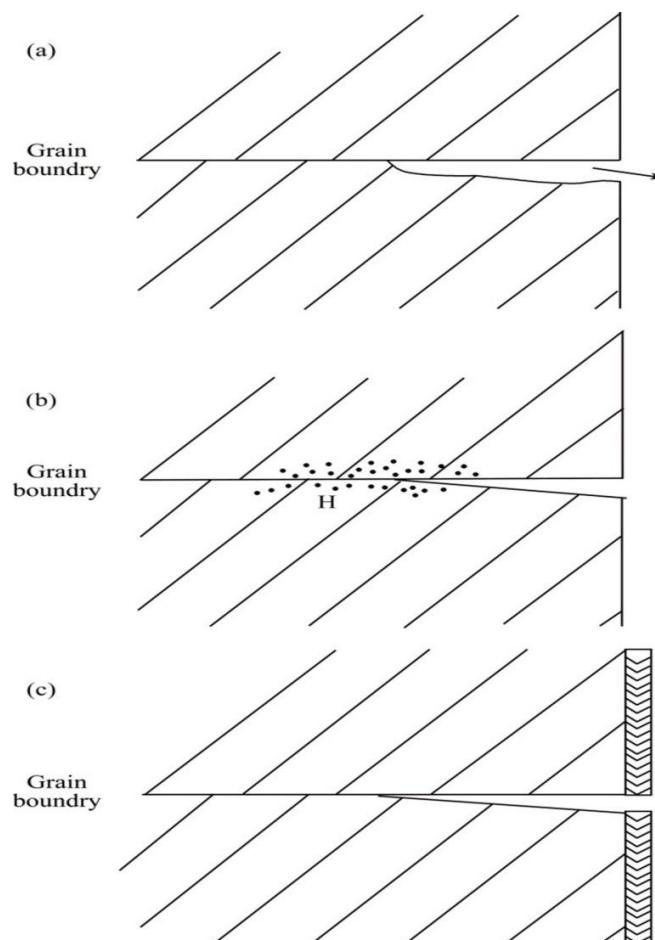
Figure 1.3. Illustration of mechanisms of SCC for aluminum alloys [16].

Hydrogen induced cracking: - As small size of the hydrogen ion can pass into the lattice sites of the material alloy in both gaseous phases and aqueous phases. In an aqueous phase where corrosion reactions take place, both anodic and corresponding cathodic reactions occur. In many cases, hydrogen ion reduction is the cathodic reaction where hydrogen atoms are formed on the surface. On the other hand, hydrogen atoms combine to form hydrogen gas, other hydrogen atoms remain adsorbed to the surface. Because of the high partial hydrogen pressure there exists a driving force for the hydrogen atoms to be absorbed into the lattice casing embrittling the lattices leading to intergranular failure. Al-Zn-Mg-Cu-Zr alloy underwent hydrogen embrittlement even in laboratory air (having a relative humidity of ~50%) this was observed by kannan et al., 2003 and Speidel has shown that the increase in relative humidity enhanced the SCC crack velocity significantly in 7075 Al alloy. The effect of hydrogen embrittlement will be diminished by providing hydrogen sites like lattice defects such as dislocations, vacancies, grain boundaries and precipitates offer a range of trappings sites for hydrogen diffusion. One of the best heat treatment for 7xxx alloys is overaging which provides efficient tapping sites for hydrogen inhibition in to the lattice sites. This heat-treatment provides a coarser precipitates along the grain boundaries with some interparticle distances acts as a trapping sites for hydrogen ions.

Anodic dissolution assisted cracking: - Anodic dissolution assisted cracking is characteristically an intergranular mode of failure. Anodic dissolution will proceeds when the grain boundaries or grain adjacent regions should be anodic to the rest of the microstructure, so that the dissolution proceeds selectively along the boundaries. It has been reported by many authors such as bobby et al.[17] in the alloys such as Al-Zn-Mg-Cu-Zr and 7039 that the passive film breakdown in the vicinity of copper rich intermetallic caused the crack initiation in the alloy. Fracture surface analysis in their studies reported that the continuous nature of anodic grain boundary precipitates caused easy dissolution leads to crack propagation and underwent intergranular stress corrosion cracking.

Aluminum alloys have excellent formability, high strength-to-weight ratio and good machinability. Due to this reason, these alloys are used in aircraft structures, automobile components and in structural components. Aluminum and its alloys are resistant to corrosion as

it has Al_2O_3 layer formed on the surface. The high strength Al alloys are prone to SCC due to presence of constituent alloying elements. Among the eight series of Al alloys, SCC is most common in 2xxx, 5xxx and 7xxx (alloys containing Mg) series Al-alloys. Precipitation-hardening alloys containing soluble alloying elements, such as Mg, Cu, Si and Zn are susceptible to SCC. It was reported that more number of aircraft components made of 7079-T6, 7075-T6 and 2024-T3 Al-alloys were failed in the year from 1960 to 1970 and these failures were attributed to the SCC [13].

In 2xxx series alloys the major constituents are copper and magnesium and the strength of the alloy attained in this alloy due to the formation of the precipitation hardening of the constituent alloying elements which is achieved by solution heat treatment followed by rapid cooling either by artificial aging at elevated temperature T6 or by natural aging.

SCC has major influences in the 2xxx series alloys as the main constituent of the alloy being copper and Mg which has an alarming effect on the EAC. SCC behavior in 2xxx series depend on the volume percentage composition and the heat treatment followed. It has been reported that this series alloys, such as 2024, 2014, and 2219 in the T3 and T4 tempers are more susceptible to SCC in the short transverse direction [18-20].

In addition, it has been reported that SCC resistance is further decreased if these alloys in the T3 and T4 tempers condition and heated for short periods in the temperature range used for artificial aging. It has been observed that SCC resistance declination can be caused due to the formation of exclusive precipitation (coursed Al-Cu) along the grain boundary which depleting the regions adjacent to the grain boundaries of solute. In this formed precipitates Cu is the major element which makes the material very prone to intergranular pitting corrosion and SCC. This copper rich precipitates zone along the grain boundary are more noble/cathodic which creates the potential difference between the aluminum matrix hence act as a galvanic coupling between matrix and the formed precipitates results in localized corrosion. The resistance to SCC of these alloys can be enhanced by heating longer times, as specified for the T6 and T8 tempers, the precipitation becomes more homogeneous.

Apart from 2xxx Al alloys Al-Li(such as 2090 and 8090) are more susceptible to intergranular SCC. These Al-Li alloys have more strength as compared to rest of 2xxx alloys

[21-23]. In the peak aged condition; these alloys have high SCC resistance and moderate resistance in overaging condition. However, in underaged condition these alloys are more prone to SCC.

The formation of intermetallic precipitates such as Al_2CuLi at the grain boundaries increases SCC susceptibility of the underaged alloys of the Al-Li alloys. These formed Al_2CuLi are observed to be more anodic to the copper rich matrix leading to crack tip anodic dissolution along the grain boundaries.

It has been reported that with increasing in aging time, copper-containing precipitates form inside the grains. It has been hypothesized that the formation of these precipitates may increase the anode-cathode area ratio in the microstructure such that preferential grain boundary attack is avoided. Similar behavior has been observed with SCC of Al-Li Cu-Mg alloys such as 8090 [23].

5XXX series Al alloys are more susceptible to SCC when cold-rolled and at stabilizing tempers with magnesium contents above 5%. In this alloy it owns highly supersaturated of solid solution, which tends to expel the excess magnesium precipitate such as Mg_2Al_3 along the grain boundary without forming in the grains, which is more anodic to the alloy matrix, and this results in SCC susceptibility [20].

Counterpart on the 5xxx series Al alloys containing low Mg show no intergranular SCC as they do not form any precipitates at the grain boundaries. While alloys exceeding magnesium concentrations of approximately 3%, such as 5083, when in strain-hardened tempers, may develop susceptible microstructures as a result of heating or even after long times at room temperature. It was observed that the anodic dissolution and diffusion of the hydrogen mechanisms leads to SCC in 5xxx series alloys.

While 6xxx Al alloys are very less prone to SCC. Till date there is no reported cases of SCC of this group of alloys, certain abnormal thermal treatments, such as a high solution annealing temperature, followed by a slow quench, can make these alloys susceptible to SCC in the naturally aged T4 condition.

Previously it was stated that among the eight series of aluminum alloys, 2xxx, 5xxx, and 7xxx alloy are susceptible to SCC. As compared to 2xxx and 5xxx Al alloy, 7xxx alloys have wider applications due to superior mechanical properties. The major application of 7xxx is in the field of aerospace industry, military, nuclear and also in the structural parts of building application because of high strength, ductility, toughness, low density to weight ratio and due to good fatigue properties. But, stress corrosion cracking (SCC) resistance is of greater importance in this alloy, since many failures of aircraft structures and components have occurred by SCC since the 1950's [24].

The main components of the 7xxx Al alloy are Zn, Mg, Cu and minor Fe and trace of other intermetallic elements such as Zr, Cr, Si and Mn. In general Al–Zn–Mg–Cu alloys has high potential to recrystallization easily during deformation and subsequent heat treatments ultimately forms recrystallized grain boundary with addition of high angle grain boundary could preferentially eroded and cracked, which is objectionable for applications. Alloying elements for instance Mn, Cr or Zr are commonly added to enhance the recrystallization resistance of Al–Zn–Mg–Cu alloys. On the other hand, the recrystallization of Al–Zn–Mg–Cu alloy cannot be completely suppressed by Mn, Cr or Zr addition although addition of Zr proven more effective and widely used [25]. Aluminum 7050 and 7075 are both majorly used for airframe structures. Both the alloys have common constituent alloying elements, except Cr is replaced by Zr in case of 7050 alloys. In addition, 7050 Al alloy containing a minor Si and Fe content than 7075 which improves the fracture toughness and it has high Cu content than 7075 which enhances the strength and SCC resistance by increasing the temperature range of GP zone stability. 7050 Al alloy is superior alloy than 7075 in overall aspects for example it has got a good combination of strength, toughness and SCC resistance. The better properties of 7050 have attributed due to the presence of Zr, which is responsible for the microstructure stability. The addition of Zr stabilizes the GP zone in a wider range of temperatures therefore, the mechanical properties and SCC resistance are reported to be high. It has been reported that 7050 Al alloy is highly quench sensitive and hard to fabricate thicker sections of consistent strength. It is found that by replacing Zr with Cr, quench sensitivity can be substantially reduced and desired recrystallisation suppressing effect of Cr is maintained [26-28]. The SCC phenomenon is very complex to understand and it is depend on the several factors. On the initiation of crack and its growth is influenced by combination of factors such as microstructure of the material which includes heat

treatment, the amount of impurities, manufacturing background, etc., the aggressive conditions in the environment and finally the level of stresses.

1.3   Laser surface melting

Laser surface melting (LSM) is carried out by heating a metal or alloys by means of a laser, which produces high power to form a melt pool. The melting of the material through the laser power depends on the conductivity, thermal diffusivity and melting point of the material. In addition melting of the metals also depend on the laser power and rate at which laser is traversed. In laser surface-melting process only a limited portion of the material is being melted which resulted in high cooling rates ranging from 100-105° C/s which also depend up on the thermo-physical properties and materials and laser process parameters. The LSM resulted in the new form of microstructure, which is characteristically more homogeneous and has ability to enhance the corrosion resistance. The dimensions of the melt pool during the laser surface melting purely depend on the laser energy density and on the lasing speeds. The melt pool dimensions transforms from hemispherical to flat-bottomed with the increase of scanning speeds as the thermal diffusion become limited. For the LSM the flat-bottomed shape is most desirable.

1.3.1   Lasers

Laser as a short form stands for 'Light Amplification by Stimulated Emission of Radiation'. Fundamentally, lasers are amplifiers of light. Laser light generally recognized as an electromagnetic radiation from 1 nano meter to 1000 micro meter in wavelength. The wavelength range of 400 to 700 nm is known to be visible laser light. From 700 nm to 1000 micrometers it is known as near – infrared and further then this limit know as far-infrared [29, 30]. Lasers utilize a resonator that normally comprise of two mirrors which are set parallel to each other so as to form an optical oscillators. In these oscillators, a light can travel back and

forth in between the mirrors in an active medium that comprise of high purity materials, which has ability to amplifying the laser light. An electric current as an external source is pumped in to the gain medium, which generates the laser radiation, consists of molecules or atoms that contain specific electron energy levels.
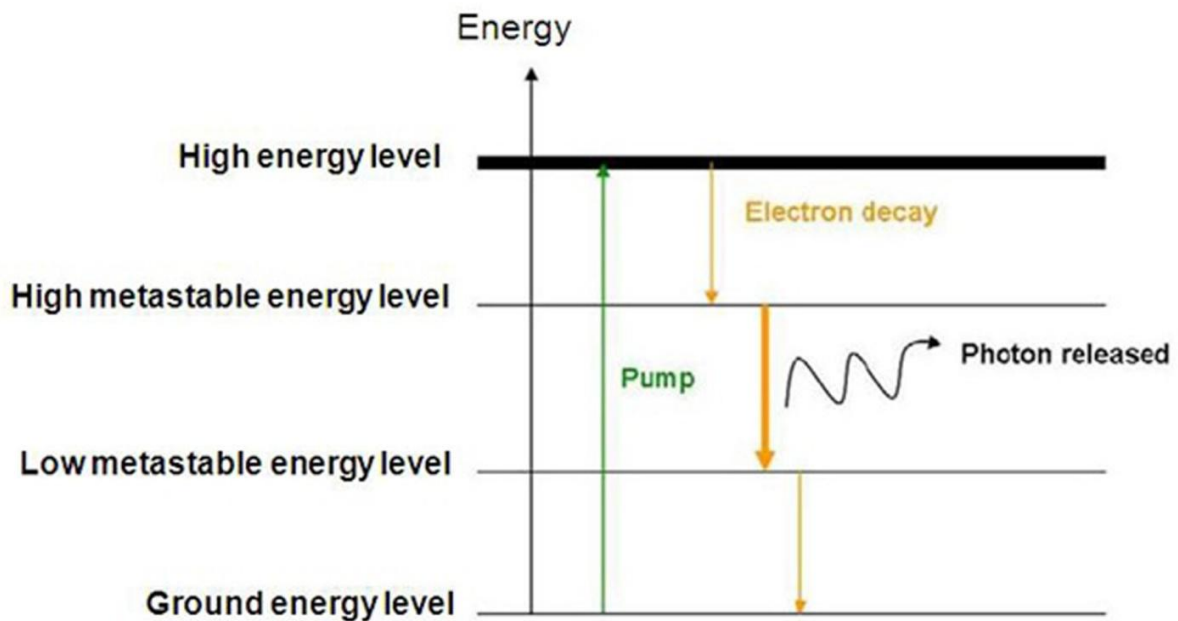
Figure 1.4: Illustrating the continuous wave of laser system from four-electron energy level [31] .

The motion of electrons among the energy levels creates a spontaneous emission of radiation. At least three electron energy levels must be necessary to generate the laser source. The energy levels are ground level, meta-stable and high levels as illustrated in figure 1.4.

Laser can be produced when an electron is excited form the ground level to the high level state. The electrons in the high energy level must be increased to more than the electrons in the ground level, which is known as population inversion. On the subsequent population inversion the electrons then loses energy and fall back from higher energy level (meta-stable)to the lower energy levels(ground level) this phenomenon known as energy decay, in this process the photon is emitted. This emitted photon is considered as light source. To increase the number of photons emissions, the transfer of electrons is stimulated with interaction of additional photons excited

atoms in the gain medium. The emitted laser radiation can be generated in the form of pulsed or continuous wave.

To generate the continuous wave of laser there must be reduction in the energy required to invert the electron population so that the inversion can me maintained easily. This can be achievable by increasing the energy levels. With a minimum of four energy levels and with two meta-stable levels structure the continuous waves can be generated as shown in figure 1.4. For the pulsed laser wave the energy input must be high enough to maintain the population inversion. The pulsed wave can be generated with the three electron energy levels as this can provide the same peak energy to invert the electron population [29, 31]. The continuous wave of laser can be transformed in to pulsed wave by using the Q-switching which has capability of storage radiation and has a control in releasing the radiation in the form of pulses[29] .

1.3.2 Types of high-powered lasers

1.3.2.1. Carbon dioxide laser

CO_2 high-powered lasers were the first generation lasers in used in industries. The light amplification attained through molecular vibrations instead of electronic translations as observed in the other lasers. The wavelength in this lasers lies in between 9.4 and 10.6μm. Due to its larger wavelength it cannot be transported through optical fibers and is generally achieved through mirrors, which has implications in applications.

1.3.2.2. *Neodymium – YAG lasers*

The amplification in the Neodynium – YAG lasers are attained through triply ionized Nd as the lasent and the crystal yttrium-aluminum-garnet as the host. YAG has a chemical oxide of $Y_3Al_5O_{12}$. The typical wavelength in these lasers is about 1.06 μm that fall in the near infrared spectrum. This lasers has feasibility to transported through optical fiber due to this feature it has flexibility industries application.

1.3.2.3. High Power Diode Lasers

The HPDL considered as the superior lasers and has a special consideration due to its unique construction, output characteristics and high precision machine tool. The single diode laser is constructed through one p-n junction formed when two slabs of semi-conductors materials are joined. Usually InGaAs/GaAs and InGaAlAs/GaAs semiconductors are used which can emit light at 808nm and 940nm respectively [32]. The single diodes laser has dimensions of about few hundred microns and has a power of few mill watts. The output of the this laser can be increased by stacking several individual diode arranged in a line on one dimensional array of about 10mm in length known as HPDL bar. These diode bars are then placed one up on other to construct diode stacks, which can generate output power up to 1 kW as shown figure 1.5. Further, these diodes stacks can be combined on the same optical path utilizing polarization coupling and wavelength so the output power increases up to 6kW. The simple construction and less cooling requirements of diode lasers can be considered as more efficient and compact as compared to Nd:YAG and CO_2 lasers.
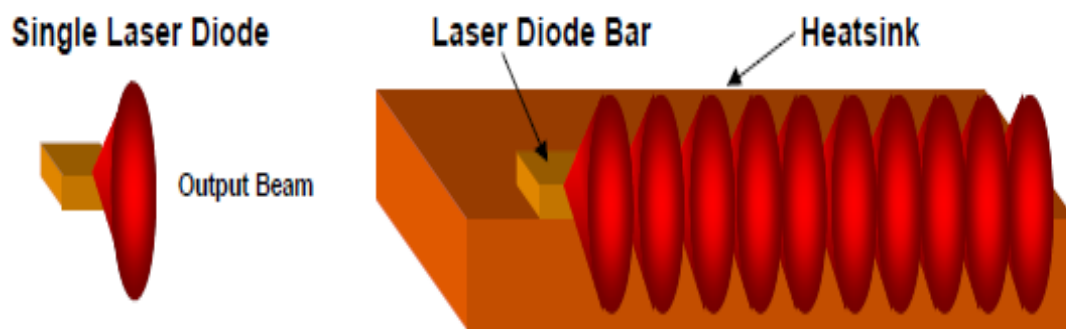
Figure 1.5: Illustrates construction of Diode laser. Multiple individual sources of emitters placed on a single substrate, each source generating a divergent beam of light

(a) Output Characteristics of HPDLs

HPDLs are incomparable with other traditional CO_2 and Nd:YAG lasers due to its many inherent features which make HPDLs more attractive for the material processing, especially for applications where a homogenous and uniform power distribution in the laser spot is required.

Some of the foremost features of HPDLs are as follows:

(b) Wavelength

Over the wavelength range of practical metal processing lasers, the reflectivity of carbon steel varies inversely with wavelength of the incident light. The HPDL possess shorter wavelength in comparison with CO_2 due to which the absorption rate of the incident radiation is high in the metallic materials. Figure 1.6 illustrates the absorption rate for different metals with respective to wavelengths produces by different lasers. It has been observed that the aluminum has coupling efficiency with the diode lasers which has main interest in this work.

(c) Beam Profile, Quality and Stability

The beam profile of a direct application high power diode laser (HPDL) is generally top hat in the slow axis direction and Gaussian in the fast axis direction with a rectangular shaped beam spot. This profile is beneficial for many heat treatment applications such as laser surface transformation hardening, where the resultant uniform heating of the surface generates an even case depth. The great number of superimposed laser beams of a HPDL system also compensates fluctuations within individual beams, giving the combined beam an outstanding modal stability.
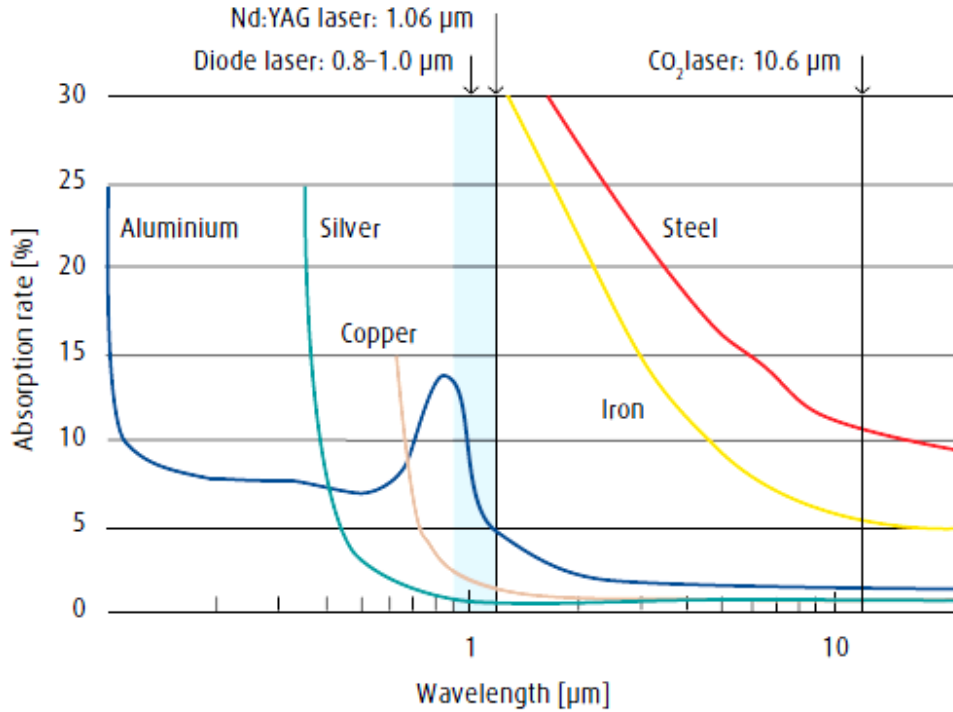
Figure 1.6. Illustrate the absorption of laser for different metals as a function of wavelength

The HPDL efficiency of 30–50% due to laser transported via an optical fiber. The beam quality of HPDLs, however, is poor with typical values of 85×200 mrad^2 compared with 1–5 mrad and 1–10 mrad for CO_2 and Nd:YAG lasers, respectively [32]. With the advent of low cost high energy efficient compact industrial diode laser that is highly amenable for industrial automation, the present study is aimed to investigate the efficacy of diode laser surface melting of 7075-T651 Al-alloy

In recent times, laser based surface modification techniques such as melting, shock-peening, alloying on such aluminum alloys has drawn significant attention in enhancing corrosion resistance without significantly affecting the strength of the bulk [33] [34]. Sometimes, as in case of laser induced shock peening process, laser can also be used to induce shock waves through an absorptive barrier, producing compressive residual surface in depths of few microns and thereby enhance resistance to corrosion, fatigue life, SCC and foreign body damage resistance. Application of laser shock peening technique on compressor blades is widely accepted and is

known to significantly enhance fatigue life by virtue of induced high compressive stresses on surface as compared to other conventional techniques [35, 36]. However some reported results on different alloy showed reduction in fatigue life with application of laser peening process owing to occurrence of internal cracking in the thin modified surface [7]. Although optimization of laser peening process could effectively enhance SCC and fatigue resistance, the limitation in enhancing the thickness of the subsurface modified layer, restricts its utility as enhancing thickness of the residually stressed modified surface was found to induce internal cracking. This envisages searching for an alternative laser based surface modification technique such as laser surface melting (LSM) that can modify the subsurface in tens of microns to millimeters without affecting the bulk.

LSM has become a power tool to modify the surface by rapidly melting near surface layer (in order of few hundreds of microns) by conduction and thereby producing a high degree homogeneous and refined microstructure in short duration without affecting the bulk. Significant improvement in resistance to pitting corrosion, SCC and corrosion fatigue has been observed on 7xxx Al-alloys and their composites due to LSM without affecting the strength of the bulk and thereby envisaging their applicability in high thrust bearing areas under corrosive media [37]. Recent research studies conducted on LSM of 7075 Al-alloy utilizing Eximer, Nd:YAG lasers showed great promise in enhancing corrosion resistance through dissolution and redistribution of precipitates and solid-solution strengthened phase transformations in refined microstructures [37, 38]. According to the LSM study conducted by Yue et al., utilizing KrF laser, on 7075-T651 aluminum alloy, crack-free surface produced comprised of uniformly refined microstructure with complete elimination of coarse second-phase constituent particles up to the laser-melted boundary as compared to their significant presence in wrought structure. The elimination of grain boundary to the shallow depth without any pronounced heat affected zone in the melted layer was attributed to the largely taken constituent particles into the solution of the melt pool associated with rapid cooling effects inherent with short duration laser irradiation and minimal thermal diffusion. The absence of galvanizing constituent particles in grains and grain boundaries of the melted microstructure will delay nucleation of surface defects as well as crack propagation of SCC. Additionally, delay in initiation of anodic sites and hydrogen transportation facilitates in further decelerating crack initiation and hydrogen embrittlement [39].

Furthermore, TEM study by same authors revealed formation of chemically stable nano-crystalline α-Al$_2$O$_3$ in the melted layer that facilitate as an effective barrier to protect the matrix against corrosion attack as against readily formed porous and fragile corrosion film initiating pitting corrosion and destruction in untreated surface due to presence of numerous second-phase particles [40]. Overall, the study showed great promise in improving SCC resistance of re-solidified layer with virtually no intergranular corrosion cracking as against severe SCC in untreated counterpart. In another study involving LSM under nitrogen atmosphere of same 7075 aluminum alloy, utilizing a Nd:YAG laser, a three-to-five fold improvement in SCC resistance was observed as compared to that of untreated counterpart [38]. They attributed such vast improvement in SCC resistance to the formation of fine cellular/dendritic structure in 300-micron deep melted layer that can effectively resist corrosion initiation. Additionally, presence of AlN in the melted layer processed under nitrogen acted as electrical insulator and inhibited corrosion initiation. As compared to laser melted layer proceed under nitrogen environment, air-processed layer showed relatively low improvement in SCC resistance owing to absence of AlN phase in re-solidified layer. Although LSM of 7075 Al-alloy under peak aged condition utilizing conventional YAG, Eximer and CO$_2$ lasers showed great promise in improving corrosion resistance, adoption of small laser beams with overlapping of tracks pose certain inherent disadvantages to apply in actual industrial applications. Lasing with large sized beam with elimination of overlapping can effectively avoid detrimental affects at overlapped regions and thereby enhance structural homogeneity in re-solidified layer and thereby reduce SCC and pitting corrosion effects. As the corrosion performance is very sensitive to inhomogeneities, significant overlap may degrade the corrosion properties. Furthermore, elimination of overlapping with enhanced coupling (especially possible with diode laser) further facilitate in fast processing time and high production efficiency.

1.4 Chapter summary

This chapter presented a brief introduction on 7XXX aluminum alloys and their corrosion properties. In addition, introduction to SCC and various factors and mechanism for SCC are discussed. Also, introduction to lasers and laser surface modifications are presented.

CHAPTER 2

Literature Survey

2.1 Introduction

7xxx series aluminum alloys have specific application in aerospace, military and structural industries due to superior mechanical properties. In these high strength 7xxx aluminum alloys, corrosion and SCC plays a vital factor of consideration, as these failures are catastrophic during the service. The understanding of corrosion behavior possesses critical challenge for this alloy. The main aim of this literature study is to understand the effect of constituent alloying elements on the response of microstructural variation in various heat-treated conditions on various corrosion behaviors such as pitting and SCC. Further, this literature study provides various methods for improving the corrosion resistance using thermo-mechanical treatments and by surface modifications of 7xxx alloys. This literature study also presents the effect of stress and pre-strain, effect of constituent alloying elements in the alloy, and the effect of environments on SCC behavior. In addition, the SCC behaviors of weldments, 7xxx metal matrix composites and also laser surface modifications.

2.2 Factors affecting stress corrosion cracking (SCC)

2.2.1 Effect of composition on SCC

The composition of the material has a vital role in mechanical properties and in SCC behavior. Segregation and Precipitation of alloying elements along the grain boundaries play a critical role in the SCC and on tensile behavior. 7xxx series alloys comprises two types of constituent particles which are contributing for high strength and SCC those are (i) precipitates like Al, Mg and Zn are anodic to the matrix and readily dissolve (ii) Precipitates such as Fe ,Cu, Mn are cathodic to the matrix and tends to boost dissolution of the adjacent matrix. Zn and Mg combine to form $MgZn_2$ precipitate known as η phase. The strength of the alloy is improved by the presence of fine $MgZn_2$ precipitates in the grains, this phase act as anode to the matrix phase and hence in certain temper conditions, the precipitates are continuously develop along the grain boundary. The dissolution of these precipitates causes easy crack propagation under tensile

stress, giving rise to SCC. In 7xxx alloys, observations of environmentally assisted cracking (EAC) are predominantly intergranular, hence, the enrichment or depletion of Mg, Zn, or Cu plays a key role in EAC resistance [9].

Many of the authors reported that there are two main mechanisms for SCC to occur in 7xxx series Al alloys which are reported to be hydrogen embrittlement and anodic dissolution. It was reported that the lattice diffusion coefficients of hydrogen ions are very low in FCC materials such as in this alloys, unfortunately it was observed that tendency of hydrogen transportation is more in this alloy was due to favorable conditions provide by the grain boundaries for the rapid diffusion of hydrogen. It has been reported that the SCC sensitivity of 7xxx alloys raises with the raise in Zn and Mg content. Also the SCC susceptibility depend on the ratio of these elements (Zn:Mg) [41, 42]. The additions of Cu recognized to increase the EIC performance of Al-Zn-Mg alloys. The composition parameters of Zn, Mg and Cu have significant influential effect on the SCC susceptibility than the other alloy addition and impurities, which has secondary influences on the SCC behavior.

Gruhl [41, 43] observed that there was a significant linear relationship between the Zn concentration of the solid solution and the logarithm of the time to failure at a constant stress level illustrated in figure 2.1. In addition, observed that the Mg concentration in the solid solution has no apparent relation with the SCC behavior. Gruhl's also observed that the EIC resistance can be improved or optimized by maintaining the ratio of Zn:Mg to 2.7 to 2.9 as shown in Figure 2.2. This approximate atomic ratio of 1 attributes to the equilibrium line between the α-phase and T-phase in the Al-Zn-Mg phase diagram. In addition, it was reported that the addition of Cu improved the EIC resistance of this alloys.

Speidel and Hyatt [20] studied the crack growth rates on AA7178, AA 7079 and AA7075 in NaCl solution as a function of over aging periods. They observed that the alloys having higher Cu content has 2.5 to 3 times the magnitude of crack growth rate as compared to low Cu alloys such as AA7079 in peak aged tempers as illustrated in figure 2.3. Also, observed that the Cu has significant role in improving EIC resistance in over aging treatments. The alloys containing higher Cu content up on over-aging significantly reduced the crack growth rate where as alloys

containing low Cu has not substantially decreased the crack growth rate. In addition to the Cu content in these alloys Zn:Mg ratio has a significant effect on the crack growth rate.
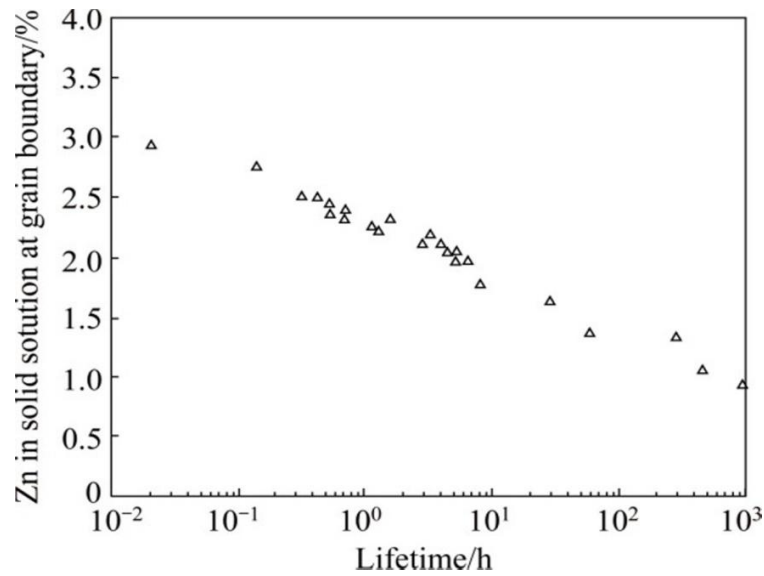
Figure 2.1: Relationship between the Zn content of the grain boundary area and time to fracture of AlZnMg (Cu) alloys, σ = 250 MPa [42].
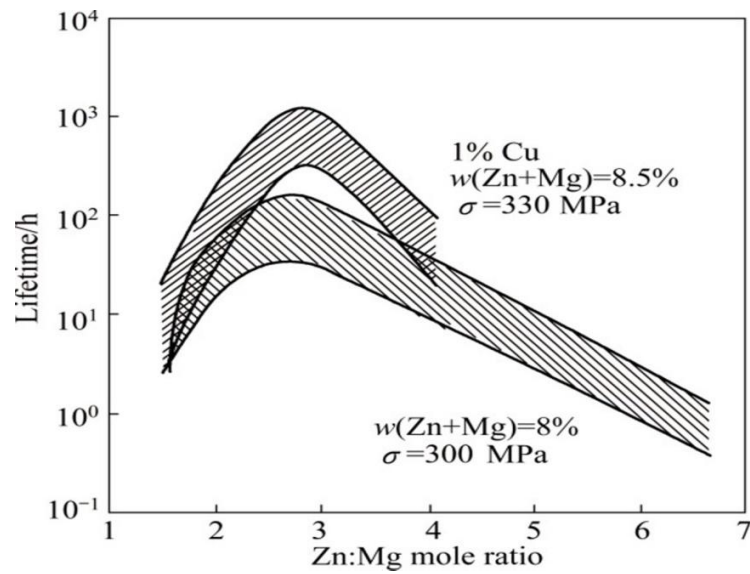
Figure 2.2: Effect of Zn:Mg ratio on SCC susceptibility in some 7xxx series alloys [42].
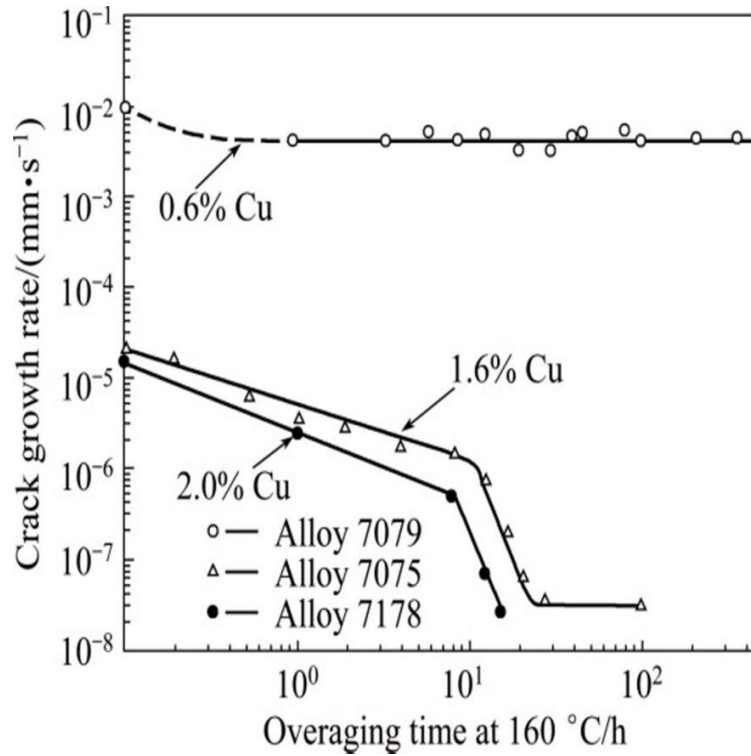
Figure 2.3: Effect of Cu contents in various 7XXX on crack growth rates as a function of overaging time [13].

The influence of Cu wt% and the heat treatment on the SCC characteristics on 70750 (Al-6Zn-2Mg-XCu) was studied by Sarkar, Marek and Starke [44] [45] and reported that as Cu content increases from 0 to 2.1% the stage II crack growth of T6 temper decreased as illustrated in figure 2.4. Further over-aging appreciably resulted in further decline of the crack growth rate only after significant over-aging with loses of strength figure 2.5.

It has been reported that the Mg content along the grain boundary is more electronegativity differences between Mg and H atom than that between Al and H atom [46]. Hence Mg along the grain boundary can attract the hydrogen absorption leads to grain boundary embrittlement and tends accelerate the growth of the stress corrosion cracks.
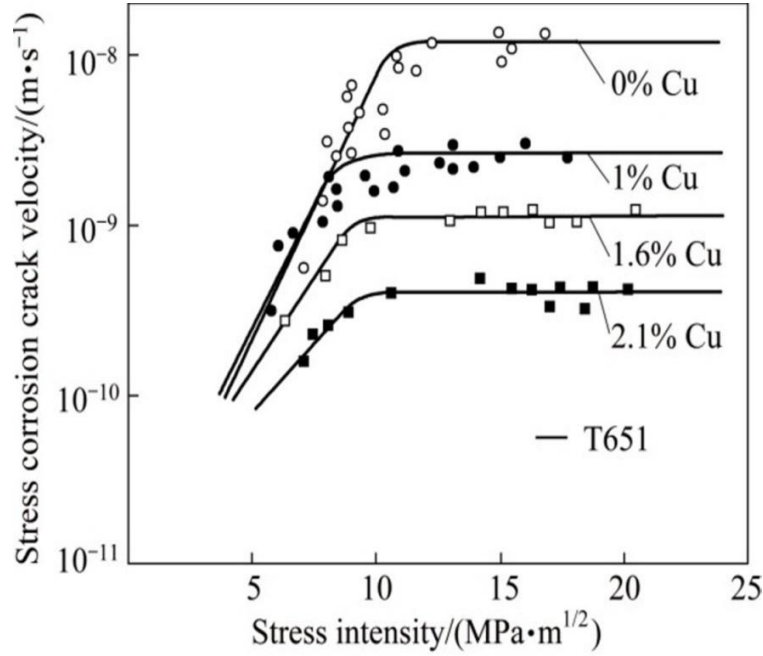
Figure 2.4: Influence of stress intensity on stress corrosion crack velocity of AA 7xxx (varying Cu content)alloys in 3.5% NaCl [44].
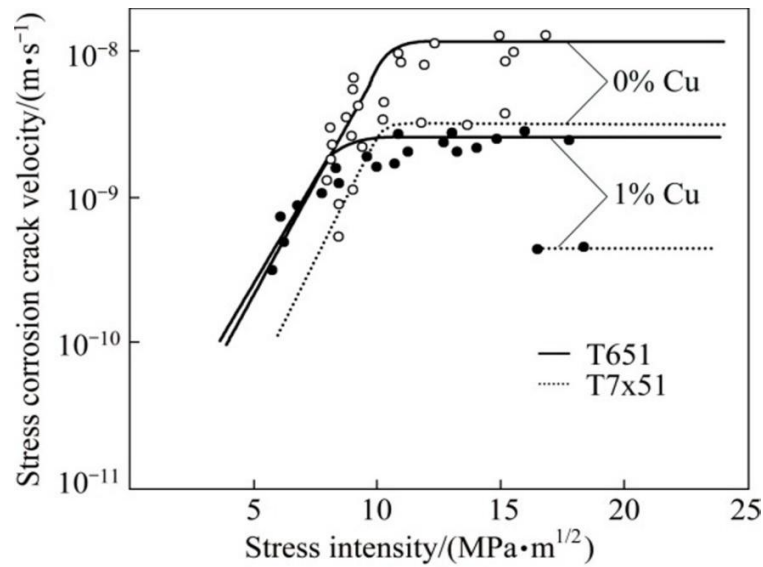
Figure 2.5: Influence of stress intensity on SCC velocity of Al-6Zn-2Mg-XCu in 3.5% NaCl for -T651 and -T7x51 type aging treatments [44].

The presence of Cu in 7xxx Al alloy has an intense effect on SCC behavior. Cu rich grain boundary precipitates will cause lower the electrochemical activity and lowers the hydrogen generation rates. Also the dissolution of Cu in both in matrix and η phase makes both noble where hydrogen generation accompanies the electrochemical dissolution at active sites in 7xxx alloys, resulting in an improvement of SCC resistance [47]. The GBP Cu content effects on crack over-potential for H production and H trapping in the GB region. The more Cu in the GBP (arising from optimized S-phase dissolution) raises the bulk alloy potential and makes the kinetics of hydrogen evolution more sluggish. It is also reported that increasing the Cu content of 7xxx alloys from 0.01 wt% to 2.0 wt% declines the crack propagation speed progressively and the decrease about 2 times in magnitude as a result of the altering in the electrochemical behavior of η precipitates as a function of Cu content in alloys.

In the report of Xian-zhe et al.,[48] stated that the Cu/Mg ratio of 1.6 in 7085 Al alloys resulted in better recrystallization inhibition and corrosion resistance and when the Cu/Mg ratio was about 0.67, the alloy resulted in better mechanical properties. Further it was observed that the there was decline in both the SCC and mechanical properties when Cu/Mg ratio is equal to 1.

It is reported that chromium and copper additions to the base alloy slow down the rate of pre exposure embrittlement. Chromium slow down the transportation of Hydrogen ions on the grain boundaries hence increases the SCC resistance when alloys are pre exposed to hydrogen containing corrosive environments. Alloying with chromium also reported that it forms much finer grains resulting larger grain boundary area which may reduce rate of hydrogen embrittlement [49].

The addition of the Sc in 7xxx alloy has beneficial effect on the strength and SCC behavior which is reported by many authors [50]. It was observed that Sc in combination with Zr enhances the recrystallization inhibition effect significantly. It was also observed that the addition of Sc enhance the SCC resistance of Al-Mg alloys and Al-Zn-Mg-Cu alloy. According to the [51] electrical conductivity factor used as an index for evaluating corrosion resistance, that

is, higher electrical conductivity means that the material has superior SCC resistance. LIU Ying-ying et al. stated that when rare earth metals such as Er added to Al-Zn-Mg-Cu alloy and followed by heat treatment will enhance ductility, strength and conductivity thereby increasing SCC resistance of the alloy [52]. Yb, Er, Cr, SC and Zr addition in 7xxx Al alloys can enhance the recrystallization inhibition there by increasing the corrosion resistance. Also observed that the addition of Sc and Zr provide favorable condition for the formation of discontinuous precipitates along the grain boundaries. When this alloy aged at 120°C for 36 h resulted in enhanced corrosion properties along with good mechanical properties.[50, 53, 54].

Iron and silicon are reported to be the main impurities in commercial grade aluminum alloys [55, 56]. The solubility of iron and silicon are high in molten aluminum, but are low in solid aluminum [56]. Therefore, most of iron and silicon will precipitate out during solidification and form large second phase particles. The iron rich particles, such as Al_3Fe and Al_7Cu_2Fe, usually act as cathodes on the surface of the alloy, promoting electrochemical attack. Murray et al. reported that the presence of Cu ions in the solution would cause metallic copper to plate onto the iron-rich particles[57]. If the matrix adjacent to the iron-rich particles contains copper, aluminum will be dissolved and the copper will remain inside pits and plate onto iron-rich particles, which makes the particles more cathodic with respect to aluminum [57].

The percentage of Si has also has influence on corrosion behavior of 7xxx Al alloys. It has been observed that the area fraction of Mg_2Si improved and coarse phases including $Mg(Al,Cu,Zn)_2$, Al_2CuMg, and Al_7Cu_2Fe decreases as the Si content increasing from 0.094% to 0.261%. The mechanical properties were declined when Si content is increase where as the electrical conductivity and SCC resistance has been enhanced with increase in Si content [58].

It can be concluded that Mg has adverse effect on the SCC initiation and its presence enables two mechanisms to activate SCC failures that is it provides an active path for diffusion of hydrogen ion in to the grain boundaries and leading to intergranular cracking and second is that it increases the anodic dissolution rate. To deactivate or to retard both the mechanism, it is reported that alloying with copper, which enable its dissolution in the matrix and enters in to the η phase along the grain boundaries, making both nobler. As a result, the mixed potential at the crack tip

shifts to a nobler value and hence SCC resistance is increased by reducing anodic dissolution rate and by reducing hydrogen diffusion rate. Similar observations are made with the addition of chromium.

2.2.2 Effect of Microstructure and heat treatments on SCC behavior

The microstructural analysis of the alloy is the well evaluate parameter used to find the microstructural resistant to SCC without disturbing the high-performance mechanical properties of the material [59]. In 7xxx series aluminum alloy, highest strength attained in peak age heat treated conditions i.e. at T6 temper. High strength and mechanical properties in this temper condition is attributed to the presence of fine dispersed precipitates in the grains which obstruct the dislocation movement thereby enhancing the properties. The general precipitation formation sequence of 7xxx series alloys is

Solid solution -> Gp zone -> η' metastable (semi coherent) -> η stable (pseudo coherent)

The main precipitates produces in peak aged condition are η' $Mg(ZnCuAl)_2$ or $(MgZn_2)$ which are semi coherent with the matrix and has a platelet like appearance. Generally two ageing peaks were observed during aging in Al-Zn-Mg-Cu alloys[60]. The high density of the coherent weak and soft G.P. Zones in the matrix responsible for the first aging peak. The strength of the first peak stage will considerably depend on the density of G.P zones. As the dislocation, bisect the G.P Zone attributed to increase in strength due to increase in surface energy. On further aging the strength declines due to dissolution of G.P zones. The second peak is associated with semi coherent η' phase. In this phase the dislocations only bypass the η' phase (Orowan mechanism)[61]. The peak value of the second peak depend on the volume fraction of the η' precipitates and interspacing distance. For 7xxx –T6 peak aged condition the η' phase is the primary precipitate and the main precipitate in over-aged temper (T7x) is the η phase.

It was reported that the three regions in the microstructure play a critical role in SCC to occur, those three regions are (1) precipitates in the interior of the grain boundary (2) the equilibrium precipitate lying along the grain boundary and (3) precipitate free zone (P.F.Z). The arrangement of the precipitates above mentioned are formed with proper heat treatment

processes such as underaging, overaging, peakaging etc. and with proper assistances of quenching techniques and or formed with proper thermo-mechanical treatments. Aluminum alloys consist of large number of alloying elements which are differing in electrochemical potentials among themselves and also differ from the matrix. High strength Al alloys [4] contains two types of constituent particles which are contributing for high strength and SCC behavior. Those are (i) particles such as Al, Mg and Zn which are anodic with respect to the matrix and readily suspend (ii) particles behave as cathodic with respect to the matrix and tends to promote corrosion or disintegration of the adjoining matrix such particle are Fe, Cu, Mn. Due to the presence of these two distinct categorized constituent particles tends to arise galvanic effect which results in development of corrosion pits at these particle interfaces. Once corrosion pits are formed they act as sites for stress concentration leading to stress corrosion cracking failure.

As 7xxx series aluminum alloys are extensively utilized in aerospace, structural components and in unique navy application, are subject to aggressive environmental and stressed conditions where it encounters salt water spray and or salt fog environments. As in case of peak aged condition it has been observed that fine η' precipitates are dispersed inside the grains as well as at continually dispersed along the grain boundary. The grain boundary precipitates are identified as the equilibrium η ($MgZn_2$) phase [62] .Due to formation of different precipitates in and around the grain boundary raises the potential difference between the matrix and grain boundaries. This continuous precipitate at the grain boundaries act as anodic tunnels of intergranular corrosion and enhance the SCC rate of the alloy by accelerating the hydrogen transportation which further embrittling the grain boundaries [47]. In 7xxx Al series the SCC mechanism involves repeated sequences of: (1) Generation of hydrogen at crack tips. (2) Diffusion of hydrogen ahead of crack tips. (3) "Brittle" fractures when a critical hydrogen concentration is reached over a critical distance.

The oxide or the solid solution act as the cathode and $MgZn_2$ phase behave as the anode. The factors such as size, nativity (matrix or grain boundary) and coherency of $MgZn_2$ will determine the corrosion behavior of this alloy and has intense influence on the corrosion potentials [27] . The Mg and Zn in the solid solution tendency to shift the corrosion potential of Al towards the active direction. The diffusion of Mg and Zn take place from the matrix and move to the grain boundaries resulting in decreasing in concentration levels of $MgZn_2$ in the

solid solution further resulting in noble shift in the corrosion potential. The noble shift will depend on the extent in $MgZn_2$ precipitation formation.

The dissolution of η precipitates from grain boundaries, coherent precipitates η'', semi-coherent precipitates η' and Al in the matrixes are dissolved into the solution with a simultaneously cathodic reaction.

The anodic dissolution reactions are

$MgZn_2$ (in GP zones, η'', η' and η) $\rightarrow Mg^{2+} + 2 Zn^{2+} + 6 e^-$ Eq. (2.1)

Al (in solid solution) $\rightarrow Al^{3+} + 3 e^-$ Eq. (2.2)
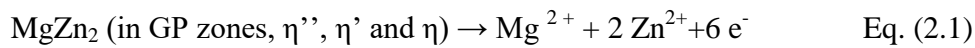
And the simultaneously cathodic reaction is

$2H_2O + 2 e^- \rightarrow H_{2(g)} + 2 O H^-$ Eq. (2.3)

The segregating of the cations (such as Mg^{2+}, Zn^{2+} and Al^{3+}) dissolved close to anodes leads to combine with the hydroxide in the locality of cathodes to form precipitation as their solubility product over the Ksp (equilibrium solubility product).

They are two methods to in improving the SCC resistance. The first method is to disintegrate the continuity of the GBPs and second method is to decrease the potential difference between matrix and grain boundary. The extensive study of the Ardo et, al. [63] stated that the dispersion or the arrangement of the matrix precipitate, size and type are very important in ascertaining the SCC behavior and also reported that the susceptibility change with variation in the dislocation-matrix precipitate interactions and the width of the P F Z, which is immaterial in the SCC susceptible, the changes in grain boundary precipitates could have a perceptible effect on the SCC. Many of the researches attempted to change the in-grain and grain boundary precipitates by employing various thermal treatments. Puiggali et al.,[64] in their research observed that prolong aging of French alloy 7010 increases the SCC resistance. This behavior is due to the alternating the distribution and volume fraction of MgZn, also they stated that extended ageing has clear influences on the growth and stability of the passive layer which has a tremendous effect on the inclination to pitting and intergranular corrosion and crack initiation

hence it can be concluded that microstructural features affecting the SCC resistance are the grain boundary precipitates (GBP).

The other method for improving the SCC resistance is by increasing both the size and the inter-particle distance of the GBP [27]. It is well known that precipitate free zones (PFZ) form during aging of high strength Al-alloys. Various factors such as aging temperature grain boundary mis-orientations and quench rate from solution treatment have an influence on the PFZ width. Although there exists a significant microstructural difference between the PFZ and the adjacent matrix, it was reported that the width of PFZ ternary Al-Zn-Mg alloys has no influence on the SCC behaviour in aqueous sodium chloride solution [59] .However, the relative strengths of the PFZ and grain interior determine the extent of strain localization at grain boundaries and affect the fracture toughness [65].

Tsai and Chuang [66] studied the effect of grain size on the SCC behaviour of 7475 Al-Alloy. They observed that the refinement of grain attributed in attaining high homogeneous slip mode and has resulted in a smaller sized grain boundary precipitates (GBPs), which has great influenced the SCC resistance. It was also reported that the high homogeneous slip mode is advantageous for enhancing the SCC resistance. However, if the size of GBPs was smaller than the critical precipitate size for nucleating hydrogen bubbles, the there is no beneficial effect due to either grain refinement or more homogeneous slip mode. The orientation of the grain also has influences the SCC behaviour of high strength Al-alloys. Intergranular SCC failures are very common in high strength Al alloys containing pancake shape grains, typically occurring in rolled plates and extrusions (Figure 2.6). The failures occur predominantly when the applied stresses are in the short-transverse direction. However, when the applied stresses are in the longitudinal or long-transverse directions, the intergranular crack path is not easy, hence leading to a high resistance to SCC. Although transgranular cracking can occur when there is no easy intergranular pathway, it is not that widely reported.

As stated earlier peak aged condition (T6) of 7xxx alloy attains high strength and high mechanical properties due to precipitate hardening and has low response to SCC. Apart from peak aging another aging has treatment know as overgaing (T7x) has significant response to SCC

resistance when compared to T6 condition. In comparison with T6 condition, T7x temper condition is followed by loss in strength by 10 to 15 % and reported lower hardness values due to coarsening of precipitates as it exposed to prolonged heating. In this over aged state the precipitates tends to coarsened and accumulated along the grain boundaries, which as potential to decrease the scattering of electrons and attributing in enhancing the conductivity.

In addition, these coarsened precipitates discourage the phenomenon of anodic tunnels of intergranular corrosion. The coarsened and discontinuously precipitates, arranged on the grain boundary with inter-particle spacing decreases the anodic dissolution speed and act as the entrapping regions for atomic hydrogen ions and produce molecular hydrogen bubbles to reduce the accumulation of the hydrogen ions in the grain boundaries [67]. Also, it is reported that SCC resistance enhanced by means of the more homogeneous slip mode and reduction of the slip planarity, due to increasing in size of matrix precipitate and the associated changes from Gp zone to semi coherent and in coherent precipitates. It has been reported that a single step aging to the T73 and T76 regarded as a best approach to increase the tensile strength and SCC resistance
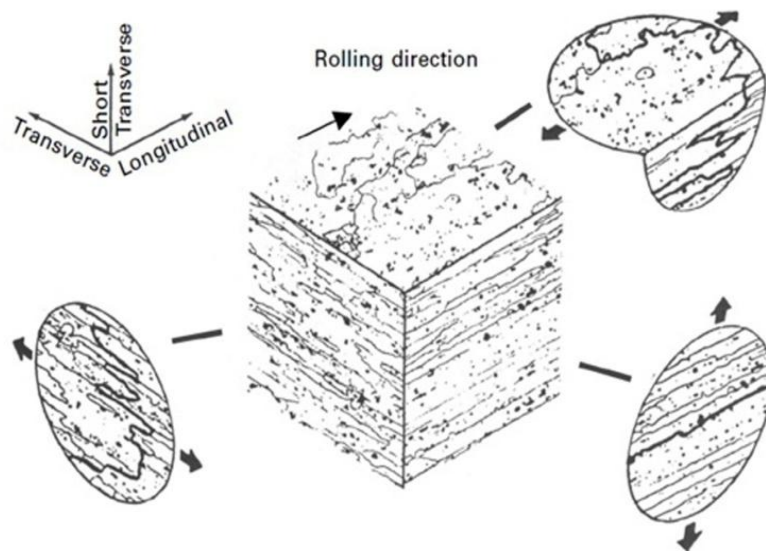
Figure 2.6: Effect of grain structure on the intergranular crack for sample stressed in different orientations [13].

.

In the report of the Lin [27] explained about the SCC mechanisms with respective to the heat treatment. They have stated that SCC degradation of 7xxx Aluminum alloy in saline environment is due to the three major mechanisms (1) Anodic dissolution (AD), (2) Hydrogen-induced cracking (HIC), and (3) Passive film rupture (PFR). The anodic AD dissolution commences immediately when the 7XXX al alloy immersed in the corrosive environment. Anodic dissolution takes place along the active η precipitates where as HIC mechanism undergoes in between space of η precipitates. Both the mechanisms AD and HIC were reported to be more severe in T6, as the rate of AD is much quick in attacking the continuously arranged fine precipitates and HIC is more sever at regions that have closely space precipitates. Apart from the T6 temper, overaging T7X and other novel heat treatments provides a slow rate of anodic attack due to space interruption between the large precipitate. The large precipitates facilitate entrapment of high accumulation of hydrogen and prevent their dispersion to cause SCC failure. Thus the increasing the size and spacing of the η particle decreases AD and HIC.

To overcome the problem observed in over aging, that is loss of tensile strength and decrease in hardness values as compared to T6 treatment, a novel heat treatment proposed by Cina et al. [68] known as retrogression and reaging (RRA) was developed to enhance the SCC resistance of 7xxx alloys without considerable change in strength when compared to the T6 temper. The RRA treatment consist of annealing process of T6 sample at 180-240 ^{o}C for 5-2400 s called as retrogression, which was followed by re-aging implementing similar conditions as used for the original T6 aging. During retrogression it was reported that the initial strength decreases due to reversion of GP zones and dissolution of small η' particles in the matrix, after retrogression treatment and upon further aging results in an increase in strength as of T6 treated sample [69] .

Viana et al. [70] studied the microstructural characterization of 7075 Al in RRA temper and interpreted through calorimetric studies and stated that RRA provided large precipitations of the equilibrium η phase in the grains and in sub-grain boundaries. And continue to preserve distribution of fine η' precipitations within the grain. The grain boundary consist of coarser intermetallic particles place in irregular intervals and act as hydrogen entrapping regions which locally decrease the hydrogen concentration in the matrix around the grain boundary. In this treatment, the increase in strength is attributed to the increases η' precipitates and its

arrangement in the matrix which nucleate due to their re-precipitation. On the other hand, η precipitates at grain boundaries are large enough when compared to the retrogressed state. The TEM microstructures are shown in figure 2.7.

In a short the RRA provides coarser discontinuous equilibrium precipitates $η(MgZn_2)$ in sub grain boundaries and in the grain which are incoherent with matrix. This arrangement of precipitates in this fashion renders increment of the conductivity and decrease the lattice distortion with maintaining a fine distribution of η' in the grain interiors. The coarse phases at the rain boundaries act as a trapping sites of hydrogen and reduces it concentration in and around the grain [71].

The microstructure high strength and resistance to SCC alloy consist of large number of fine particles and the relative strength to SCC is determined by the amount of hydrogen trapping ability by numerous interphase boundaries. The microstructure changes while application of retrogression treatment has been extensively studied Baydogan [72]. They have elaborated the changes in the microstructure in 3 distinct regions as a function of retrogression time. Region I, due to short retrogression time that indicates dissolution of main constituents of microstructure present in T6-temper state, such as GP zones and small η' precipitates. Region II shows the curve at longer retrogression time with matrix rich in Mg and Zn owing to the dissolution encourage the nucleation of new η' precipitates, while existing η' precipitates transform and grow to η. Furthermore η precipitates that are majorly present at the grain boundary are coarsened and spaced with larger intervals. The microstructural changes observed in region II is indication of size and quantity of η and η' precipitates. Furthermore (region III) increase in retrogression time outcomes to overaging which has consequence in precipitates coarsening. The TEM microstructures of the T6, RRA and T73 tempers are shown in figure 9. The arrangements of the precipitates at the grain boundary are described through these TEM images. In T6 condition the precipitate dispersed continuously alongside the grain boundary and finer precipitates present inside the grains. In T73 larger precipitates distributes discontinuously along the grain boundary while depleting distribution of the precipitates in the grain. Where as in RRA treated condition the larger precipitates distribute along the grain boundary while maintaining the fine precipitates inside the grain which satisfy the both SSC and strength of the alloy.

In the study of the Li We Bin et al. reported that RRA not only Increases SCC resistance it also increases the conductivity and observed that in RRA treatment, with an increase in retrogression time and temperature conductivity increased, while decrease in tensile properties were reported [73]. Due to short period retrogression time, RRA treatment was only applicable for thin sections. Initially RRA was applicable for 1 to 6 mm thick components and the application of RRA to thicker components did not give in good results. Rajan suggested that lower retrogression temperatures and longer retrogression times made achievable to apply RRA heat-treatment process to thicker components [74]. In addition, reported that decreasing in hardness when retrogression done for prolonged time due to excessive coarsening of the precipitates which is shown in figure 2.8. Hence optimum retrogression temperature and time became challenging to fulfill both the strength and SCC in RRA treatment for thicker components.

C.P.Ferrer et al worked to determine the lower retrogression temperature used for RRA treatment to enhance the strength and SCC resistance and to extend the applicability of the low temperature retrogression to the thick section of 7075 Al alloy, aircraft components. They have concluded that lower retrogression temperature and with longer duration can improve the SCC resistance of thicker sections by maintaining optimum strength. In this work it was concluded that the RRA process with retrogression at 160°C for 660 min resulted vast improvement in SCC resistance, with only a 4% deduction in strength below T6[75].

Oliveira studied effect of RRA on the SCC resistance and strength of AA7050 alloy and AA7150 aluminium alloys and concluded that maximum hardness after re-aging was obtained in the samples retrogressed for 20 and 40 min. After RRA process 30% improvement in the yield strength was observed in the AA7050 alloy, while for AA7150 alloy the mechanical properties were similar to the original condition and SCC for both the alloys after RRA for 40 min shown the same pattern as of original condition [76].

Many of the authors worked on to improve the SCC resistance by implementing various thermal treatments on the 7xxx alloys, some of the novel thermal treatments are reported below. Apart from aging treatments on the effect of microstructure behavior on SCC, solution treatment also has an impending effect on the microstructural evolution and on the SCC behavior. Min

song [61] reported that the in Al-Zn-Mg alloy enhancement in SCC resistance can be achieved through improved solution heat treatment and high temperature pre precipitation process. In this combined process high copper concentrations and low Mg can be attained with arrangement of discontinuous distribution of GBPs. It was confirmed that the altering the solution treatment temperature has influence on the stress corrosion susceptibility by changing the metallurgical microstructure and the grain boundary composition [77]. The GBPs concentrations of Cu ,Mg and Zn depend on the solution heat treatment temperature. As the solution heat treatment temperature decreases the mentioned concentration also decreases. It was also reported that solution treatment temperature also has influence on the stress corrosion plateau crack velocity.
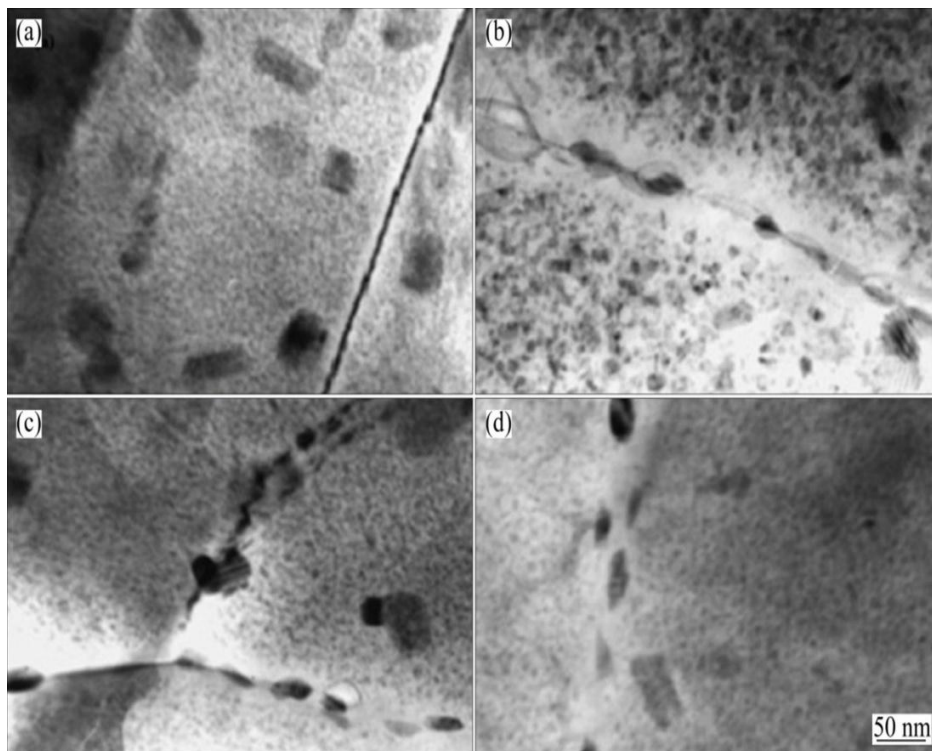
Figure 2.7: TEM microstructure of (a)T6 temper (b) Overaged T7 temper (c)after retrogression (d)after RRA [70].
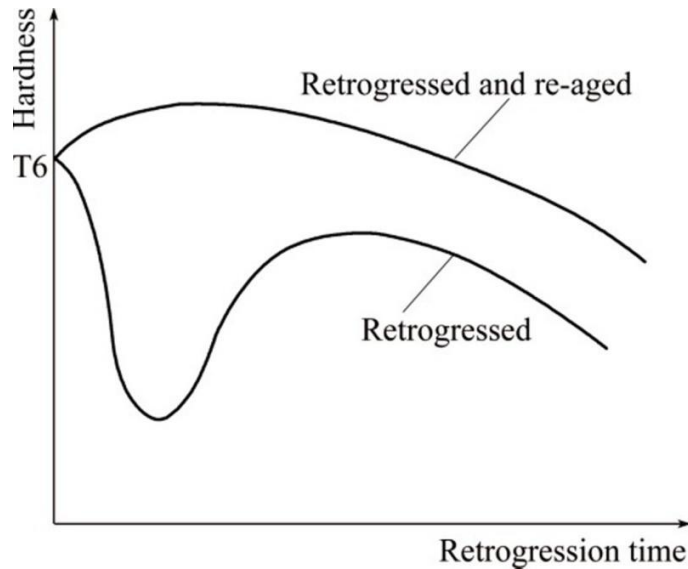
Figure 2.8: Schematic representation of the change in hardness during retrogression and re-ageing [74].

Joshi et al., have determined that the amount of constituent particles such as Mg, Zn, Cu, Fe and Si at the grain boundary depends on the solution heat treatment and successive annealing treatment. Also reported that if identical solution heat treatments are involved, then the final aging treatment that influences the grain boundary solute distribution. They have observed that at 438 ^{o}C the solute concentration was minimum at solution heat treatment done in the range of 399 ^{o}C to 527 ^{o}C [78].

Stepped solution treatment also has a remarkable influence on the SCC behavior and strength of the alloy. The multi stepped solution treatment, prior to RRA treatment increases the dissolution of S-phase (Al$_2$CuMg) which increase the Copper content at the grain boundary and increases the SCC resistance by retarding the anodic reaction kinetics.

D.K. Xu studied the effect of S-phase dissolution on the corrosion and stress corrosion cracking of an As-rolled Al-Zn-Mg-Cu (AA7150) alloy and concluded that by high temperature stepped solution treatment can effectively release Cu into the matrix which increased the Cu content at the grain boundaries after RRA treatment [47]. Another novel heat treatment well-

known as multi step aging in combined with controlled heating rate to attain the final over-aging temperature. This novel heat treatment resulted in better combination of improved strength and fracture toughness. As the RRA treatment was restricted only to the thinner sections where as this novel multi-step aging has prove more advantageous and can be applicable to thicker sections. Kannan [17] reported that with this novel treatment sample can attain superior SCC resistance with higher ductility in an Al-Zn-Mg-Cu-Zr alloy.

Interrupting aging T6I6(130 °C, 80 min + 65 °C, 240 h+130 °C, 18 h) was studied by LI jin feng et al. compared the precipitate densities formed conventional aging treatment such as T6, T7X, RRA and stated that T6I6A possess high density of η' precipitates than the T6 and other aging processes and stated that RRA and T6I6 maintains the strength as that of T6 state and with increase in SCC resistance as compared with T73 and HTPP treatments [79].

Reda et al., and baydogan et al.,[9, 72] worked on to increase the strength, hardness and resistance to SCC of 7075 Al alloy by considering different combination of pre aging and retrogression temperature for different duration of time. They have concluded that the optimum condition was preaging at T6 =120 °C and retrogressing at T7 = 200 °C, gave the highest hardness and tensile properties. Preaging at100 °C and retrogression done 160 °C for 250 min resulted in high resistance to SCC and the sample retrogressed at 200 °C for 8 min resulted in low stress corrosion cracking resistance. They have also reported that the sample retrogressed between 170 °C and 240 °C for short span of time resulted in superior combination of hardness and SCC resistance than the T6- temper state. Further at high retrogression temperature of 380 °C resulted in reduction in SCC and mechanical properties. They concluded that sample retrogressed at 170 °C resulted in excellent combination of SCC and hardness with 20 % enhancement in hardness and 85 % improvement in resistance to corrosion.

G. Silva studied the affect of heat treatment parameters to improve the tensile strength and SCC resistance of 7075 Al alloy. They conducted the test on variously aged sample such as T6, T73, T76 and aged at 163 °C for different duration of time (3,5,8,16 and 24 hours). Their main aim was to study the tensile properties and the SCC behavior of 7075 thick plates when submitted to a single step ageing by varying the ageing times and to decrease the production cost to produce an aircraft material. They concluded that T76 treatment can be replace by the 163° C

aged for 8 hours for larger plates. T6 and plates aged at 163 ^{o}C for 3 and 5 shown failures to SCC. While T76, T73 and plates aged at 163 ^{o}C for 8, 16, 24 hours shown no failure to SCC which can be interpreted in the figure 2.9 [80]
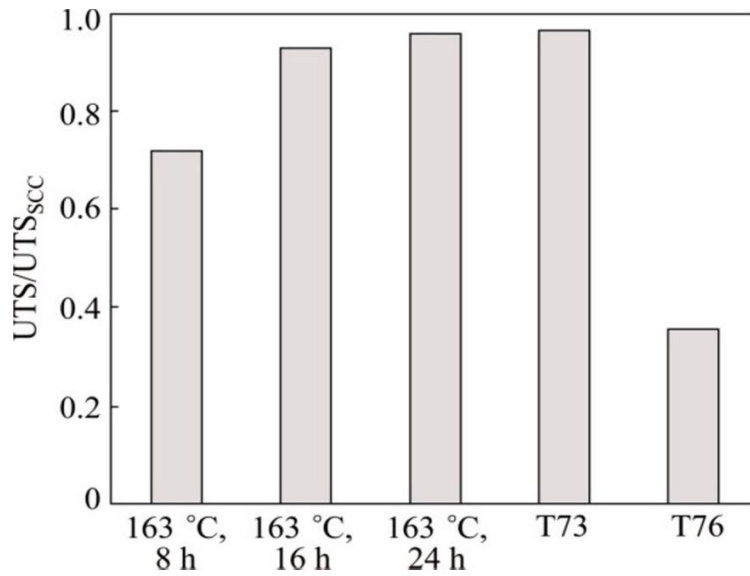
Figure 2.9: Ratio between the ultimate tensile stresses obtained from the tensile tests and the ones obtained by tensile loading of the corroded specimens [80].

Aside from heat treatment, quenching rates also play an important function in an organization the constituent particles in high strength Al alloys. It has been stated that high strength 7xxx alloys are quench sensitive and many authors studied the effect of quench rates on the conduct of mechanical properties and SCC behavior. It has been reported that decreasing the quenching rate will increase the size and inter particle distance of the GBP's along with increase of width of PFZ's. Unfortunately, the copper percentage in grain boundary precipitates will decline with decrease in quench rates. The resistance to SCC of the material first increases and then decreases this attributing to the distribution and size of GBP's and copper content at GBP.

Recently, OU et al. and LIN et al. developed new heat treatment know as step-quenching aging (SQA) and stated that this method as ability to enhance the SCC resistance without losing

its strength. OU et al. also carried out effect of step homozinization on the mechanical and SCC behavior of 7050 Al alloy shown in figure 2.10. They have concluded that the densest and finest distribution of dispersoid, produced through step homogenization (Step-H) treatment, can efficiently inhibit recrystallization to attain the structure which contains smallest fraction of recrystallization. And step quench and aging develops broad spaced GBPs which increases SCC resistance [27, 81].

Many authors studied on the effect of heat treatment and arrangement of the microstructural constituents of the alloy on the SCC behavior and concluded that overage, RRA and novel treatment such as multi-stepped aging and solutionizing treatments are beneficial to improving the SCC without loss of mechanical properties. As these treatments provides efficient arrangement of microstructural constituents which will retard the mechanisms of hydrogen induced cracking and anodic dissolution which are most widespread in 7xxx series alloys.
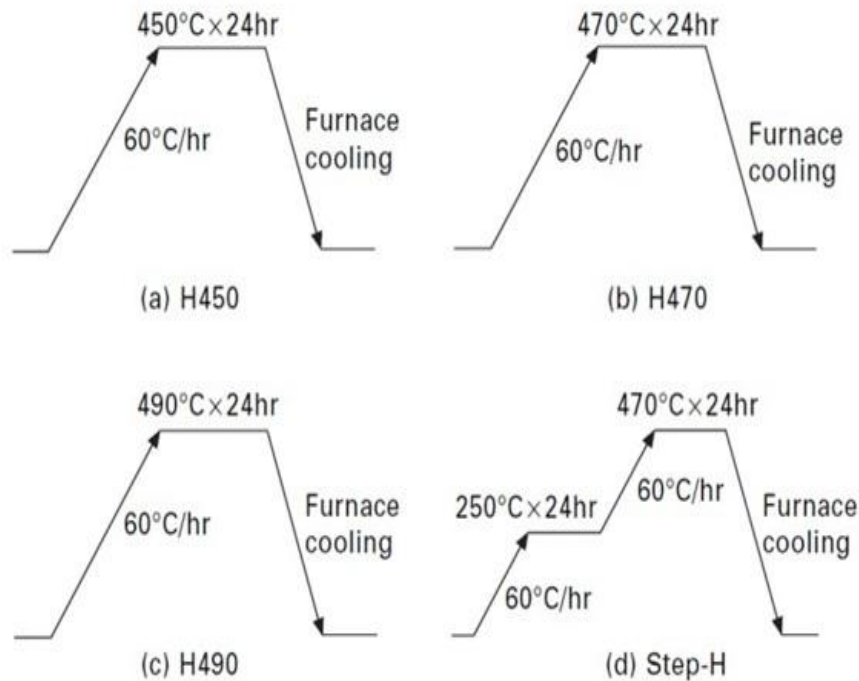
Figure 2.10 Schematic representation of different homogenization (H) treatments [81].

2.2.3   Effect of stress on the SCC behavior

Stress raisers of flaws (such as bolt holes, fatigue cracks, notches etc.) are often required to imitate SCC failure. The magnitude of the stress field surrounding a stress raiser, the stress intensity factor (K), is a function of the flaw size (a), applied stress (σ)and other geometric considerations that depend on the configuration and the manner the stress is applied. Generally double cantilever beam (DCB) specimens which resembles as fatigue pre-cracked specimens used to measure stress corrosion crack propagation rates, are designed to maintain plane strain loading conditions.

Magnin [82] compared stress corrosion cracking (SCC) and corrosion fatigue(CF) under different loading conditions. SCC occurs under constant tensile loads or at slow stain rate while corrosion fatigue occurs under dynamic loadings. At free corrosion potentials it was observed that the corrosion fatigue occurs in all strain rates ranging from $1E^{-8}$ to $1E^{-2}$ s^{-1}. Which SCC occurs at stain rate $< 2E^{-5}$ s^{-1} for 7020 T4 and $< 8E^{-7}$ s^{-1} for 7020 T6 condition. With the strain rates $> \varepsilon$ (SCC), Transgranular corrosion fatigue micro-cracks are developed by joint effect of passive film breakdown and the plastic strain localization due to fatigue.

Intergranular microcracks are formed at strain rates $< \varepsilon$ (SCC) in SCC, the CF is enhanced by SCC. However, upon immediately imposing the cathodic potential (-1100 mV vs. SCE) in electrolyte, SCC does not occur as anodic dissolution does not form to initiate micro-crack. Mechanically formed micro – cracks results in entry of H ion leading to embrittlment and corrosion fatigue failures. These observations support the necessity of a surface defect for hydrogen entry. In SCC anodic dissolution is responsible for the surface defects while in CF the surface defects are generated by mechanical means.

2.2.4 Effect of Environment on SCC behavior

As stated earlier Composition, heat treatment and microstructure of the material plays a major role in SCC susceptibility, little change in the composition of major alloying elements such as Mg and Zn or ratios of them can drastically alter the SCC behavior. Aluminum alloys are prone to corrosion in Aqueous Cl^-, Br^- and I^- solutions and also in moist air and in distilled water. In Generally 3.5 % NaCl solution is taken as corrosive environments for aluminum alloys as it is believed to result in severe general corrosion rates and it represents roughly the salinity of sea water. As aircrafts are exposed to several complex chemical environments both inside and outside, no single environment could simulate the actual condition for this reason, 3.5% NaCl solution taken as a corrosive environment as it assumed as "realistic chemical corrosive environment" [83]. It is also stated that high strength aluminum alloy containing copper in 3.5% aqueous NaCl solution [ASTM G44], develops severe pitting and finally leads to mechanical failures. Apart from 3.5 % NaCl aqueous solution many synthetic environments such simulated sea water was used to study SCC behavior. Braun [84] studied the effect of various synthetic environments on the SCC behavior of 7050 Al alloy by using SSRT technique and concluded that 7050 T7351 shown high resistance to SCC were as T6 condition shows a less resistance and when tested with an aqueous solution of 0.5 M $NaClO_4$ on a smooth specimen no SCC was observed. Al 7050-T651 was found to be sensitive to environmental assisted cracking when Performing SSRT in an aqueous solution of 0.1 M NaCl + 0.05 M Na_2SO_4 + 0.05 M $NaNO_3$ + 0.01 M $NaHCO_3$ at pH 3.5. This synthetic environment did not promote IGSCC when the alloy was aged to the tempers T7651 and T7351.

Stress corrosion behavior in mode I(tension) and in mode III (torsion) of underaged, T6 and T73 treated 7075 Al in a corrosive medium of 1N $AlCl_3$ reported to be high resistance to SCC in T73 condition. Mueller et al. reported that [85] predominant mechanisms of SCC were hydrogen embrittlement in mode 1 and anodic dissolution in mode III. They also concluded that highly aggressive environment such as $AlCl_3$ can add a strong non-SCC component to the cracking and therefore lead to possible misinterpretations of accelerated laboratory SCC tests conducted in this environment. A better suitable corrosive environment to conduct SCC test is an aqueous solution of 3.5 % NaCl.

The effect of test environment temperature on SCC behavior studied by J. Onoro and C. Ranninger [86]. They stated that temperature of the environment is a basic parameter for the SCC process. And it has influence on the chemical reactions takes place at the crack and also has influence on rate of diffusion of corrosion products from the corrosion environment to material. The SCC test was conducted in different test heated environment (20 ^{o}C and 80 ^{o}C) on different temper condition and concluded that T6 condition more susceptibility to SCC than T73 and RAA.

Many authors has studied on the effect of the moisture content on loss of ductility when SCC test conducted in laboratory environment and main emphasis was made on the presence of humidity and hydrogen presence in the laboratory environment and they have also studied the effect of relative humidity and found that the ductility ratio decrease with increase in relative humidity. SCC [87] behavior of underaged 7010 Al was tested in glycerin and the results were compared with the results obtained from 3.5 % NaCl solution and laboratory air. It was concluded that laboratory atmosphere in not considered as inert atmosphere as the alloy undergone SCC failure due to hydrogen embrittlement and due to relative high humidity of the test environment. In contrast they have concluded that glycerin can be taken as inert environment for conducting SCC.

W-T.sai et al has studied on the effect strain rate, solution pH and dissolved oxygen on SCC behavior of 7050 – T7451 Al alloy in 3.5 Wt% NaCl solutions. They have concluded the following observations. At strain rate of 8 X 10^{-7} in neutral 3.5 wt% NaCl solution the alloy was most susceptible to SCC in short transverse direction. Regardless the presence of dissolve oxygen at pH <4 the alloy was more susceptible to intergranular stress corrosion cracking and at pH>10 SCC was less convincing to failure as compared to acidic environments. But they observed that in the presence of oxygen in the pH range of 4 to 10 SCC is more profoundly affected. The alloy tested was susceptible to SCC in non-deaerated solution but showed immunity when oxygen was removed. The presence of oxygen would promote pitting corrosion and assisted the nucleation of stress corrosion cracks [26].

Rout et al [88] observed that the SCC susceptibility depends on the pH values. For all the temper condition samples the SCC was sever in the pH of 1 and intermediate in the pH12 and

observed to be least in pH of 7. and also observed that in all the cases anodic dissolution accompanied ny hydrogen induced cracking responsible for the SCC failures.

2.2.5   Effect of pre immersion of alloy in corrosive medium on SCC

Extensive research has been done on the effect of the pre immersion on the stress cracking behavior of Al alloys, it has been stated that pre exposing results in the diffusion of H^+ ions through the grain boundaries which leads in decrease of the grain boundary cohesion in turn intergranular fracture due to hydrogen embrittlement. SCAMAN observed same behavior of embrittlment of grain boundaries when working on the SCC behavior of pre immersed 7075 Al alloys. The severity of hydrogen embrittlement depends on the factors such as pre exposure time, temperature of the environment and relative humidity of the pre-exposure environment. They have also reported that the addition of copper up to 1.7 % or chromium up to 0.14% suppresses the hydrogen embrittlement in high purity alloy and even more decreases in the 7075 Al alloy [49].

The surface of the sample becomes saturated with hydrogen when pre exposure with corrosion media and further up on application of stress causes this hydrogen to penetrate in to the bulk of the specimen. The effect of pre exposure can be removed through repeating the complete heat treatment process as done to 7xxx Al, after exposed to the saline environment. Pre exposure of the corrosive media decreases the ductility of the commercial 7075 alloy due to pre chathodic charging. As the pre chathodic charging of this alloy exhibits all the aspects of typical strain aging hydrogen embrittlement. Similarly Tromans and Pathanias reported that the pre cathodic charging also decrease the time to failure of stress corroded high purity 7xxx alloys this aging attributing to the hydrogen embrittlement [89].

Pre immersion in 3.5% NaCl (pH=12) about 240 hours of various heat treated Al 7050 on the behavior on SCC was investigated by Liao [90]. They observed that for a specific heat treatment the pre-immersed sample shown high resistance to SCC than that of the sample without preimmersion. In this research work they have reported unpredicted result that peak aged condition show high resistance to SCC and resistance decreased in overaged condition. In this

work they have observed that the a passive CuO was observed when T6 sample was pre exposed thus, attributing to high resistance to corrosion where as a mixture of CuO, Cu_2O and $CuCl_2$ in aluminum hydroxide was observed for the RRA and step solutionizing treatments which results in degradation of the alloy. From the above perspective of the research work it is concluded that the main mechanism behind SCC Is attributed to hydrogen embrittlemnt.

2.2.6 Effect of pre stain on SCC

In order to relive the quench induced internal stresses, a pre-strain is generally employed to the as quenched 7xxx series aluminum alloys. In the pre strain process, incubation of the dislocation network in the matrix takes place which provides efficient sites for heterogeneous nucleation of η precipitates. In addition up on further aging provide a fast diffusion paths for the precipitation and can importantly affect the progression of precipitation which leads increase in strength [91].

Fooladfar et al has studied on the novel treatment, which include one shot-peening process between or before the two stages of aging at 120 °C for 24 h and at 160 °C for 1 h, respectively. They observed that the mechanical properties are comparable with T6 condition without effecting bulk microstructure in over-aging period. This treated sample has higher SCC resistance than the T6 condition due to dislocations generated which change sequence of precipitate formation (GP → η' → η). On Further over-aging the shot-peened sample, SCC resistance increased by producing larger size and larger inter-particle space of the grain boundary precipitates [8].

The pre-strain resulted in the generation of the equilibrium phase η (MgZn2) on the dislocation network, hence the application of pre-stain reduced the amount of solutes for the formation η' in the T6 sample, resulting in decreased mechanical properties. On subsequent aging at above 160 °C makes, the grain boundary precipitates enlarge and distributed discontinuously. In addition, precipitates generated in the vicinity of dislocations in the matrix tends to enlarge which leads to decline in strength. It also observed that the dislocation density generated during pre-strain not only advantage for the growth of GBPs but also helps in

decreasing the width of the precipitate free zones (PFZ) though solute transfer from the grain matrix to the grain boundaries[92][93].

In the work of D.wang studied the effect of severe cold rolling on the mechanical properties and SCC behavior of 7050 aluminum alloy and concluded that increase in cold reduction increases yield strength and UTS when compared to T6 condition. In addition to the mechanical properties, the SCC resistance of cold worked samples were also increased compared to that of the T6 sample, attributing to enlargement in the size and particle interval of the grain boundary precipitates [94].

Neguyen [95] proposed that the increment of the precipitate size and the associated change in sequence of precipitate formation (GP → η' → η) give rise to more homogeneous slip mode and a reduction in slip planarity. That effectively decreases the mobile dislocation and, by a greater degree, brings down the hydrogen transported to the GB in the pre- strained samples.

2.2.7 Stress Corrosion Cracking of   surface treated 7xxx alloys

It has been reported that during the various heat treatments of the 7xxx aluminum alloys several constituent phases are formed. The formation of these phases will vary in size and shapes. Generally 4 types of coarser particles or phases are formed Al-Zn-Cu, Al-Cu-Fe-Zn, Al-Si-Zn-Cu and Al-Cu-Zn-Ti-Si-Cr in 7xxx Al alloys. This coarser precipitates act as the pitting sites for corrosion and crack imitation.

There are certain Laser surface melting have been the subject of significant interest as a means of improving the corrosion performance of aluminium and its alloys. Microstructural modification resulting from relatively rapid rates of cooling compared with conventional surface treatment techniques provides the basis for property enhancement.

Yue [96]studied the effect of Excimer laser surface melting on SCC behavior. It was observed that in re-solidified laser-melted zone the original grain boundaries were altered and the corrosion causing coarse second-phase particles were eliminated. The new grain boundaries after re-solidification were free from precipitates which improve the SCC resistance. In addition to

that a layer of nanocrystalline structure of Al_2O_3 had formed at the outer surface which retards the corrosion attack.

The pitting corrosion fatigue behavior of aluminium alloy 7075 after eximer laser surface melting was studied by C. P. Chan et al [37]. LSM resulted in a reduction both in size and number of constituent particles and a alteration of the grain structure within the laser melted region resulted in improvement in corrosion. In dry fatigue condition the for LSM sample the total fatigue life was lower than that of the untreated sample. Up on the shot penning the of the LSM sample the total fatigue life was enhanced. They also observed that the shot peened LSM sample tested in 3.5 wt% NaCl solution with 48 hrs resulted in high total fatigue life than the untreated specimens with an increase of two orders of magnitude in fatigue life.

T. M. Yue et al., [39] also studied the stress corrosion cracking (SCC) behavior in a 3.5%NaCl solution employing slow strain test on the 7075 aluminum alloy after excimer laser surface treatment. They have observed that the SCC initiation resistance of 7075 aluminum alloy was appreciably enhanced when tested in SSRT using 3.5% NaCl as corrosive envirnoment. They also reported that for untreated specimen, brittle intergranular fracture was observed and transgranular fracture features were observed when both tested in anodic potential. They have also observed that Laser treatment reduced the hydrogen evolution rate when tested under cathodic polarisation conditions.

Effect of Nd:YAG laser surface treatment of aluminum alloy 7075 was studied by tm yue et al [38]. In this work LSM was done under two distinct Shrouding gas environments nitrogen and air. They observed that constituent coarse particles were eliminated and fine cellular/dendritic microstructures had formed and for the N2-treated specimen, an AlN phase observed to be present. They have concluded that in SCC test when concluded in 30 days immersion test found that untreated sample resulted intergranular cracks while laser treated in air resulted in lengthy stress corrosion cracks and a small number of relatively large corrosion pits were found. While for N2 treated samples few short stress corrosion cracks were observed attributing enhancement in corrosion initiation resistance due to presence of AlN phase which act as insulator providing barrier for the corrosion attack.

Micro arc oxidiation (MAO) treatment and plasma-electrolyte-oxidation (PEO) treatment improves the SCC resistance. Ceramic alumina coating by MAO and PEO method offered good barrier effect and improves elongation in chloride environments on meliorating the localized corrosion resistance of AA7075 aluminum alloy under long-term immersion conditions [97, 98].

2.2.8 Stress Corrosion Cracking of Weldments

Gas metal arc (GMA), plasma arc (PA) and Gas tungsten arc (GTA) widely used welding process to weld aluminium alloys. Fusion welding processes are used mostly for 5xxx and 6xxx series aluminium as they are easily weldable when compared to the high strength aluminium alloys such as 2xxx and 7xxx alloys. The main weakness of the fusion welding process (GTA/GMA/EB or LB) is that it consists of an aggregation of constituent precipitation randomly and has cast microstructure. The final microstructure and phase transformation of the welded components are depend on the filler material used in the process and also depend on the amount of heat input given during the welding process.

The invention of the solid state joining process known as friction stir welding (FSW) which was developed in the year of 1991. The joining of high strength aluminium alloys by this FSW has become much easier and this process has gained a broad application in the aircraft sector for the joining of heat-treatable aluminium alloys. The major advantage in this FSW is that it produces the final product without any distortion. Apart from FSW, the use of Power beam processes such as electron beam (EB) and laser beam (LB) welding are widely used for welding of high strength and age hardenable Al alloys in the recent years.

In the FSW process, extensive plastic deformation and flow of material assisted by the frictional heat are taking place at the weld nugget. During the FSW process, high temperature of about 480°C is obtained at the weld nugget region in some cases it has been reported that inchoate melting in the weld nugget occur due to frictional heat generated during the FSW process. The regions adjoining the weld nugget also get affected by the thermomechanical effects. Thus, the corrosion behavior of the weldment of the Al alloy is expected to alter significantly. The prior/post-weld heat treatment, phase transformations/ micro constituents in

the weld metal and/or heat affected zone and the residual stresses that develop during welding may have a vital influence on the SCC behavior. As stated earlier that 6xxx series Al alloys are less susceptible to SCC so as FSW 6xxx Al weldments alloys are also less porn to SCC and also reported that SCC of these weldments exhibits better SCC resistance than the parent metal [99]. It is reported that 2219 Al-alloy in T87 temper and its friction stir weldment in the as-welded condition were observed that are highly resistance to SCC [100]. SCC failures observed in the heat affected zone regions of 7xxx series alloy weldments have been attributed to the degree of sensitization [101].

It is reported that the FSW weldments of moderate strength Al such as 5083, 2219 and 2195 presented better SCC resistance when compared to high strength 7xxx Al alloys, on account of the favorable temper conditions, microstructural features, and corrosion behavior of different regions of the weldment. It is observed that the resistance of the weldments to SCC is influenced by the welding process and technique. In case of 2195 and 2219 Al-alloys Plasma arc welding were found to have a higher susceptibility to SCC than its FSW counterpart [102].

An electron beam weldment of alloy 7050-T7451 Al-alloy was found to be susceptible to SCC in 3.5% NaCl solution compared to its parent alloy, as assessed by constant load SCC tests at different stress levels. The higher susceptibility was attributed to the considerable level of residual stresses in the EB weldments[103]. Hatamleh et al.[104] produced friction stir welds from 7075 Al-alloy in T651 temper and evaluated the SCC behavior of this weldment with and without laser shock peening and shot-peening treatments. The temper condition of the welded plates was modified from T651 to T7351 by artificial aging. The peening treatments were aimed at altering the state of residual stress at the surface in order to improve the SCC behavior. The SSRT data summarized by the authors showed that there was no SCC of the weldments in 3.5% NaCl solution, even in the non-peened condition, which could be attributed to change in temper condition to a more stable/SCC resistant T7351.The limited available information on the SCC behavior of aluminium alloy welds indicate that the alloys welded in the stabilized temper or that were given a post-welding heat treatment may resist the environmentally induced damage.

Srinivasan[105] have investigated the SCC behavior of a dissimilar friction stir weldment that comprised 6056 and 7075 Al-alloys. In the SSRT tests performed in air and in

3.5% NaCl solution at 10^{-6} s^{-1}, the fracture was observed in the TMZ/ HAZ region of the 6056 Al-alloy, which was the weak region in the joint. Even though numerous pits were observed in the 7075 Al-alloy and also in the root region of the weld nugget, there was no SCC. However, when the test was performed at a lower strain rate (10^{-7} s^{-1}), SCC was noticed in the 7075 parent alloy, revealing the significant influence of strain rate in evaluating SCC of this dissimilar aluminium alloy weldment.

C. S. Paglia studied the effect of short term heat treatment on the friction stir welded 7075-T7451 alloys the short term heat maximum of 280 ^{o}C was applied and observed the SCC resistance increased and the fracture region transferred to HAZ to nugget[101].

Intergranular corrosion following friction stir welding of aluminum alloy 7075- T651 were studied by Lumsden et al. they have concluded that Following FSW of AA 7075-T651, weld zones were susceptible to intergranular attack. The hottest regions within the HAZ were the most susceptible to intergranular corrosion. The weld nugget and deformed region of the TMAZ also were susceptible to intergranular corrosion, but to a lesser extent than the hottest region of the HAZ. The mechanism of intergranular corrosion best correlated to a Cu depletion model linking intergranular corrosion with pitting corrosion [106].

2.2.9 Stress Corrosion Cracking behavior of 7xxx metal matrix composites.

Aluminum metal matrix composites have much more better mechanical and wear properties as compared to monolithic counterpart. The superior properties can attributed because the matrix phase reinforced with hard secondary phase in the form of particulates, whiskers or fibers. These reinforcements add their additional properties to matrix phase. But, when coming to the corrosion of metal matrix composites it's uncertain. Corrosion susceptibility may increase or decrease with the addition of the particles reinforcement and it is depend processing parameters involve in making the MMC as well as the on the metal reinforcement combination. The corrosion problems that are likely to occur in metal matrix composites (MMCs) are as follows[107]. (1) Galvanic effects between the matrix and reinforcing phase,(2) Selective

corrosion at the matrix/ reinforcement interface,(3) Corrosion caused due to defect during manufacturing of matrix.

MMC are manufactured with incorporating the ceramic particles or insulating particles such as boron, alumina and silicon carbide etc., little or no galvanic reaction between reinforcement particles and the aluminium matrix would be expected, but, when manufacturing the MMC, a strong interfacial phase is formed which binds the matrix and reinforcement . If this interfacial phase behaves as cathodic or anodic potential then it may favor for corrosion to occur. This corrosion leads to pit formation and act as a crack initiation site, as when load or stress applied leads to SCC failure. Further aging of this high strength heat treatable Al MMCS has a profound effect on the SCC behavior. Another reason for SCC failures of MMCS attributed to buildup of a very huge dislocation density due to presence of immssiable reinforcement particles which raises the stress concentration at the interface, and may favor for fast dissolution of atoms in the composite than compared to metal alloy and also de-bonding between the matrix/interface would support the mechanism of stress concentration at the interface in the stimulation of the corrosion process[108].

The effects of ageing heat treatment on the stress corrosion cracking resistance of SiCw-A1 7075 MMC were studied in chloride solutions [109]. They observed that the resistance to pit initiation was same for both monolithic alloy as well as the SiCw-Al 6061 MMC. Up on initiation of pit further damage will proceeds by formation of crevices between the matrix and the reinforcement and by the dissolution of the latter in the pits. While for Al 7075 metal matrix composite, aging at 170 °C for more than 1 h subsequent ageing at 110 °C made MMCs resistance to SCC due to formation of precipitates adjacent to the SiCw-A1 7075 interface make them noble.

S.L. Winkler [110] studied the SCC behavior of 7xxx Al–6%Zn–1% Mg and Al– 6%Zn–1%Mg–1%Ag (7xxx) MMCs reinforced with Al_2O_3 fibers. It reported that Ag has significant role in SCC resistance in MMC. It has observed that MMC containing Ag has higher resistance to SCC as compared to the MMCs without Ag and also stated that the pitting tends to initate at the fiber/matrix interfaces due to galvanic effect between the Fe-rich particles and Ti-rich at the interface and the matrix. SCC in MMC initiate due to microsegregation of the Mg at the

matrix/fiber interface which increase the transportation of hydrogen making the composite brittle. Furthermore, investigation of facture surface of MMCs suggests that both the anodic dissolution and hydrogen embrittlement mechanism are engaged in stress corrosion crack initiation and propagation. Also observed that the SCC occurred due to microsegregation of Mg at the fiber/ matrix region which enhances Hydrogen transportation hence embrittles the composite.

2.3 Motivation

Based on the literature survey, it is evident that the research has been done on the SCC behavior on various heat treated condition but, the effects of cold working (CW) and annealing on the tensile and SCC behavior of 7075 Al alloy were very scarce. The present research work focuses on the comparative analysis of tensile and SCC behaviors of 7075 alloy through applications of cold rolling with varying degree of deformation and subsequent annealing at different temperatures. This study will help in understanding the susceptibility of SCC on various thermo mechanical treatments.

The LSM of 7075 Al-alloy under peak aged condition utilizing conventional YAG, Eximer and CO_2 lasers showed great promise in improving corrosion resistance, adoption of small laser beams with overlapping of tracks pose certain inherent disadvantages to apply in actual industrial applications. Lasing with large sized beam with elimination of overlapping can effectively avoid detrimental affects at overlapped regions and thereby enhance structural homogeneity in re-solidified layer and thereby reduce SCC and pitting corrosion effects. As the corrosion performance is very sensitive to inhomogeneities, significant overlap may degrade the corrosion properties. Furthermore, elimination of overlapping with enhanced coupling (especially possible with diode laser HPDL) further facilitate in fast processing time and high production efficiency.

From the literature study there is a research gap to study the effect of cold working (CW) and annealing on the corrosion behavior and it is also observed that their very scarce study has been done on the application of HPDL with large beam spot without over lapping of tracks on the corrosion behavior of 7075 Al alloy. The present study fulfills the scarcity lacking in the previous

research works. In addition, in the process of laser surface melting the microstructure altered to maximum extent observed from the extensive literature study. It is well known that in the process of LSM, removal of hard primary precipitates present in wrought microstructure leads to decrease in mechanical properties such as hardness. In order to enhance surface properties like hardness preserving corrosion resistance as compared to the untreated alloys, motivated to carry out laser surface cladding with ceramic powders.

It is difficult to draw the temperature profiles on the treated surface as the high temperature developed due to coupling efficiency of high power diode lasers with aluminum alloys. In order to predict the change in temperature thermal stress fields developed in the heated region and cooling rate of laser modified surface with various laser processing conditions has motivated to do numerical simulation using COMSOL multiphysics.

2.4 Problem identification

To study the comparative analysis of tensile and SCC behavior of 7075 alloy by using cold rolling with varying degree of deformation and subsequent annealing at different temperatures. In addition, application of HPDL with large beam spot without over lapping of tracks on the corrosion behavior of 7075 Al alloy.

2.5 Objective of Research Work

The main objective of this research work to find the corrosion behavior in bulk material by thermo-mechanical treatments and through the surface modifications with application of lasers heating. Following objectives are formulated in 2 phases for the present work.

Phase I objectives

- To study the effect of thermo-mechanical treatments on the Tensile Properties of 7075 Alloy Aluminum.
- To study the effect of thermo-mechanical treatments of 7075 Aluminum alloy on the corrosion and stress corrosion cracking behavior.

Phase II objectives

- To study the effect of laser surface modification such as laser surface melting and laser surface cladding on the corrosion properties of 7075 Al alloys
- To develop a theoretical model using computer simulation for the laser surface melting and to study the temperature evolution and thermal stress generated on the treated surface during the laser surface melting process.

2.6 Chapter summary

The understanding of corrosion behavior possesses critical challenge for 7075 Al alloy. The main aim of this literature survey is to understand the effect of constituent alloying elements on the response of microstructural variation in various heat-treated conditions on corrosion behavior. Further, literature survey done on to factors which are improving the corrosion resistance using thermo-mechanical treatments and by surface modifications of 7xxx alloys . The effect of stress and pre-strain, effect of constituent alloying elements in the alloy, and the effect of environments on corrosion behavior. In addition, the SCC behaviors of weldments, 7xxx metal matrix composites and laser surface modifications thoroughly reviewed. Literature on methods for the carrying out various treatments such as thermo-mechanical treatments and laser surface modifications has been complied. The problem identification has been done and objective for this research work has been ascertained.

CHAPTER 3

Experimentation

3.1   Introduction

In this chapter, the materials and methods used for the experiments are discussed in detail. The first phase includes the materials and methods used to carry out the thermo-mechanical treatments and the instruments used to carry out various corrosion tests. In the second phase, the processing methods and various process parameters used to carry out the laser surface treatment and laser surface cladding are discussed. In the final section, the numerical equation and methods adopted for the computer simulation for the LSM are discussed.

3.2 Experimental procedure to carry out thermo-mechanical treatment of 7075 Al alloy and methods adopted to study corrosion behavior

3.2.1   Tensile test

The nominal chemical composition of 7075 Al alloy is presented in table 3.1. The initial condition of the material was in peak aged condition, with the plate thickness of 6.35 mm. The alloy was very hard to cold rolled in the as received form. Therefore, the as received material was full annealed. Full annealing was carried out at the temperature of 415 ^{o}C for 150 min followed by furnace cooling. This is to bring the peak aged temper condition to O – temper condition. This O- tempered 7075 Al alloy was considered as the starting material(SM) in this work.

Composition	Zn	Mg	Cu	Fe	Si	Cr	Mn	Ti	other	Al
Wt%	5.5	2.4	1.3	0.16	0.05	0.23	0.03	0.071	0.15	bal

Table 3.1: Nominal chemical composition (wt%) of 7075-T6 Aluminum alloy

Cold working (CW) was carried out by use of a Lab Mill and the O-tempered samples was reduced to with various thicknesses, which involved: (a) thickness reduction from 6.3 to 5.5 mm (12% CW), (b) thickness reduction from 6.3 to 5 mm (19% CW), (c) thickness reduction from 6.3 to 4.4 mm (28% CW). Further, the cold rolled (CR) samples were subjected to different final annealing temperatures of 225 ^{o}C , 275 ^{o}C and 325 ^{o}C for 5 min in muffle furnace. The annealed plates were air cooled to the ambient temperature. The schematic representation of the treatment followed, shown in the figure 3.1.
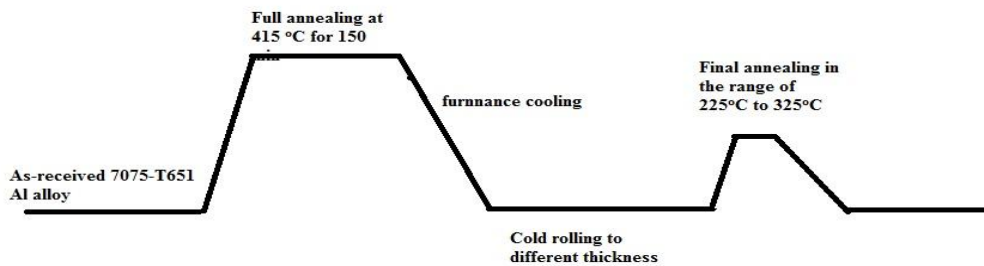
Figure 3.1: Schematic representation of the heat treatment cycle followed

Tensile samples were prepared along the transverse direction of the plate and were prepared according to ASTM E8 sub-size standard. The dimensions of the tensile sample are 20 mm X 6 mm X 4 mm with gauge length of 20 mm as shown in figure 3.2. The test was conducted on the SAHIMADZU universal testing machine with a crosshead speed of 2 mm / min.
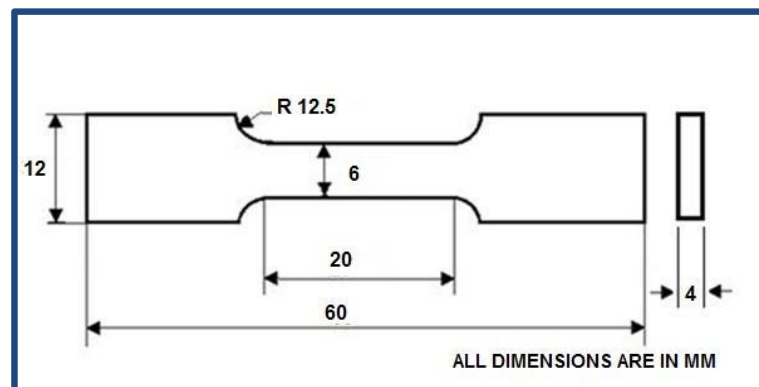

Figure 3.2: Tensile specimen dimensions

Strength and ductility parameters were calculated from the tensile test. The engineering stress and engineering strain were evaluated from the extension data and load applied in the tension test. Then true stress and true strain were evaluated from the equation 3.1 and 3.2.

$$\varepsilon = \ln(1+e) \qquad \text{Eq. (3.1)}$$

$$\sigma = s(1+e) \qquad \text{Eq.(3.2)}$$

Where e and s are engineering strain and stress respectively, ε and σ are true strain and strain. True stress-strain curve know as flow curve expresses a true indication of deformations properties since it is based on the instantaneous dimension of the specimen. The flow curve in uniform plastic deformation can expressed by simple power law as shown in Eq. 3. 3

$$\sigma = K \varepsilon^{n} \qquad \text{Eq. (3.3)}$$

Where K is the strength coefficient and n is the strain-hardening exponent. The K and n defined in a log-log plot of true stress and strain curve in the region between yield point to UTS which results in a straight line in that the slop of the line gives the value of n where as K is the true stress at $\varepsilon = 1.0$.

Micro hardness test was carried out on HVS-20 SHIMADZU micro hardness machine with a load of 10 Kgf for 15 sec. Fracture surface of the broken specimens from the tensile test of various cold worked samples were taken for the fractographic study using scanning electron microscope (SEM).

3.2.2 Corrosion test

Slow Strain Rate Testing (SSRT) is carried out by using Constant extension rate testing (CERT) to evaluate SCC behavior of thermo-mechanical Al alloy in an 3.5% NaCl alkaline solution. The SSRT testing machine is shown in figure 3.3. The SSRT samples were prepared according to ASTM E8 sub size standard. The dimensions of the tension sample were taken as 20 mm X 6 mm X 4 mm with gauge length of 20 mm. In the present work, the SSRT test was carried out with the corrosive of environment pH of 12. In order to attain desired level of Ph, solution of NaOH was added to the 3.5% NaCl solution. The strain rate of the constant extension rate-testing machine was set to 4×10^{-5} s^{-1} and initially preloaded of 50 kg was set. The ASTM G 129- 95 standards was adopted to evaluate the resistance of metals to environmentally assisted cracking (EAC) in slow strain rate test (SSRT).

The SSRT index is used to measure the SCC resistance and is defined as the ratio of elongations of the samples tested in the 3.5% NaCl solution to that of elongations of the samples tested in the air. The higher value of E_{sol}/E_{air} indicates high resistance to SCC. The standard conventional electrolytic cell was used to carry out potentiodynamic polarization tests and potentiostat used to measure the electrochemical measurements and polarizations scans. Figure 3.4 show the electrochemical work station used to carry out the potentiodynamic polarization test. Metallographic samples were prepared for all the conditions. The specimens were mounted and ground on the various grit papers followed by disc polishing by using 1-micrometer diamond paste. The keller's reagent was used as etchant to reveal the microstructure. XRD analysis was carried out to find the phases present. Fracture surface of the deformed sample from the tensile test and SSRT test were taken for the fractographic study using scanning electron microscope (SEM).

Figure 3.3: Slow Strain Rate Test unit. (a) Extensometers (b) vessel carrying corrosive media (c) Computer attachment to record deformation data
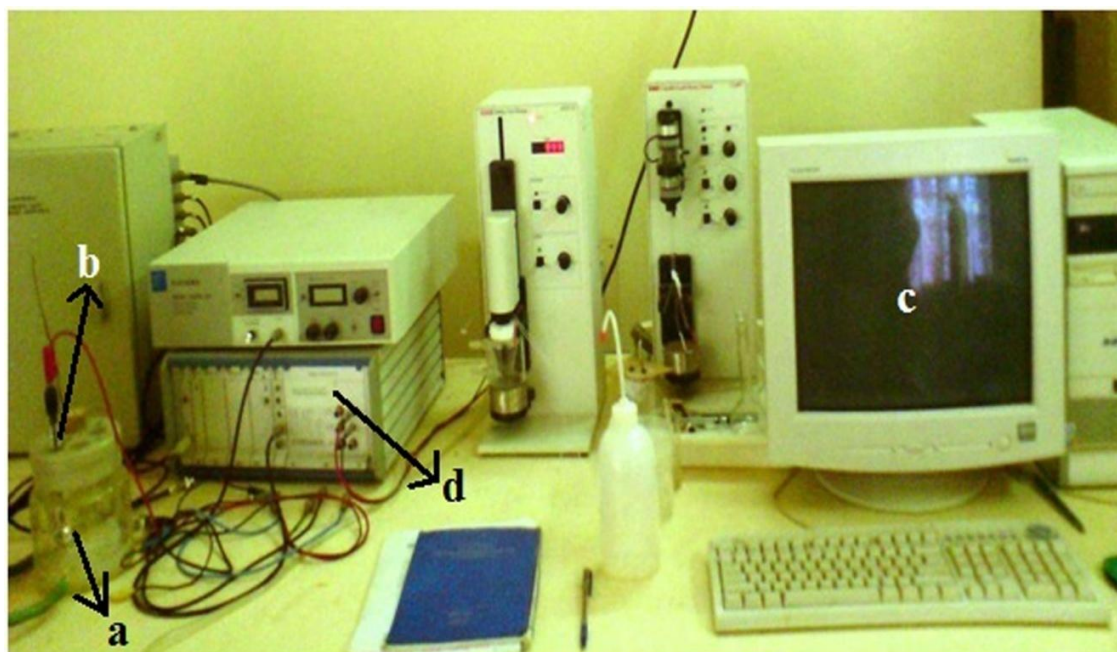

Figure.3.4: Shows the electrochemical work station (a) Electro-chemical cell (b) Electrodes (c) computer to record corrosion data (d) Potientostat.

3.3. Experimental procedure for Laser Surface Treatment and methods adopted to study corrosion behavior

3.3 .1 Laser Surface Melting

The 7075-T651 aluminum alloy plate was irradiated under a multi-mode (Gaussian in fast axis and top-hat in slow axis) diode laser beam of size 20 mm X 5 mm. Figure 3.5 shows the laser processing setup utilized for experimentation. The setup constitutes a 6-kW maximum power deliverable continuous wave fiber-coupled diode laser system integrated to 8-axis robotic workstation. It is pertinent to mention here that diode laser whose wavelength is 890-980 nm can potentially induce high coupling efficiency to aluminum-based materials and thereby facilitate high process efficiency. Laser parameters used for laser surface modifications are shown in table 3.2.

The sample was fixed to the working table and the laser beam carried through fiber connected to the sixth arm of Robot is traversed at a constant laser powers and with scanning speeds as shown in table 3.3. Laser melting has been carried out at fixed working distance of 300 mm to uniformly focus laser intensity distribution throughout the experiments. The laser energy densities are calculated using Eq. 3.4, dependant on process variables laser power (W), spot size (mm) and scanning speed (mm/s).

Figure 3.6 and 3.7 shows the schematic of laser surface melting process. A nitrogen shroud at 2-bar pressure through a specifically designed and fabricated 25 mm X 5 mm off- axis nozzle was used to effectively shield during laser processing against atmospheric contamination. Apparently, nitrogen shielding also provide advantage of diffusing nitrogen in the laser melted layer as anticipated in previously reported studies [38]. The laser treatments were carried out along the transverse direction of the plate perpendicular to the rolling direction. Table 3.3 elucidates the LSM process parameters utilized for experimentation.

$$Laser\ energy\ density\ = \frac{laser\ power}{[processing\ speed * laser\ spot\ width]} \qquad \text{Eq. (3.4)}$$

Figure 3.5: Laser processing setup utilized for experimentation
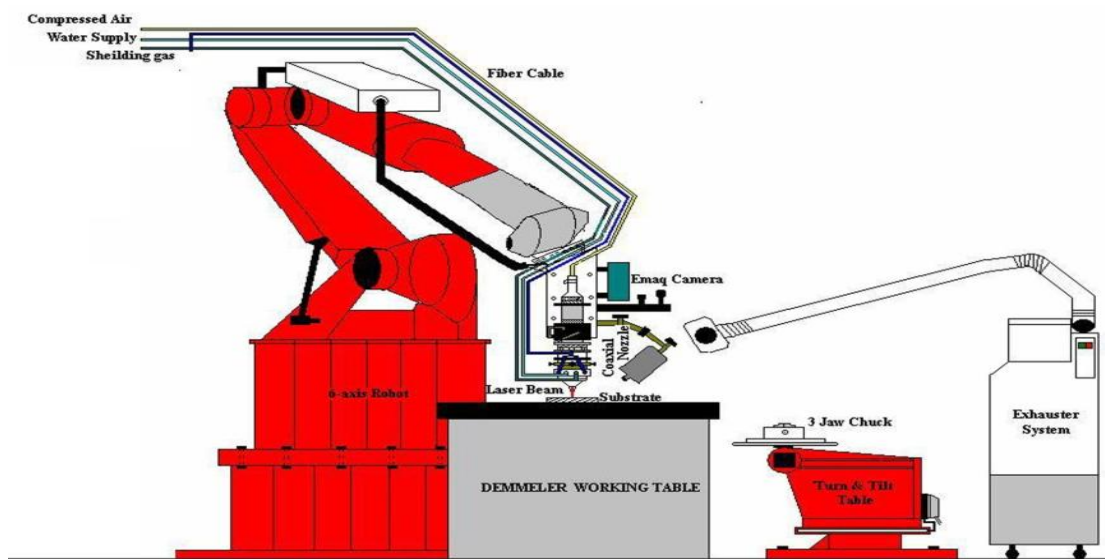
(a)
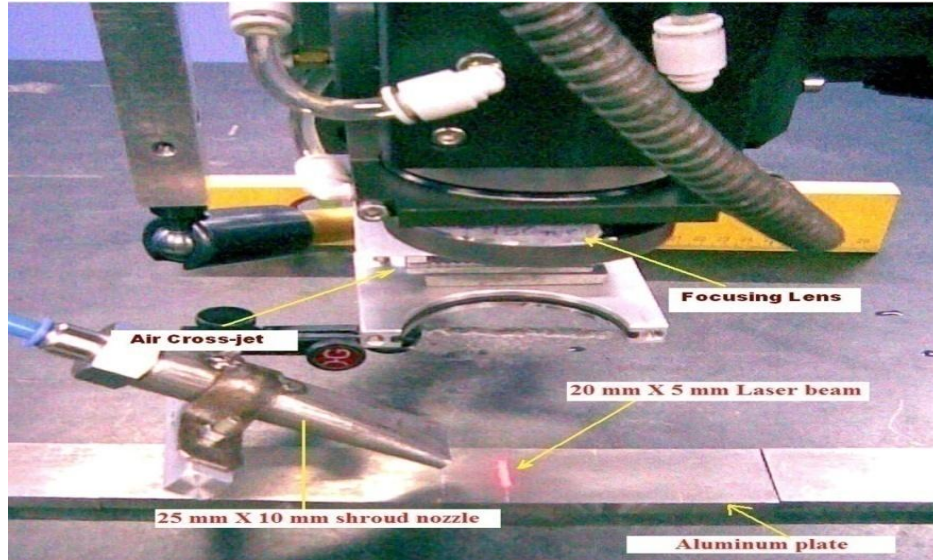
(b)

Figure 3.6: (a) Schematic view of Laser processing setup utilized for experimentation, (b) Diode laser surface melting setup (closer view) includes laser beam of 4kW power impending from focusing lens. Laser beam shroud with N2 gas coming from shroud nozzle and an Al 7075 plate.

Figure 3.7: (a) Schematic of laser surface melting (b) the shape and size of the focused laser beam with laser intensity distribution.

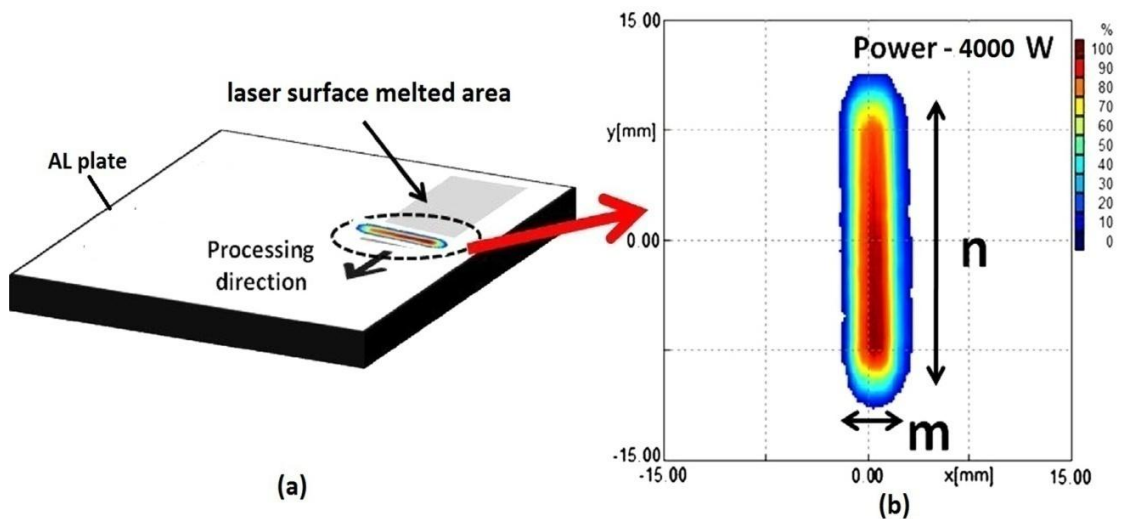|	Properties	values
1	Wave length	890 – 980 nm
2	Spot Size	20 mm X 5 mm
3	Fiber	1000-µm (NA:0.22)
4	Shroud	N_2 (2-bar)
5	Working Distance	300 mm
6	Substrate	7075 Al-alloy (T-6)
7	Surface condition	Grinded

Table 3.2: Laser parameters used for laser surface melting experiment

Sl.no	Laser power [W]	Scan speed [mm/s]	Heat input[J/mm]	Laser energy density[J/mm^2]
1	4000	10	400	80
2	4000	5	800	100
3	3000	5	600	120
4	3000	4	750	150
5	3000	3	1000	200

Table 3.3: Laser process parameters used for LSM experiments.

3.3.2. Characterization of Treated Layers

After laser surface melting, treated layers were sectioned utilizing a low-speed cutting saw and cross-sectional metallographic specimens were prepared applying standard metallographic procedure. The sectioned surfaces and cross-sections of the laser-melted layers were analyzed for case depth, microstructure and phase composition utilizing light microscopy (LOM). Keller's reagent was as etchant to delineate microstrucural variations in melted, fusion boundary, heat affected zone and unaffected substrate regions. Micro hardness measurement has been carried out on the cross-section of the sample using 50gf load force and with dwell time of 10 s. Further to analyze in depth microstrucural features in the laser melted layers, high magnification Scanning Electron Microscope (SEM) analysis has been carried out under BSI and SEI modes. Few samples were also analyzed for compositional variations in microstructures of laser treated layers by subjecting spot analysis and area mapping utilizing Energy Dispersive Spectrometry (EDS) attached to SEM. Phase constitution of laser treated as well as untreated surfaces was analyzed by X-ray diffraction technique scanned in the 2θ ranging from 10 – 80 deg utilizing a X-rays generated with Cu target. The phases obtained in each case were identified and analyzed utilizing standard PDF cards. In order to understand corrosion mechanism, few samples were also subjected to surface morphological and compositional analysis utilizing SEM of laser melted and untreated surfaces before and after corrosion testing.

3.3.3 Corrosion Testing

In order to evaluate and compare corrosion behavior of laser melted surfaces processed under different conditions and untreated surfaces, electrochemical measurements were performed employing a conventional three-electrode system in 3.5% NaCl (neutral pH) solution purged with nitrogen gas carried out at room temperature conditions. For the purpose, centrally sectioned laser treated surface covering 10 mm X 10 mm area was exposed as working electrode, whereas platinum electrode was used as counter electrode and SCE electrode as reference electrode. Electrochemical interface (SI1287) combined with Impedance/Gain phase analyser (SI 1260) retrieved from *Solartron* was used for both Potentiodynamic polarization and Impedance

after obtaining OCP approximately   at 30 minutes. The polarization plots were obtained by applying potentials between -1.5 to -0.5V Vs SCE with a scan rate of 1mv/sec. Impedance measurements were carried out for both laser treated and untreated surfaces utilizing the same instrument before potentiodynamic polarization scan. The E_{corr} and I_{corr} and corrosion rates are obtained from R_p fit method [112].

The EIS experiment was conducted within a frequency range of 100000 to 0.1Hz by applying a AC signal with 10 mV amplitude. The potentiodynamic polarization plots were generated and compared to analyze corrosion rates in case of laser-melted and untreated surfaces.

The impedance measurements of the EIS experiment were depicted as Nyquist plots as well as bode plots. The EIS plots for specimens tested at OCP were used to define loops in both high-frequencies as well as low-frequency ranges. To interpret the electrochemical behavior of the EIS spectra, suitable equivalent circuits consisting of resistance, capacitors and other circuit elements were constructed and analyzed.

3.4 Experimental procedure for Laser cladding

Laser surface cladding is carried out to improve the surface properties of Al 7075 alloys. Initially grooves of dimensions 150 mm X 22mm X 0.2 mm on the surface of Al 7075 alloy plate where prepared as shown in figure 3.8. A paste of poly-vinyl-alcohol and powders are prepared and then painted in the grooves to forms uniform coat thickness as shown in figure 3.9. The laser heat in put was applied over the painted surface. The laser parameters utilized for laser cladding are same as that of the laser parameters used in LSM operations. The processing parameters used for laser cladding are presented in table 3.4. The processing parameters are chosen as per the feasibility of the laser processing machine. The microstructure, hardness and corrosion properties evaluated after laser cladding and compared with the laser melting samples as well as as-received sample.

Figure 3.8: illustrate the grooves prepared on the 7075 Al alloy prior to the coating of powders.

Figure 3.9: illustrates the painting of mixture of ceramic powders and poly-vinyl-alcohol in the prepared grooves.

Sl.no	Laser power [W]	Scan speed [mm/s]	Powders used
1	3000	5	Graphite powder (30-40 μm)
2	4000	10	B_4C (30-40 μm)
3	4000	10	Al_2O_3(30-40 nm)

Table 3.4: parameters used for laser cladding

3.5 Computer Simulation

The 3-dimentional heat transfer simulation model was built in COMSOL Multiphysics. The variation in temperature profiles, cooling rates and thermal-stress developed in the treated region for several laser processing conditions were predicted using this simulation model. The Equation 3.5 determines the heat transfer equations used in this simulations. Whereas Equation 3.6 gives addition of Gaussian shape energy distribution in Eq 3.5.

$$\rho C_p \frac{\partial T}{\partial t} + \rho C_p \, u\nabla T = \nabla.(k\nabla T) + Q \qquad \text{Eq. (3.5)}$$

$$Q = Q_0 * \frac{A_c}{(\pi * r_b{}^2)} * e^{-2[((x-x_c)/r_b{}^2)^2 + ((y-y_c)/r_b{}^2)^2]} \qquad \text{Eq. (3.6)}$$

Where ρ is the density of material in kg/m^3, c_p is material specific heat in J/kgK, k is the thermal conductivity (W/m K), Q (W/m^2) is the heat flux, Q_0 is laser power density applied to the material (W/m^2), A_c is absorption coefficient, r_b radius of laser beam, x and y are the axis of the coordinates system.

Figure 3.10 shows the spatial arrangements of laser sources used in this work. The shape and size of simulated beam is constructed in way that resembles the experimental beam. The simulated beams consist of seven superimposed circular sources in a two-dimensional array with radius $r_b =$ 2.5 mm and has an equivalent power share shown in figure 3.11.
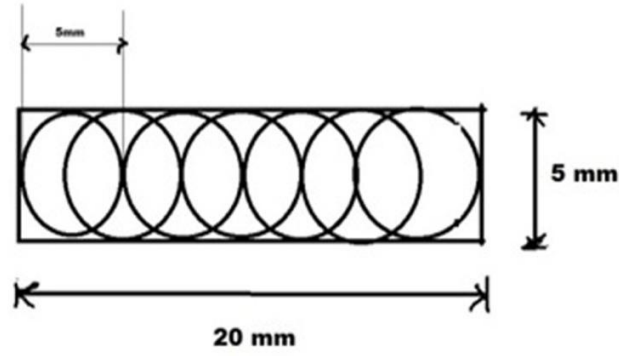

Figure 3.10**:** Arrangement of laser beam spot sources in the modeling work.

The heat transfer solution from the Equation (3.5), can be refitted to the following expression for seven beam sources used in this work.

$$\rho C_p \frac{\partial T}{\partial t} + \rho C_p \, u\nabla T = \nabla.\,(k\nabla T) + Q_{01} + Q_{02} + \cdots \dots + Q_{06} + Q_{07} \qquad \text{Eq. (3.7)}$$

$$\text{Where, } Q_{01} = Q0 * \frac{A_c}{(\pi * r_b{}^2)} * e^{-2[((x-x_1)/r_b{}^2)^2 + ((y-y_1)/r_b{}^2)^2]}$$

$$Q_{02} = Q0 * \frac{A_c}{(\pi * r_b{}^2)} * e^{-2[((x-x_2)/r_b{}^2)^2 + ((y-y_2)/r_b{}^2)^2]}$$

$$Q_{03} = Q0 * \frac{A_c}{(\pi * r_b{}^2)} * e^{-2[((x-x_3)/r_b{}^2)^2 + ((y-y_3)/r_b{}^2)^2]} \dots$$

$$\dots Q_{07} = Q0 * \frac{A_c}{(\pi * r_b{}^2)} * e^{-2[((x-x_7)/r_b{}^2)^2 + ((y-y_3)/r_b{}^2)^2]}$$

Q_{01} is the first laser spot volumetric heat source term, Q_{02} is the second laser spot volumetric heat source term, and Q_{03} is the source term due to the third spot and so on until seventh spot,

respectively. The loci of the intensities are changed with respect to scan speed by changing the x and y coordinates in the Gaussian field equation.

x_1 and y_1 are the distance between the origin of the coordinates system and first beam center, x_2 and y_2 are the distance between the origin of the coordinate system and the second beam center along the x and y coordinate respectively. In a similar fashion, the beam centers were constructed by varying the distance between beam centers coordinates from the origin. The seven volumetric source terms are constructed as shown in figure 3.10 and are add up due to form the linearity of the model to form equation 3.7.

Figure 3.11 shows the power density distribution for simulated laser beam profile. In this work, The rectangular beam spot resembles a top-hat profile in y–x plane is constructed which is approximately similar to the experimental beam profile.
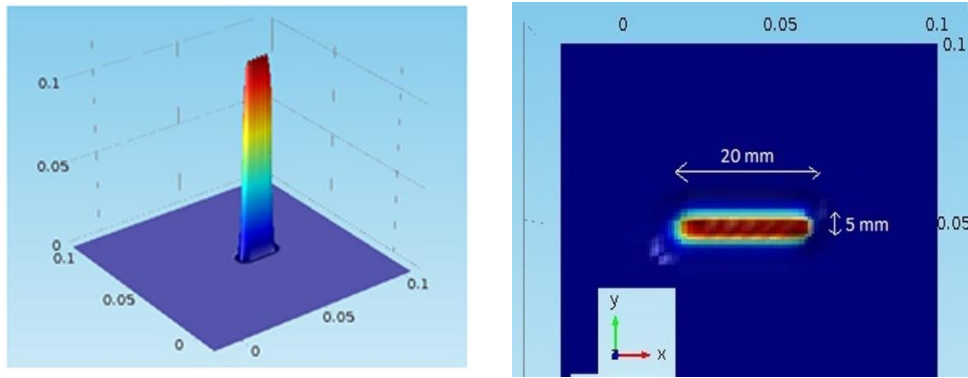

Figure 3.11: Power density distribution resembling top hat rectangular beam profile.

During the phase transition, the total quantity of heat absorbed per unit mass of the material under investigation is indicated by change in enthalpy ΔH. Further, the equivalent specific heat capacity C_{p1} (Equation 3.8) is used to express the influence the latent heat during phase change by relatively assuming melt occurs within $T_m - dT_m = T_m + dT_m$ with the addition of Gaussian function δ (Equation 3.9) centered at melting point Tm.

$$Cp1 = Cp + \delta\Delta H + \left(\frac{\Delta H}{Tm}\text{-}\right)Z((T - Tm), \Delta T) \qquad \text{Eq. (3.8)}$$

$$\delta = \exp\left(\frac{(-T-Tm)^2}{(\Delta T)^2}\right)/\Delta T\sqrt{\pi} \qquad \text{Eq. (3.9)}$$

ΔH is the latent heat of change; T and Tm are instantaneous and melting temperatures, respectively. ΔT represents the phase transition temperature range, and Z is the smooth Heaviside function [113]. The constant properties used for this simulation are listed in table 3.5.

The boundary conditions followed in this simulation are shown in figure 3.12 (a) and defined in table 3.6. The boundary 4 of the model undergo exposure to the laser beam, convective cooling, and surface-to-ambient radiation simultaneously (Eq. (3.9)).

$$K\frac{\partial T}{\partial z} = Q - h[T - T_0] - \varepsilon\sigma[T^4 - T_0^4] \qquad \text{Eq. (3.9)}$$

Where h is the heat transfer coefficient. The high value of heat transfer coefficient is applied in the present simulations across the heated spots (h = 9000 W/m^2 K) due to the jet injection. The natural convection is considered on the surrounding sides of the sample (h = 50 W/m^2 K) to account for the cooling. The high value of heat transfer coefficient at the free surface of the work piece is due to the assisting gas jet impingement at the surface. The emissivity, ε of treated alloy as function of temperature given in table 3.5 [114] and σ is the Stefan– Boltzmann constant (σ = 5.67 X 10^{-8} W/m^2 K^4)

A fine mesh is best for obtaining more precise results. Unfortunately, the finer the mesh, would take the longer time for the completing simulations. It was essential to observe the heat transfer effects at the location of the track and its immediate surrounding region. Therefore, the area with the proximity of the laser track was designated with the highest level of predefined meshes (extremely fine). The remaining model is subjected to normal mesh shown in figure 3.12(b).

Property	Symbol	Value
Thermal conductivity	k	130 [W/(mK)]
Absorptivity[a]	A	0.2
Density	ρ	2.8×10^3 [Kg/m^3]
Melting temperature	T_m	660 [^{o}C]
Vaporization temperature	T_v	2519 [^{o}C]
Latent heat of melting	ΔH	390 [J/g]
Latent heat of vaporization	Lv	10,900 [J/g]
Emissivity(as a function of temperature)	ε	$(7.2*10^{-5})*T + (3.2*10^{-3})$[114]
Coefficient of liner expansion	α	25.2 [1/K]
Half-width of the temperature curve	ΔT	30

[a]Approximate value selected based on different values used in the literature.

Table 3.5 : Properties and values used for 7075 Aluminum alloy.

Description	Boundary	Boundary condition	Variable
Laser source	4	Heat Flux	Q
Radiation	4	Surface-To-Ambient	ε
Convection cooling	1 ,2,5,6	Convective Cooling	h
Insulation	3	Insulation	-

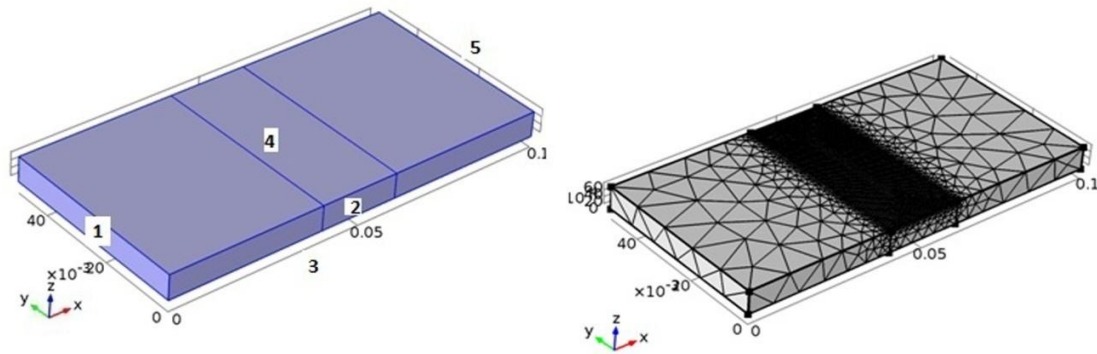**Table 3.6**: Boundary conditions applied to the model

Figure 3.12. (a) Illustrating the boundary conditions of the sample (b) Meshing of the model.

Apart from thermal analysis, thermal stress analysis was simulated in this model. The bottom of the plate was constrained and the rest of the plate has no constraints. It is well known that temperature increment of a material changes its volume that accompany changes in the thermal strains. These thermal strains normally accounted for stress analysis through a temperature dependent differential thermal expansion coefficient. Von Mises (equivalent stress) stresses are calculated and presented in this simulation to find the coupled effect of thermal and stress analysis.

3.6 Chapter Summary

In this chapter all the materials and methods for carrying out various experiment such as corrosion behavior of 7075 Al alloys. The experiments and processing parameters used to carry out Laser surface modifications are discussed. This chapter gives detailed information on the equipments and machinery used to characterize and analyze the results. In addition, the numerical equations used to construct the laser surface melting simulations are discussed.

CHAPTER 4

(a)   Results and Discussion on Effect of Cold Rolling and Subsequent Annealing on The Stress Corrosion Cracking Behavior of 7075 Aluminum Alloy

4.1 Introduction

The objective of this chapter is to compare and analyze the effect of cold rolling and subsequent annealing on the mechanical and corrosion properties of 7075 aluminum alloy. The mechanical properties such as strength and ductility parameters were evaluated through tensile test and the corrosion properties were determined from the slow strain rate test and potentiodynamic polarization test carried out in 3.5 % NaCl solution. Further, the objective of this chapter extended to understand the influence of cold rolling and annealing on the dislocations generated during the cold working processes and their effect on the corrosion properties.

4.2 Microstructure

Figure 4.1 (a) illustrates the microstructure of the starting material (O-tempered condition) where as the figure 4.1(b) shows the microstructure of 12 % cold rolled sample (without final annealing). It was observed that on cold rolling of the starting material the width of the grains decreased and its length were increased along rolling direction. Figure 4.2 illustrates some of the microstructures of cold deformed and subsequent annealed samples. It was observed that the with the increase in the percentage of cold deformation the aspect ratio (length/width of the grain) has been increased. Further, it was observed with high final annealing temperature of about 325°C, the width of the grain increased owing to recrystallization as can seen from figure 4.2(c) and (e).
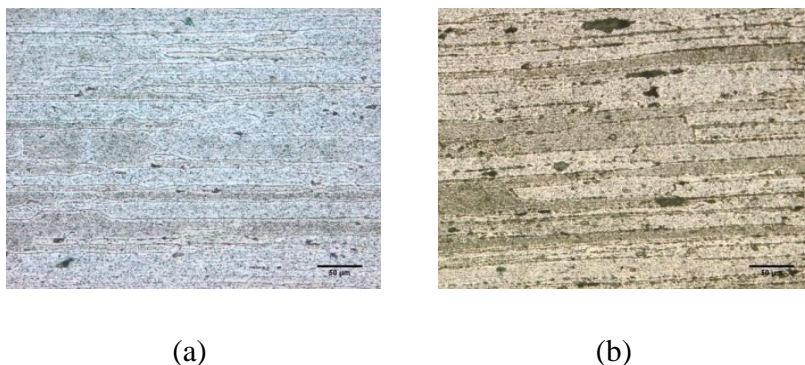

(a)   (b)

Figure 4.1: (a) Microstructure of fully annealed that is O – tempered condition at 20 x magnification. (b) 12% cold rolled without final annealing.
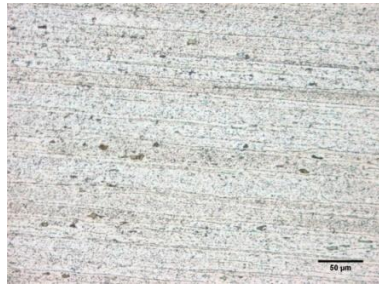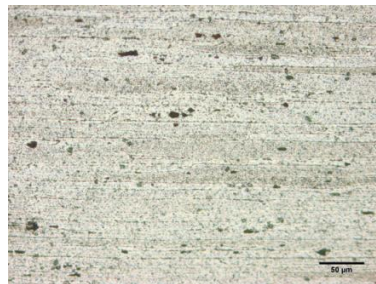
Figure 4.2: (a) Cold rolled at 12 % and annealing at 225 ^{o}C (b) Cold rolled at 12 % and annealed at 275 ^{o}C, (c) Cold rolled at 12 % and annealed at 325 ^{o}C, (d) Cold rolled at 28 % and annealed at 225 ^{o}C (e) Cold rolled at 28 % and annealed at 325 ^{o}C .

4.3 Tensile test

The mechanical properties where drawn from the stress – strain diagrams as shown in figure 4.3. The strength and ductility parameters along with the micro hardness of cold rolled (CR), cold rolled and subsequent annealed (CR+Rex) samples were presented in table 4.1. Figure 4.4 illustrates the influence cold deformation on UTS, YS and hardness. It was observed that the UTS, YS and hardness were increased with increase in % of cold deformation. Whereas from figure 4.4 (b) the elongation tends to decrease with increase in degree of cold deformation. The increase in mechanical properties were attributed to the dislocations generated in the process of cold working.

Figure 4.5 illustrates the effect of cold rolling and subsequent annealing on the strength properties. It was observed that the UTS and YS decreased with increase in the final annealing temperatures for example sample undergone thermo-mechanical treatment of 12% cold deformation and annealed at 225°C has higher UTS (sample E ; UTS= 248 Mpa) then the sample having same degree of deformation and with final annealing of 325°C. In addition, it was observed that the hardness has been decreased with increase in final annealing temperature as illustrated in figure 4.6 and 4.7. The decrease in mechanical properties such as YS, UTS and hardness on recrystallization were attributed to decrease in dislocations density resultant from high recrystallization temperatures applied to the samples. Influence of dislocation density on the yield strength (σ_y) of alloys can be explained through the Taylor equation (Eq. 4.1) [115, 116] .

$$\sigma_y = \sigma_0 + \alpha M^T Gb\rho^{1/2} + 0.85\ M^T Gb\ ln\ (x/b)/\ 2\pi\ (l\text{-}x) \qquad Eq.\ (\ 4.1)$$

Where σ_0, α, G, b, M^T ,ρ, x and l are friction stress, a constant, shear modulus, Burgers vector, Taylor factor, dislocation density, average size of precipitates and the inter-particle spacing respectively . From the Eq. (4.1) it is apparent that yield stress of the material is directly proportional to its dislocation density. This attributes the yield stress of the 7075 Al alloy drops due to decline in dislocation density resulting from recrystallization. Further, the elongation has

been observed to increase with increase in annealing temperatures as elongation is very sensitive to the recrystallization, as seen from the figure 4.6.
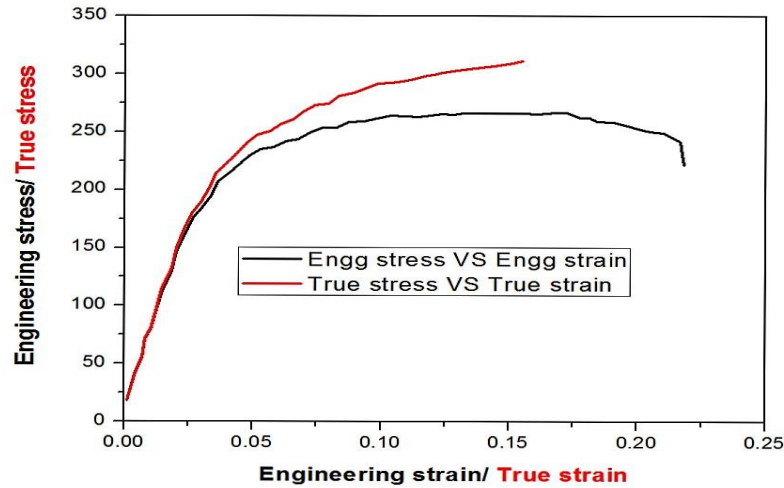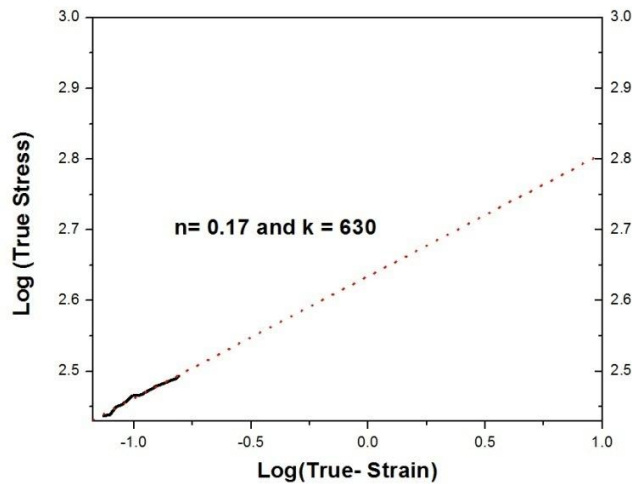

(a)

Figure 4.3: Evaluation of strength and ductility parameters of the sample 28% CW +ReX For 325 ^{o}C/5min (a) Engineering stress- stress and True stress- strain diagram (b) Log – Log plot of true stress – strain, slop of Log – Log plot of true stress – strain gives n where K is the true stress at ε = 1.0.

|	Specimen no.	Condition	Hv	UTS (MPa)	YS (MPa)	UTS/σ$_y$	% TE	% RA	% UE	n	K (MPa)
A	SM	450 ºC for 150 min	68	221	200	1.105	25.5	18.5	17	0.12	812
B	CW 12 %	12% CW	88.7	251.3	241.12	1.04	21	19.7	11	0.18	645.6
C	CW 19%	19 % CW	91.62	273.2	257.47	1.06	20.17	18.55	11.37	0.21	923
D	CW 28%	28 % CW	94.3	276.4	263	1.05	19.3	21.33	10.1	0.21	892
E	Tmt1-A1-1L	12% CW +ReX For 225 ºC/5min	82.9	248	230	1.05	21.8	19.8	11.07	0.17	588
F	Tmt1-A2-1L	19% CW+ReX For 225 ºC/5min	85.02	267	245	1.08	23	23.23	14.17	0.26	1000
G	Tmt1-A3-1L	28% CW +ReX For 225 ºC/5min	88.4	270	255	1.09	22	23	11	0.22	800
H	Tmt2-B1-1L	12% CW +ReX for 275 ºC/5min	81.2	242	203.6	1.22	20.16	19.8	12.77	0.29	831.7
I	Tmt2-B2-1L	19% CW +ReX For 275 ºC/5min	83.52	253	204.2	1.22	21.49	19.58	14.85	0.24	851
J	Tmt2-B3-1L	28% CW+ReX for 275 ºC/5min	84	266	203.9	1.31	19.2	20.13	12.83	0.3	1318
K	Tmt3-C1-1L	12% CW +ReX For 325 ºC/5min	78.74	238	220.8	1.08	25.9	19.5	12.55	0.20	660.5
L	Tmt3-S2-CL	19% CW +ReX For 325 ºC/5min	80.7	250	230	1.09	22.7	19.7	14.05	0.22	758
M	Tmt3 -C3-1L	28% CW +ReX For 325 ºC/5min	83.32	263	255	1.04	21.8	19.7	12.3	0.17	630

Cw:- cold working ;Rex :- Recrystallization

Table 4.1: Tensile and ductility parameters of the 7075-O tempered alloy in the cold rolled and subsequent annealed condition.
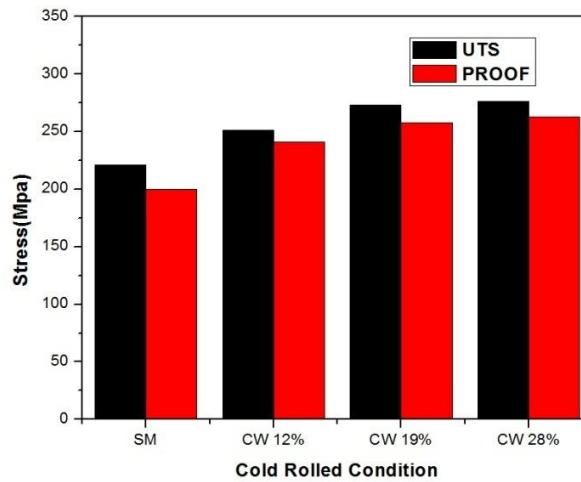
(a)
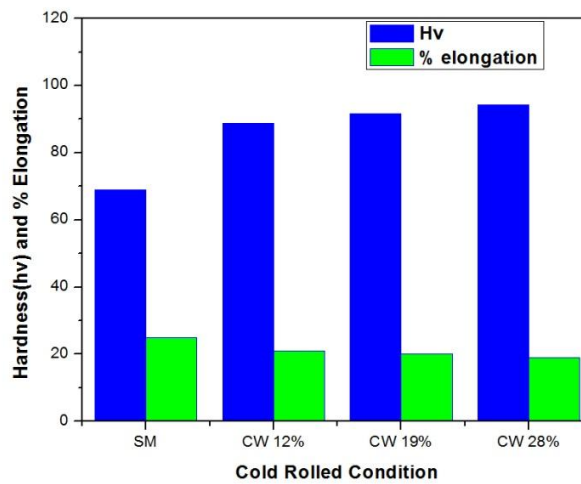
(b)

Figure 4.4:   Influence of cold rolling on the (a) Hardness, tensile strength, proof stress and (b) elongation of the cold worked 7075 –O Al alloy
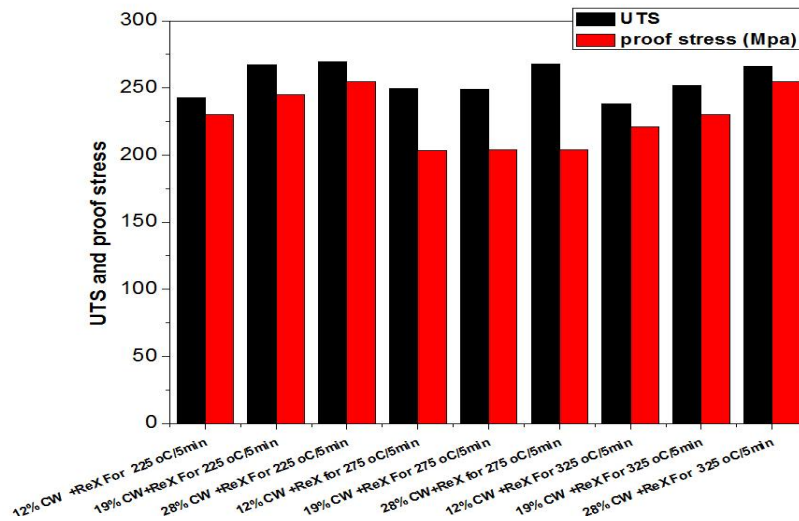
Figure 4.5: Variation of the proof stress, UTS and hardness of cold rolled and subsequent annealed sample
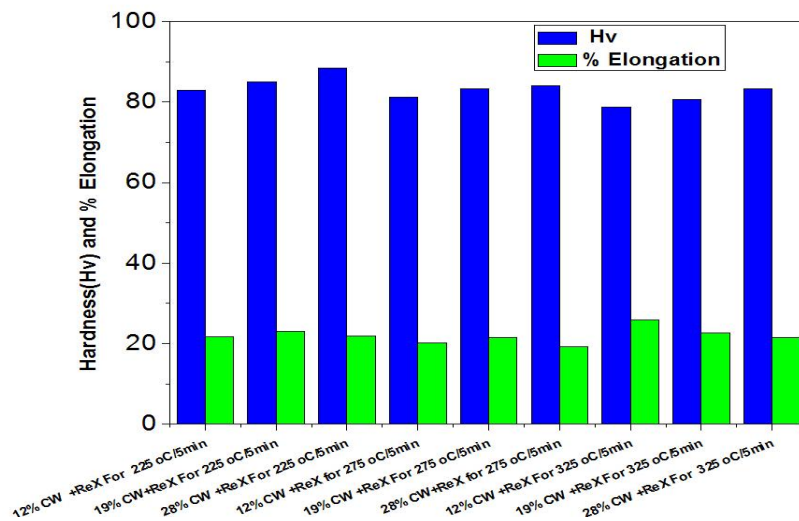

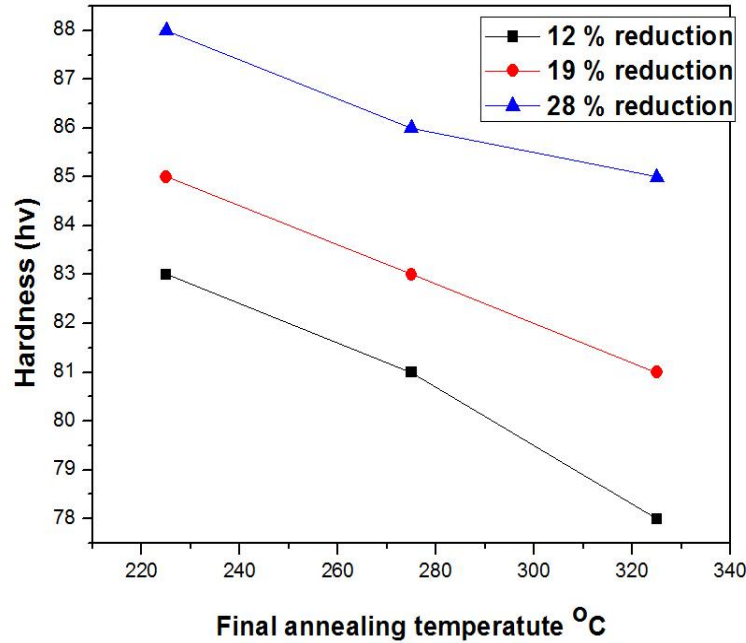Figure 4.6: Effect of cold rolling on the total elongation and hardness

Figure 4.7: Micro hardness in correlation with the various annealing temperatures

Figure 4.9 shows the SEM fracture surface of the tensile samples, which are 12% and 28% cold, rolled respectively without any final annealing. The SEM micrograph of cold worked samples indicates extended voids with fibrous structure (fine network of dimples) and a few quasi cleavage regions corresponding to the ductile to brittle fracture mechanism. Further, the voids shape and sized were depend of the degree of cold working. As compared to the 12% cold work, the finest voids are observed in the 28% deformed sample. In cold rolled and subsequent annealed samples of 12 % and 28 % reductions the SEM micrographs indicates both large dimples and fibrous features. The size of the dimple depends on the degree of cold rolling and annealing temperatures. The fracture surface of cold rolled and subsequent samples indicates the typical micro-void coalescence (MVC) mechanism of ductile failure.
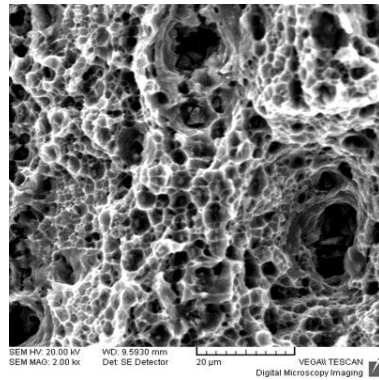
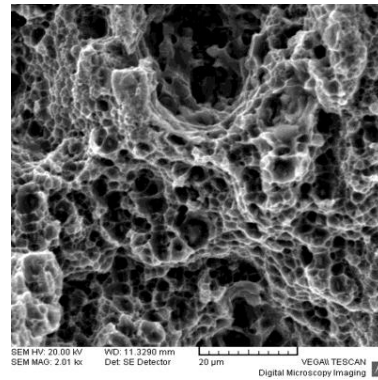(a)

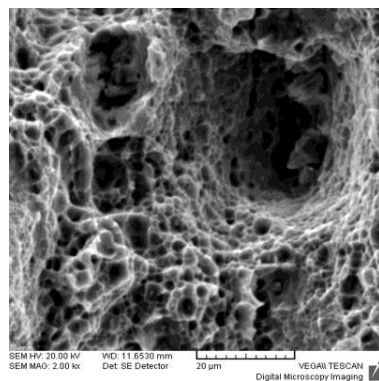

(b)

(c)
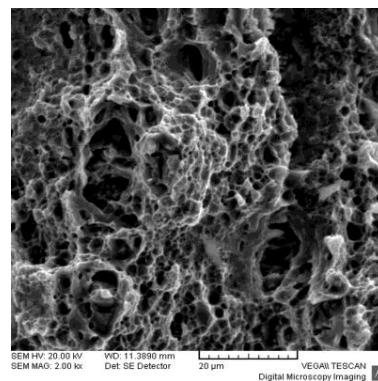

(d)

(e)

(f)

(g)   (h)
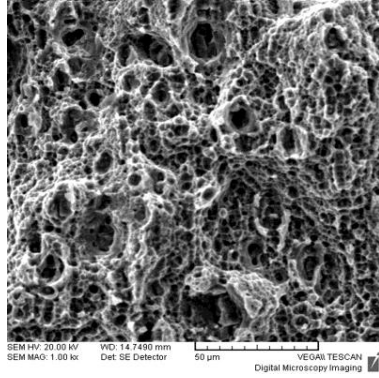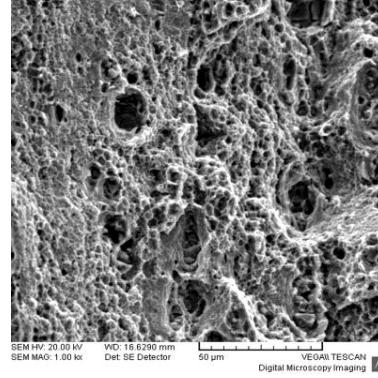
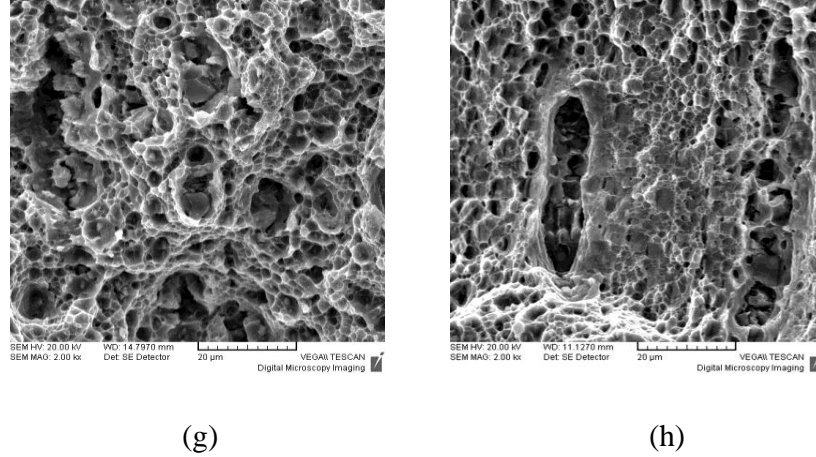Figure 4.8: SEM images of fractured tensile samples at 2000 X (20 µm), (a)7075 O tempered and 12 % cold rolled, (b) 7075 O tempered and 28 % cold rolled, (c) 12% CW+225°C Rex (d) 12% CW+275°C Rex, (e) 12% CW+325°C Rex, (f) 28% CW+225°C Rex, (g) 28% CW+275°C Rex, (h) 28% CW+325°C Rex

4.4 Corrosion test

From the literature study, the corrosion properties in 7075 Al alloys depend on the precipitates formed in and around the grain boundaries. Further the sequence of precipitates formation dependent on the dislocation generation during cold deformation and subsequent annealing. As the behavior of UTS attributed to the dislocations generated in the sample during thermo-mechanical treatments. In the present work, the corrosion properties were evaluated for the samples which has resulted in high and low UTS in the tensile test of thermo-mechanical treated samples.

4.4.1 Stress corrosion cracking test

The high and low values of the UTS are taken as references to evaluate the corrosion properties. The high and low UTS values for a particular set of cold deformation were drawn from table 4.1 and are presented in table 4.2 further the   SCC was evaluated though SSRT index which is defined as the ratio of elongation in air to the elongation in corrosion media. The stress – strain

diagram for thermo-mechanical treated sample were shown in figure 4.9 and the elongations observed both in NaCl and air were tabulated in table 4.2.
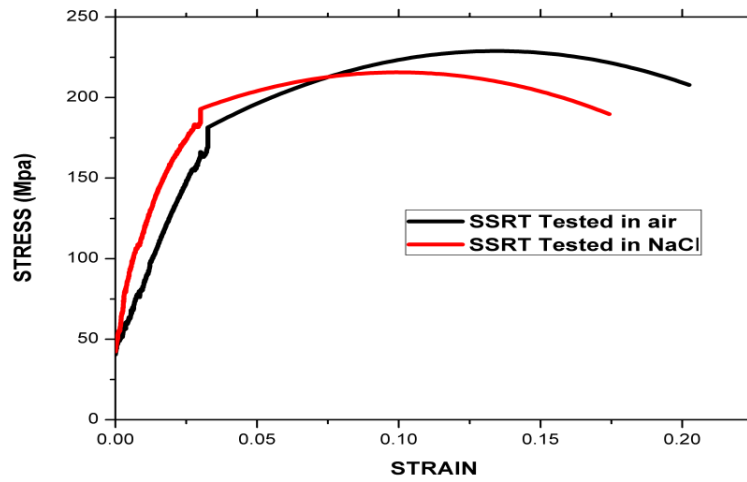
(a)
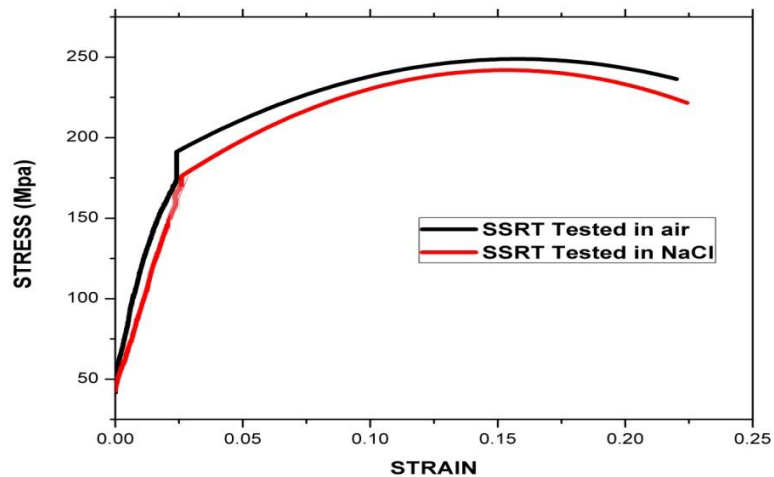
(b)

Figure 4.9: Shows the SSRT results of the samples (a) 12% CW +ReX For 225 $^{\circ}$C/5min (b) 28% CW +ReX For 325 $^{\circ}$C/5min.

Nomenclature	Treatment	Tension test UTS (Mpa)	UTS in SSRT in air (Mpa)	UTS in SSRT In NaCl (Mpa)	% Elongation in air	% Elongation in NaCl	SSRT index $E_{SOL/AIR}$	Corrosion rate (mm/year)
E	12% CW +ReX For 225 ^{o}C/5min	248	231.31	218.88	20	17	0.85	9.78
G	28% CW +ReX For 225 ^{o}C/5min	270	252.5	249.26	24.9	21	0.85	9.88
H	12% CW +ReX for 275 ^{o}C/5min	248	248.92	244.5	20.8	22	1	8.07
J	28% CW+ReX for 275 ^{o}C/5min	266	259	255	20.66	22.2	1	8.30
K	12% CW +ReX For 325 ^{o}C/5min	238	241.8	232.3	21	22.81	1	8.58
M	28% CW +ReX For 325 ^{o}C/5min	263	252.95	245.76	22	22.42	1	2.65

Cw:- cold working ;Rex :- Recrystallization

Table 4.2: Tensile and Corrosion properties cold rolled and annealed samples

From the SSRT index it was observed that the sample with low annealing temperature of 225°C experienced the corrosion attack ($E_{sol/air}$ = 0.8). The SCC attack in this sample was attributed due to low final annealing treatment of 225 ^{o}C for short duration of about 5 min is insufficient to provide heterogeneous nucleation of coarser precipitates at the dislocation networks. Even though for the sample experienced 28% cold reduction, which is expected to generate high dislocation networks has also experienced SCC attack due to low final annealing treatment. While the samples undergone high final annealing treatments of about 325°C the SCC

resistance has shown to improved as these thermo-mechanically treated samples has tendency to form higher dislocation densities along with inter spaced grain boundary precipitates. The improvement in the inter-particle spacing and size of the GBP's due to thermo-mechanical treatments could decline the anodic dissolution speed, and served the trapping sites for atomic hydrogen and produce molecular hydrogen bubbles, which would diminish the concentration of the atomic hydrogen on the grain boundaries.

In addition, it was observed that the samples experienced a specific heat treatment (such as samples H-L) and prolonged immersion in alkaline solution resulted formation thick films of corrosion products. The SSRT was carried out with a very slow strain rate of 4 X 10 $^{-5}$ s^{-1} and was conducted in 3.5 % NaCl solution with pH of 12 (alkaline solution) and the test was performed for more than 50 hrs. Generally, the corrosion product consist of mixture of hydroxides. It is believed that the Aluminum hydroxide might be the main compound to combine with the minor elements such as zinc, magnesium and copper hydroxides. The presence of copper ions in the hydroxide may result in destruction of H-bond and diminish the attraction of chloride ions from the corrosive medium. As a result, the corrosion product consisting of copper-enriched hydroxide is more protective and the aluminum alloy beneath suffer less attack by chloride ions.

Form the SEM-EDS corrosion products were formed on the SSRT sample surface (tested in NaCl) as shown in figure 4.10 and wt % of the elements present are tabulated in table 4.3. The XRD analysis for the corroded sample is shown in figure 4.11(a). The major phases present on the SSRT sample were observed to be Al, $MgZn_2$, Cu_2O and MgO . The XRD analysis carried out at slow scan rate (0.005 s^{-1}) in the 2Θ range of 30° to 50 ^{o} to characterize the presence of MgO on the surface shown in figure 4.11(b). These Cu_2O and MgO along with other corrosion products on the surface of the sample act as a effective barrier to avoid further interaction of bulk material with the corrosion media and thereby enhancing its corrosion resistance.

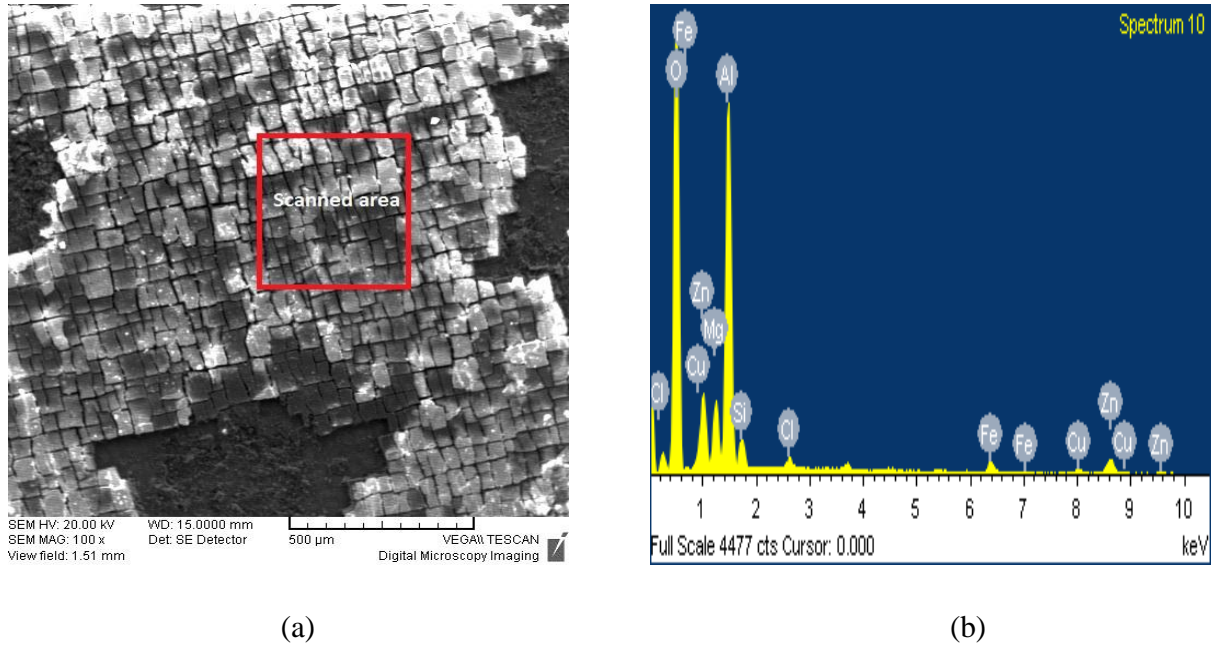(a)   (b)

Figure 4.10: (a) SEM- EDS analysis of the corrosion products on the surface of 28% CW +ReX For 325 ^{o}C/5min in NaCl solution (b) EDS spectra obtain from scanned area.

Sl.no	Element	Weight%
1	O K	58.72
2	Mg K	4.84
3	Al K	22.26
4	Si K	2.11
5	Cl K	0.70
6	Fe K	2.15
7	Cu K	1.63
8	Zn K	7.60
Total		100

Table 4.3: SEM- EDS results analyzed area shown in figure 4.12.
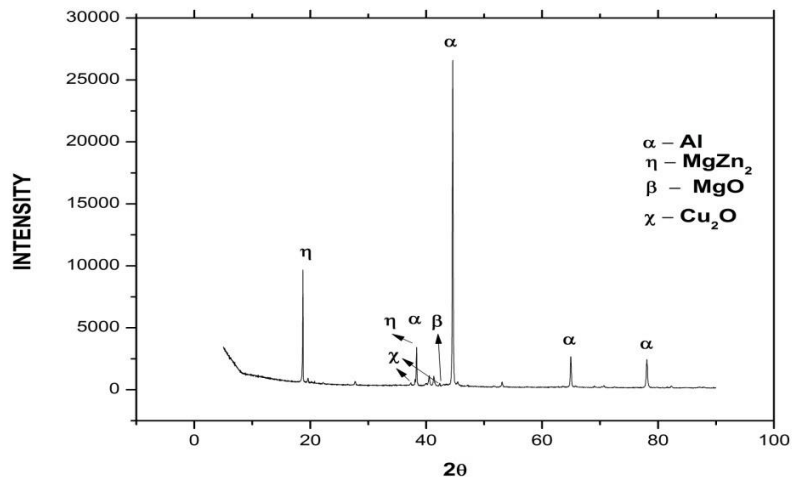
(a)
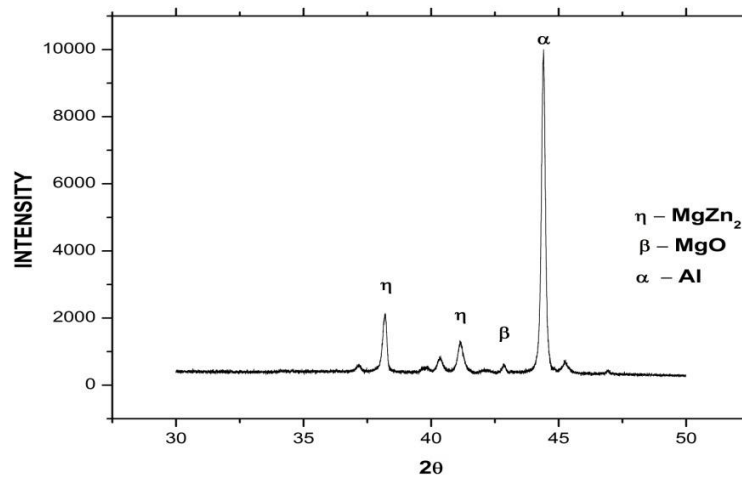
(b)

Figure 4.11: (a) XRD analysis of the sample 28% CW +ReX For 325 ^{o}C/5min in NaCl after SSRT test. (b) XRD analysis of the same sample

Figure 4.12 show the Potentiodynamic polarization plots for thermo-mechanical treated samples. The polarizations tests were performed to understand the corrosion behavior of the particular thermo-mechanical treated condition while performing the test without immersing for prolonged period in NaCl solution, indicated as corrosion rate in table 4.2. It was observed that the sample with high cold reduction and with high final annealing temperature resulted in high corrosion resistance.
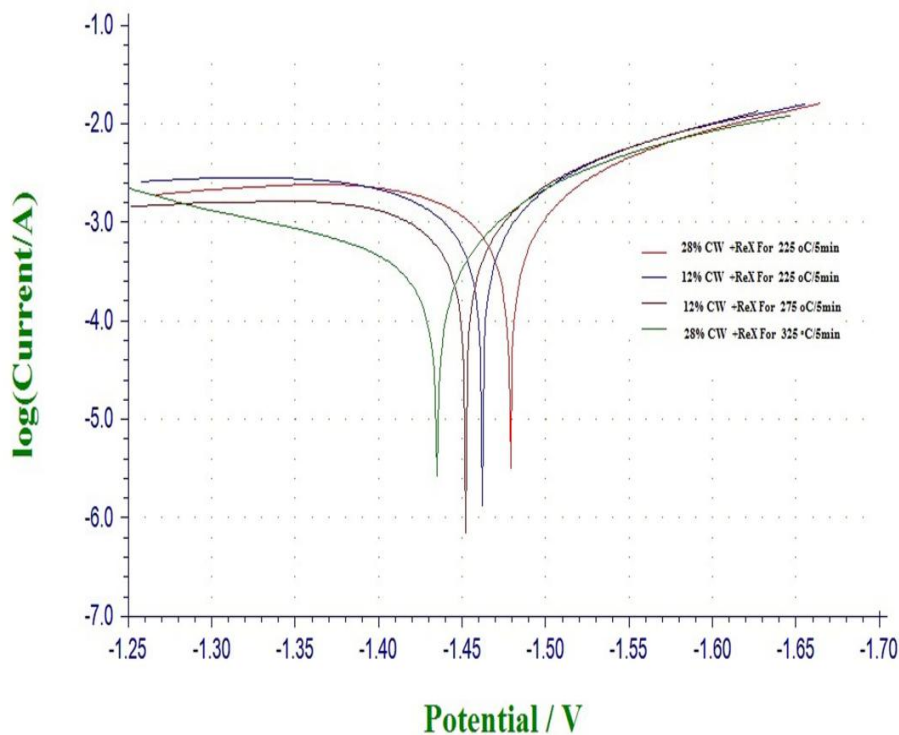
Figure 4.12: Potentiodynamic polarization plots of the thermo-mechanically treated samples.

Figure 4.13 presents the typical SSRT fracture surfaces of the thermo mechanically treated samples tested in air and in 3.5% NaCl solution. The fracture surface of the cold rolled and at low annealed samples tested in air dominated by fine dimples with micro-voids, as shown in figure 4.13(a). Whereas the same sample when in tested in NaCl solution resulted in intergranular cracking with corrosion attack which typically resembling a brittle fracture feature as shown in figure 4.13(b). Several corrosion products were also observed on the fracture surfaces which were shown in figure 4.14 and were analyzed by SEM-EDS shown in table 4.4.

Whereas the fracture surface of the sample treated with higher annealing temperature and SSRT conducted in air was dominated by large size dimple with micro-void coalescence. Similar type of features were observed in high temperature annealed samples tested in NaCl solution which corroborates that corrosion attack has not been taken place which are illustrated in figure 4.14 (c) and (d).
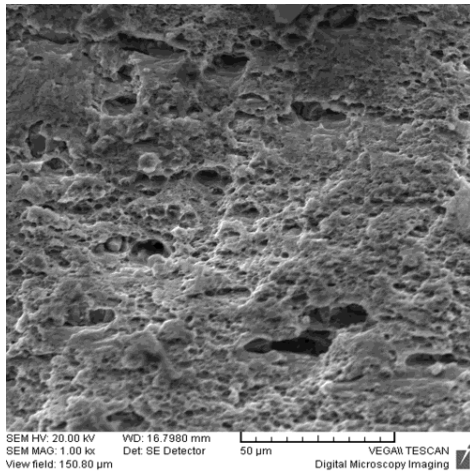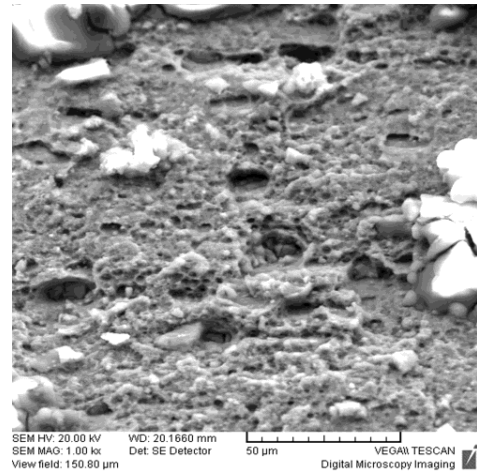
(a) (b)
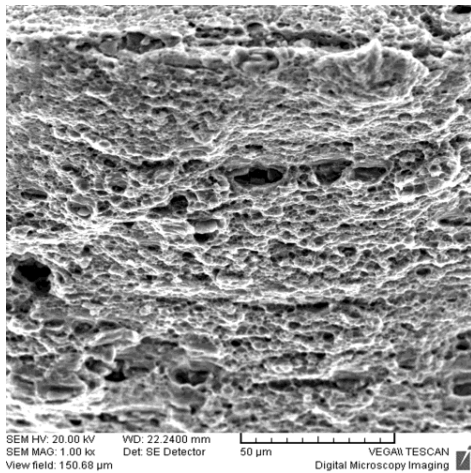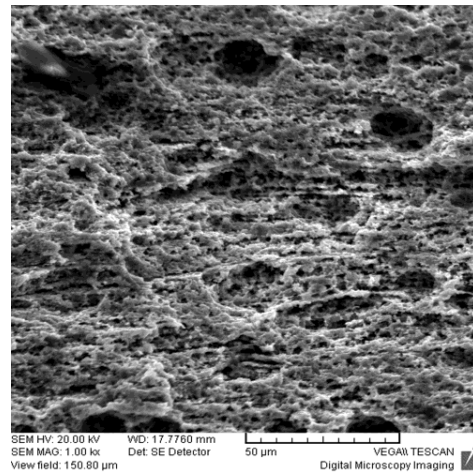
(c) (d)

Figure 4.13: SEM micrographs showing SSRT fracture surfaces of 7075 samples with various treatments (a) 12% CW +ReX For 225 ^{o}C/5min in air (b) 12% CW +ReX For 225 ^{o}C/5min in NaCl (c) 28% CW +ReX For 325 ^{o}C/5min in Air (d) 28% CW +ReX For 325 ^{o}C/5min in NaCl.

| (a) | (b) |
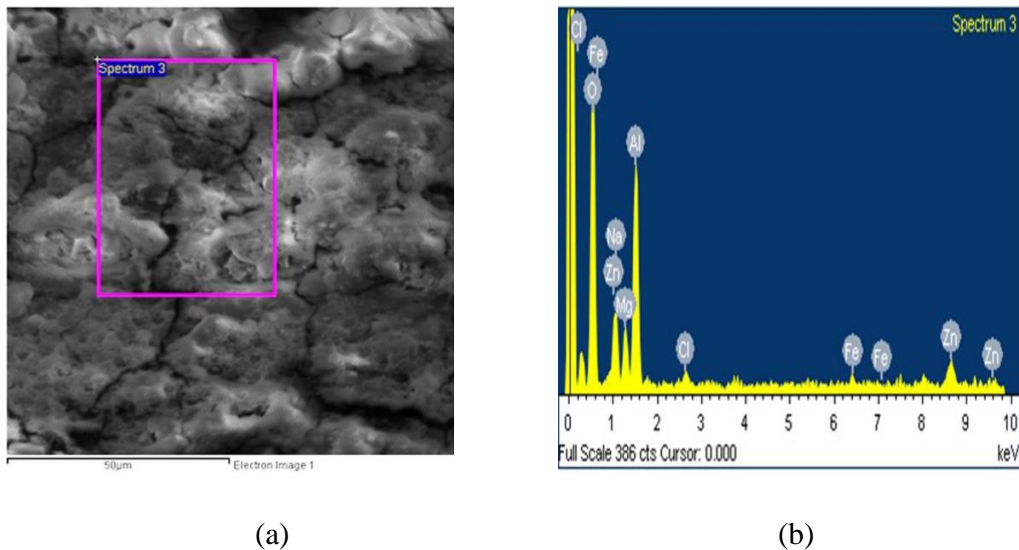
Figure 4.14: (a) SEM- EDS analysis of the corrosion products on the fracture surface of 12% CW +ReX For 225 ^{o}C/5min in NaCl solution (b) EDS spectra obtain from scanned area.

Sl no.	Element	Weight%
1	O K	52.31
2	Na K	4.78
3	Mg K	5.54
4	Al K	19.85
5	Cl K	0.99
6	Fe K	2.17

Table 4.4: SEM- EDS results analyzed area shown in figure 4.14

4.5 Chapter summary

In this work slow strain rate tests and potentiodynamic polarization tests were carried out to evaluate the corrosion properties. It was observed that the sample with high cold reduction and annealed at high temperatures has given the best corrosion resistance both in SSRT and potentiodynamic polarization. The enhancement of corrosion properties attributed due to formation of corrosion products over the surface of the sample during test due to prolonged immersion in alkaline media. This formed corrosion products act as film on the surface which has tendency to restrict further corrosion attack. The samples with low cold reduction and low final annealing treatments such as sample, 12% cold deformation and final annealed at 225°C was susceptible to corrosion attack. Where the sample M (28% red + rex 325 ^{O}C) considered as specific thermo-mechanical treatment which has resulted in superior corrosion properties both in SSRT and in potentiodynamic polarization test.

CHAPTER 5

(b) Results and Discussion on Influence of Diode Laser Surface Melting on Microstructure and Corrosion Resistance of 7075 Aluminum alloy

5.1 Introduction

The presence of different second phase intermetallic particles in AA 7xxx alloys affects their corrosion properties. The reduction or elimination of such intermetallic particles from the surface of the alloy may increase the corrosion resistance. This chapter deals with the application of high power diode Lasers (HPDL) to alter the surface microstructure and its effect on the corrosion properties.

5.2 Microstructure Analysis

Figure 5.1 shows the morphology of the laser treated surface. It has been observed that surface treatment carried out with a high power laser density that is with 200 J/mm^2 (1000 J/mm) resulted in heavily undulated surface. Under the influence of very high temperature during the laser treatment, the surface material evaporates, thereby forming a specific surface area with undulation. Whereas the laser treatment carried out with energy densities of 80 J/mm^2(400 J/mm) 120 J/mm^2 (600 J/mm) and 150 J/mm^2 (750 J/mm) resulted in the uniform surface finishing which has been depicted in figure 5.1.

In addition, the sample treated with laser energy density of 100 J/mm^2(800 J/mm) resulted in solidification crack long the laser track. During laser processing large thermal gradients are generated between the melted region and the substrate. This large thermal gradient produces thermal stresses. Excessive thermal stress resulting from laser processing leads to surface and subsurface cracking. Once the laser beam is no longer heating a spot on the surface of a material a period of rapid cooling takes place, which is typical with laser processing. This causes stretching in the heated surface and as the limit of this stretching is reached, cracks develop as the tension is relieved. Upon cooling, the whole of a laser-treated track is in tension. More specifically, the laser track experiences tensile hydrostatic pressure stresses. These tensile hydrostatic pressure stresses can be readily attributed to the fact that the treated track shrinks more than the surrounding substrate during cooling resulting surface and subsurface cracks.
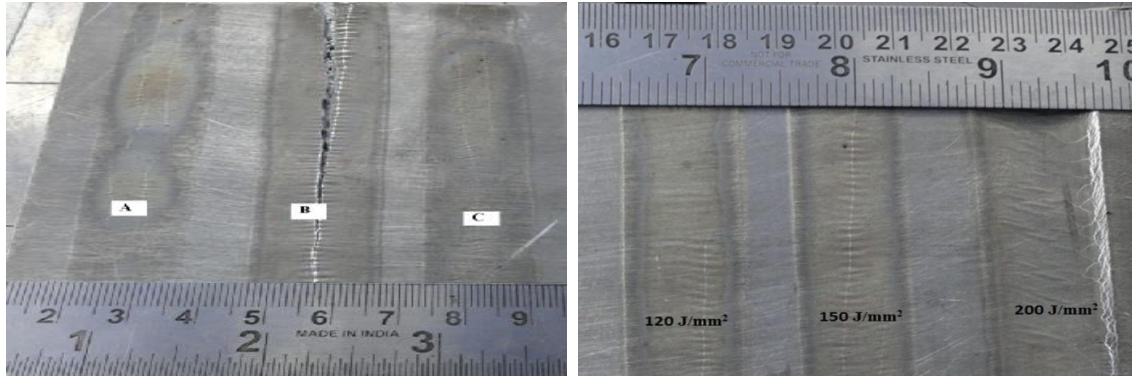
Figure 5.1: Illustrating the laser surface melting tracks with various energy densities

Figure 5.2 depict cross-sectional macrographs of laser melted layers processed under mentioned energy density and Table 5.1 shows measured depth of melted zone, Interface zone and Heat affected zone (HAZ) obtained in each case evaluated form image analysis software attached to microscope. The surface microhardness measurements were also carried out on the treated surfaces and reported in the table as ready reference. The preferential chemical attack due to etching evidently indicated distinguishably different zones (marked in Figure 5.2) in the treated layer associated with thermal diffusion effects.

(a)

(b)

(c)
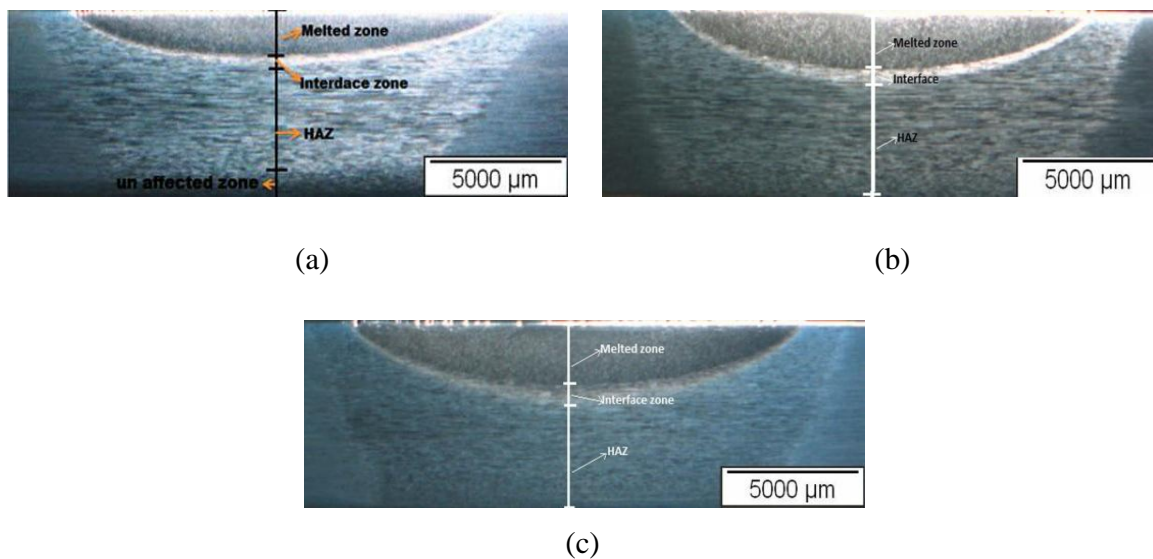
Figure 5.2: Cross sectional stereographic microstructure of the samples at 12x of laser melted layer illustrating various zones.(a)80 J/mm^2 (b)120 J/mm^2 (c)150 J/mm^2

Also, crack-free smooth and flat surface was observed in the melted layer. The melt depth in the treated layer was observed to in between 1.5 mm to 2.5 mm and the width of the melt observed to be 16.7 - 18mm. These melt depths and widths are depend on the heat inputs and transverse speeds are illustrated in table 5.1.

| Laser power (W)	Scan speed (mm/s)	Heat input (J/mm)	Laser Energy Density J/mm^2	Depth of melt (mm)	Depth of interface zone(μm)	Depth of HAZ(mm)	Width of melt (mm)	Surface Hardness (Hv)
4000	10	400	80	1.5	300	4.55	16.7	135-140
3000	5	600	120	1.8	400	4.15	17	137-140
3000	4	750	150	2.3	500	3.55	17.5	137-140
			Surface Hardness of untreated alloy 160-165Hv					

Table 5.1: Melt depths and Hardness value for laser treated samples

The observed width of the processed zone for the applied laser interest is less than the focused laser beam attributed to the laser intensity distribution. The interface layer depth (preferentially bright layer) obtained between the melted and heat affected zone was about 300 to 500 microns thick and a shallow heat affected zone of 4.2 mm to 3.55mm was observed in the treated sample.

In the present work it was observed that the melt depth has increased manifold (in millimeters) as compared to that reported in Nd:YAG laser treatment (about 300 microns) utilizing a smaller circular spot [37]. This could plausibly be attributed to the high energy coupling efficiency associated with diode laser wavelength. The distinguishably distinct bright interface region at melted boundary shows termination of coarse secondary phase particles observed in HAZ and unaffected parent material microstructures. Similar boundary layers were observed in studies involving laser melting utilizing YAG and Eximer lasers and attributed to

dissolution of coarse constituent phases in the melted layers [37, 38]. Indeed, insufficient thermal diffusion in HAZ regions associated with low temperatures (but sufficiently higher than that of conventional heat treatment cycles) may not facilitate in dissolution of constituent phases in grains and grain boundaries as evident from unperturbed wrought microstructure.

The microstructure across the depth of the laser-treated layer varied (as observed in case depth analysis) due to laser treatment thermal profile variation, corrosion attack is a near surface phenomena and as a result, near surface microstructure examination is vital for analysis. Figure 5.3 illustrate high magnification SEM surface microstructures obtained in laser treated layers processed with 80 J/mm^2 ,120 J/mm^2 and 150 J/mm^2 as well as untreated substrate. The corresponding phases obtained by XRD analysis are presented in Figure 5.4. The microstructure of untreated alloy depicted in Figure 5.3 (a) shows presence of uniformly distributed coarse primary particles as well as fine inter-metallic precipitation hardened particles along the Al-rich grain boundaries. It appears large intermetallic primary particles (5 – 20 μm sized) remained undissolved during solution treatment, whereas, fine submicron particles (0.5 - 2 μm sized) produced due to secondary hardening precipitation during the artificial ageing are formed along the grain boundary is discernible in the microstructure. Various studies also reported similar microstructure in the aluminum alloy when processed under peak aged condition[9]. The constituent secondary hardened particles present in the microstructure of untreated substrate were found to be running along the rolling direction. From XRD analysis (Figure 5.4) these constituent phases are identified as $MgZn_2$, Al_7Cu_2Fe, $CuAl_2$, Mg_2Si and along with few Si containing phases. The presence of such constituent phases was also reported in the work of Birbilis [118].

The SEM-EDAX spot analysis along with elemental mapping depicted in Figure 5.5 (a) and Figure 5.6 further corroborate the presence of these constituent phases in Al-rich grains and grain-boundaries of the untreated substrate. Indeed presence of coarse Zn-lean platelets (Al-Cu-Fe) in the Zn-rich Al-rich matrix grains of untreated substrate could be attributed to the over aging condition adopted [118].
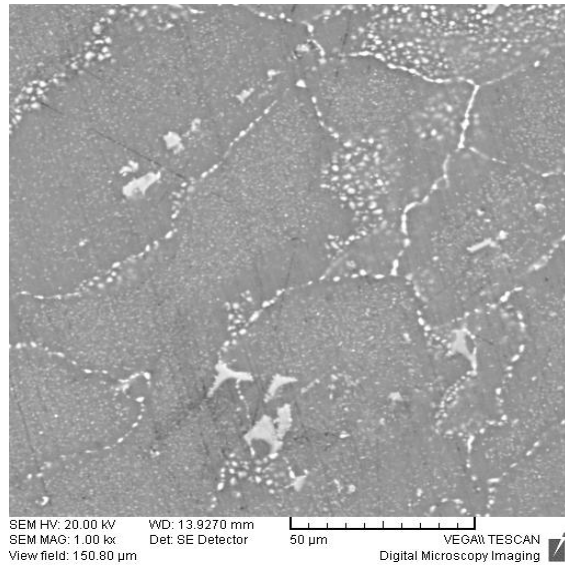
(a)
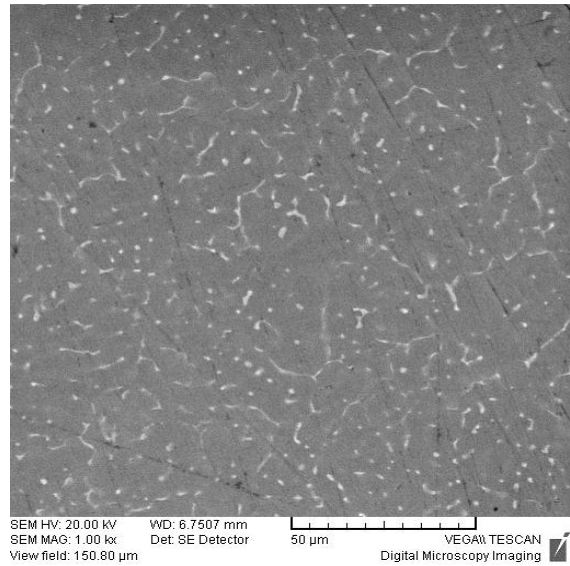
(b)
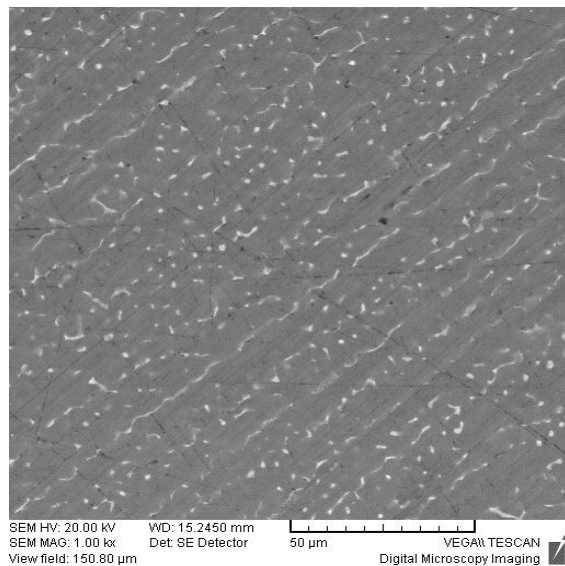
(c)
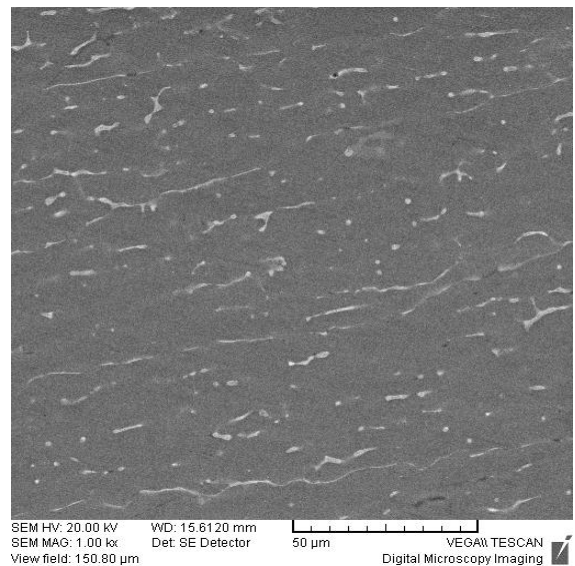
(d)

Figure 5.3: SEM Surface microstructures at high magnification of (a) As received 7075 Al alloy (b) Sample lased with 80J/mm^2 (c) Sample lased with 120J/mm^2 (d) Sample lased with 150J/mm^2
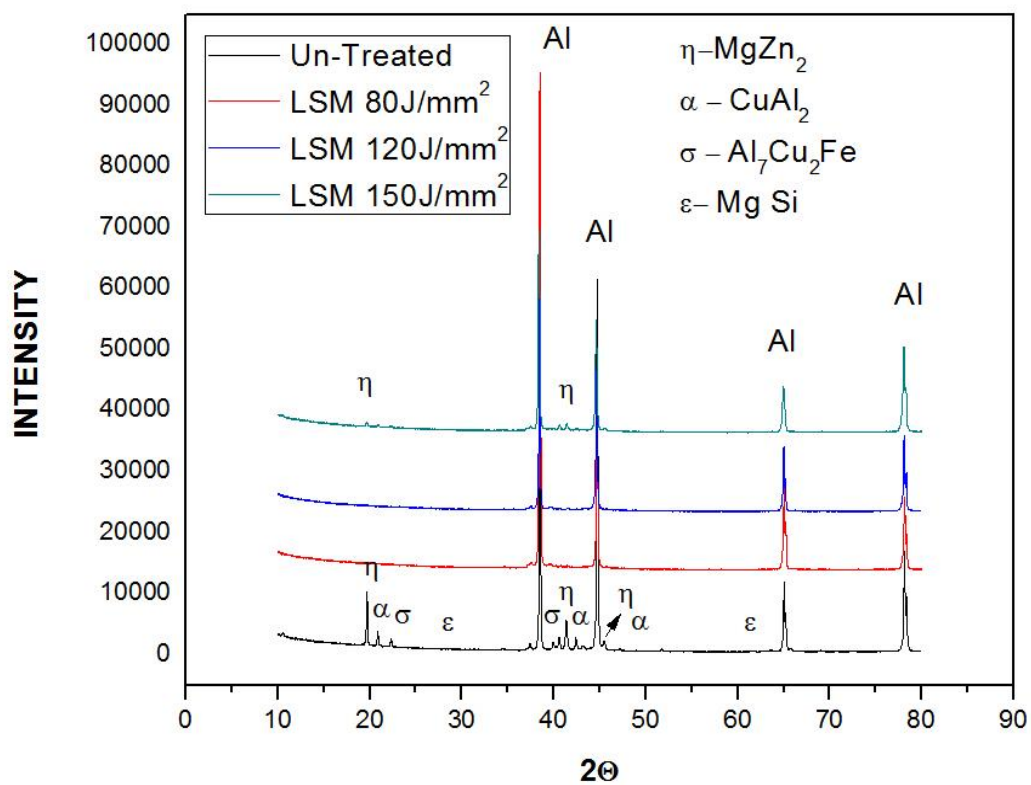
Figure 5.4: XRD of untreated and laser treated sample.

(a)

(b)

(c)

(d)
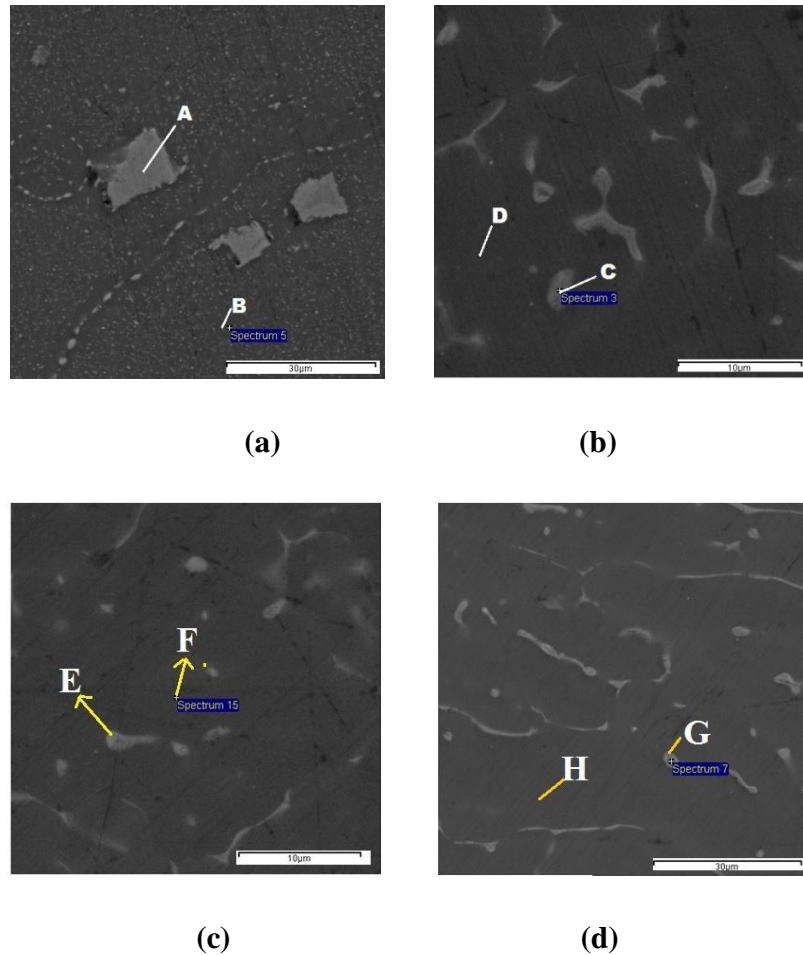
Figure 5.5: SEM images showing positions of EDS analysis (a) As received 7075 Al alloy (b) laser melted sample. The wt% of the composition depicted in table 5.2

SL.NO	ELEMENTS Wt%	AS RECEVIED		80 J/mm^2		120 J/mm^2		150 J/mm^2	
		Spot A	Spot B	Spot C	Spot D	Spot E	Spot F	Spot G	Spot H
1	Mg	0.26	2.90	6.07	1.78	6.16	1.47	8.30	1.67
2	Al	55.92	87.85	73.87	92.96	73.43	93.90	61.86	93.27
3	Fe	12.60	0.14	0.07	0.11	0.03	0.05	0.04	0.2
4	Cu	29.57	1.68	6.47	0.62	5.63	0.25	11.31	0.46
5	Zn	1.65	7.43	13.52	4.53	14.15	4.34	18.49	4.37

Table 5.2 : EDS spot spectrum analysis on the as- received and laser treated samples

(a)

(b)

(c)

(d)

(e)

(f)
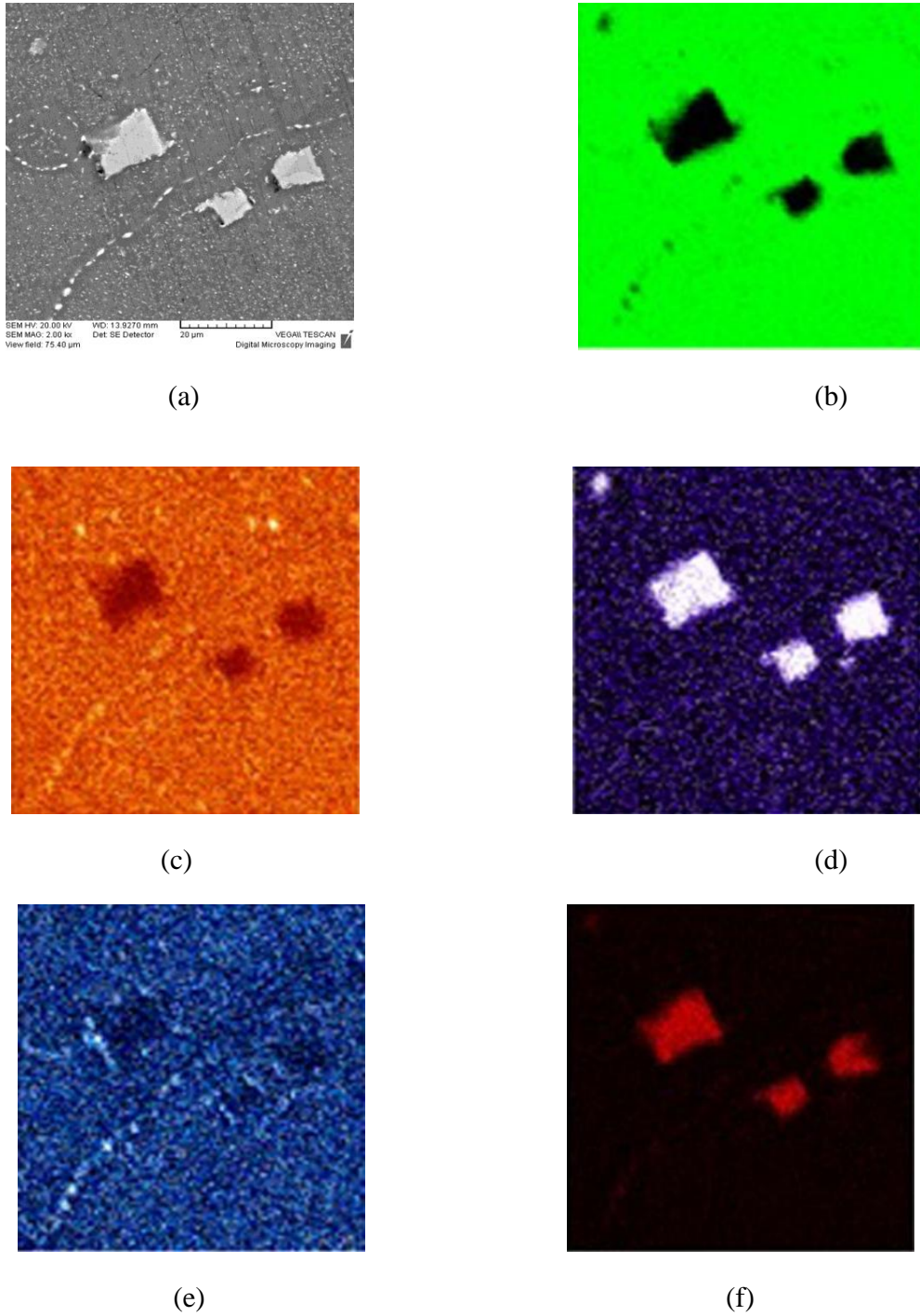
Figure 5.6: SEM-EDX mapping analysis of as- received AA 7075-T6 alloy. (a) Micrograph of the surface revealing the presence of dispersed phase (b) Al (c) Mg (d) Fe (e) Zn (f) Cu.
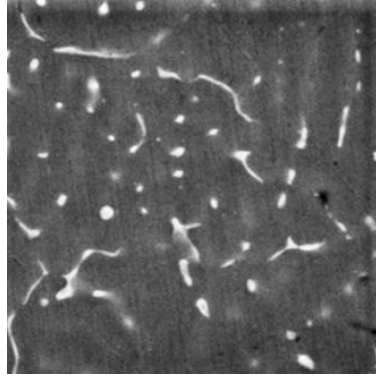
(a)
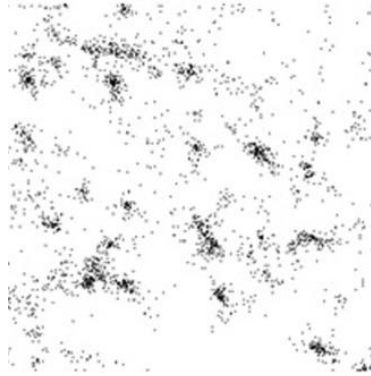
(b)
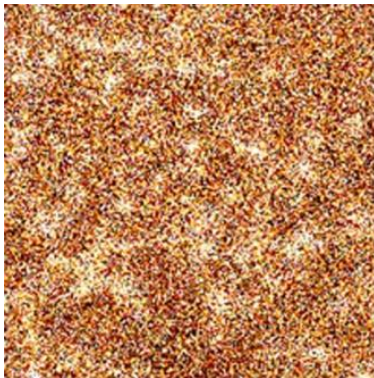
(c)
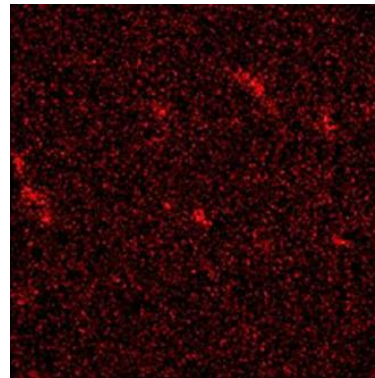
(d)
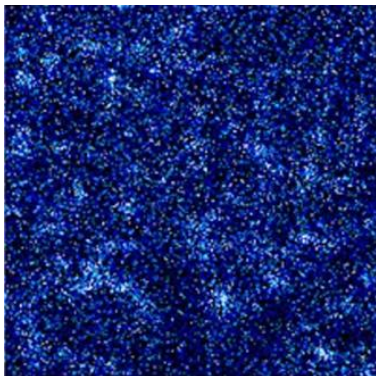
(e)
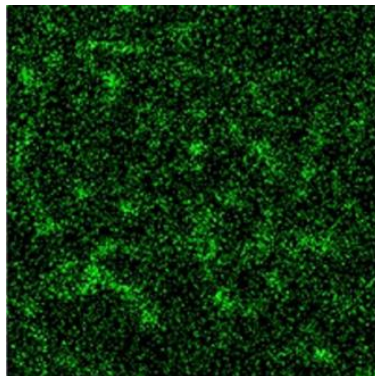
(f)

Figure 5.7: SEM-EDX mapping analysis of laser treated with 80J/mm^2 sample. (a) Micrograph of the surface revealing the presence of dispersed phase (b) Al (c) Mg (d) Fe (e) Zn (f) Cu.

(a)

(b)

(c)

(d)

(e)

(f)
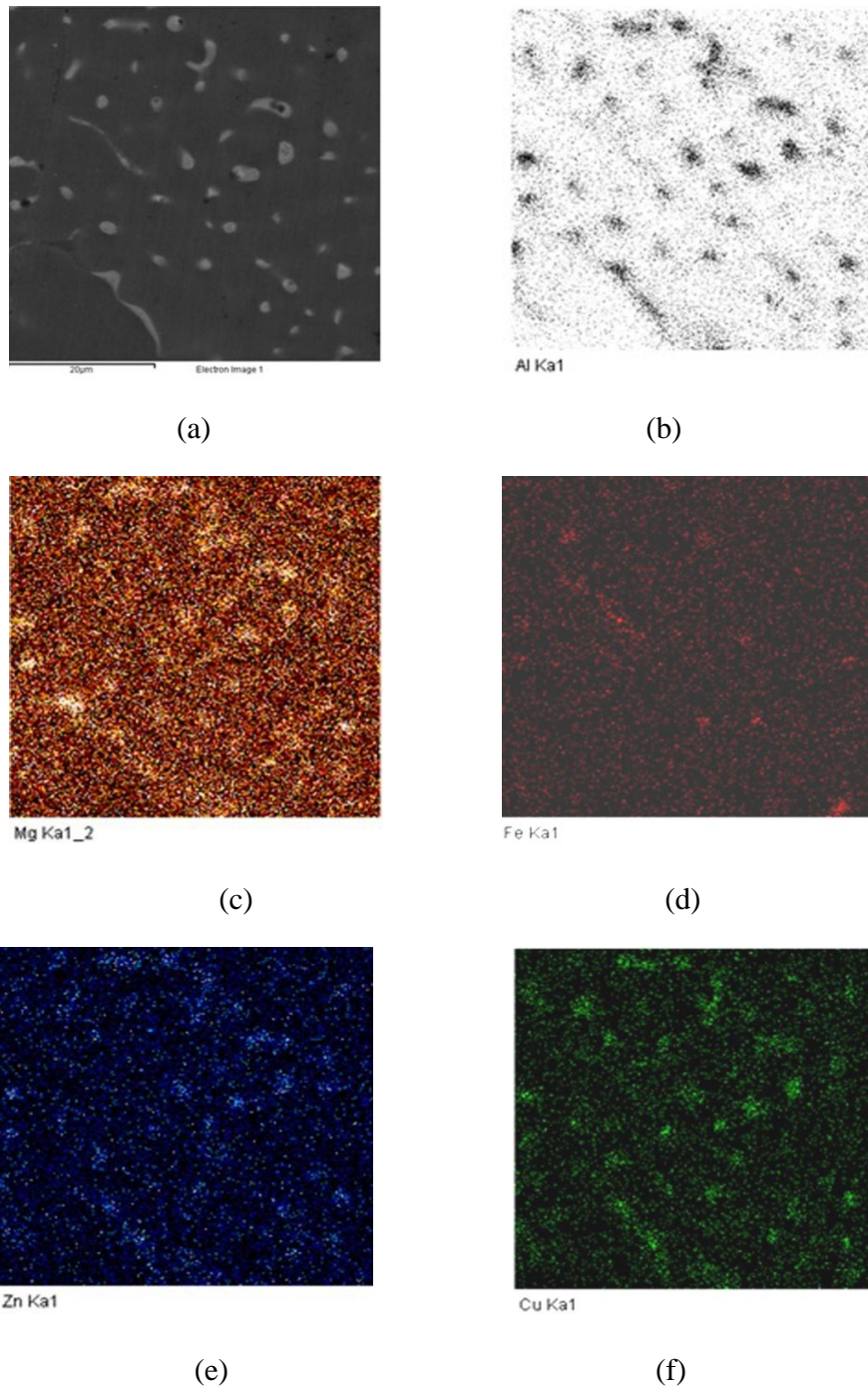
Figure 5.8: SEM-EDX mapping analysis of laser treated with 120 J/mm^2 sample. (a) Micrograph of the surface revealing the presence of dispersed phase (b) Al (c) Mg (d) Fe (e) Zn (f) Cu.

(a)   (b)

(c)   (d)

(e)   (f)
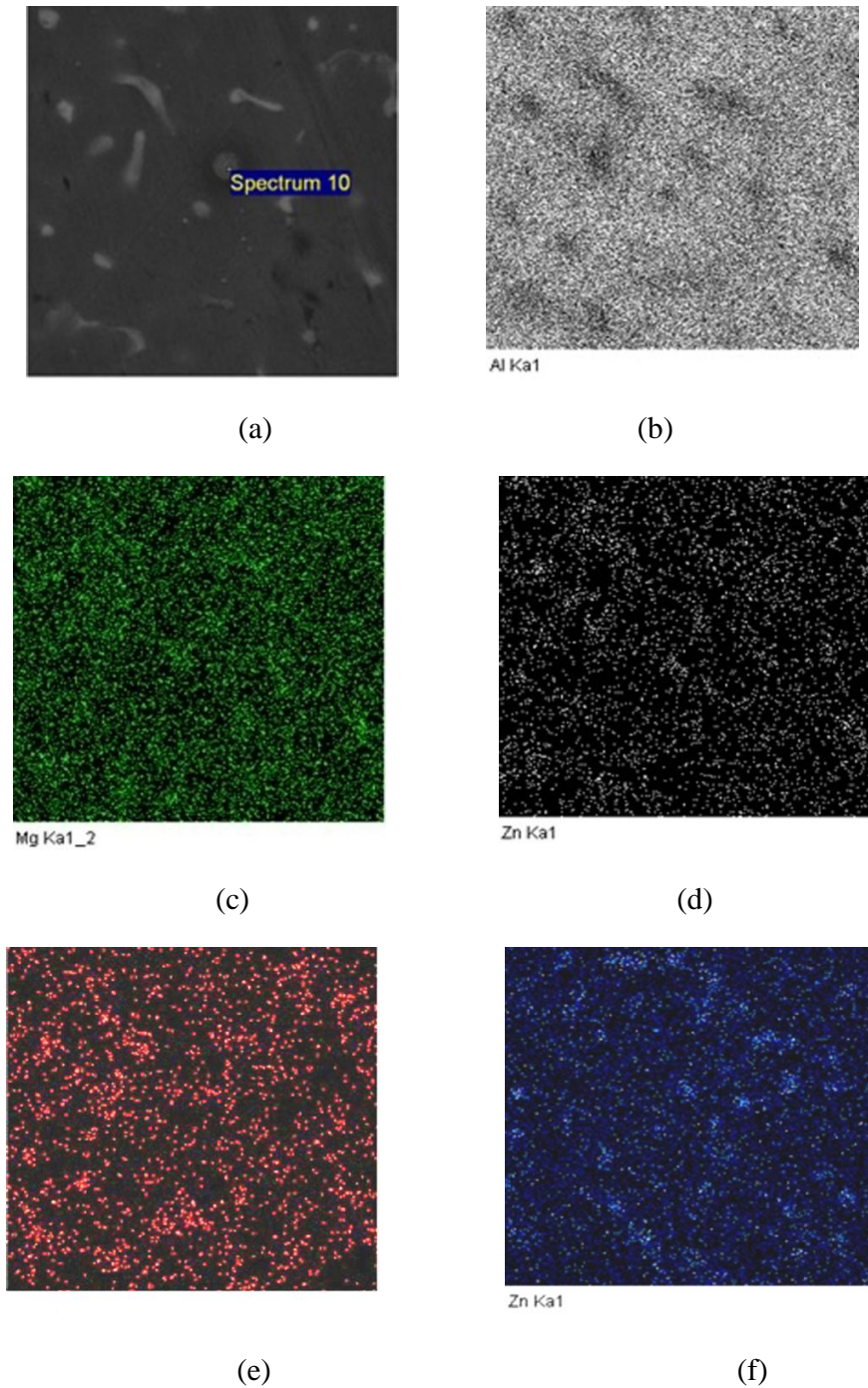
Figure 5.9: SEM-EDX mapping analysis of laser treated with 150J/mm^2 sample. (a) Micrograph of the surface revealing the presence of dispersed phase (b) Al (c) Mg (d) Fe (e) Zn (f) Cu.

In contrast to the substrate microstructure, laser melted surface microstructure observed to be fine dendritic/cellular on account of the rapid melting and re-solidification associated with the laser treatment cycle. It was reported that LSM treatment provides an amalgamation of the second phase particles and aluminium matrix in solid solution of the melted layer. The solid solution should then solidify rapidly to prevent interface instability, entrapping the solute in solid-solution. The microstructure as depicted in Figure 5.5 (b-d) consist of fine discontinuous network of dispersed phases of about 2-3μm sized comprising of Al-Cu-Mg-Zn which are examined through SEM-EDAX spot spectrum analysis illustrated in Figure 5.5 (b-d) and also from the table 5.2 which shows the quantitative weight percentage of composition. The presence of above mention phase was also evident from the SEM-EDAX area mapping depicted in Figure 5.7- 5.9. It shows the presence of very fine phase bearing Al-Cu-Mg-Zn spreading throughout the melted surface uniformly unlike the coarse phases present in the untreated sample.

The samples treated with laser energy density of 80 J/mm^2 and 120 J/mm^2 observed that the weight percentage of Cu was appreciable decreased about 5-6 times when compared with the composition of phases present on the untreated and laser treated samples. Further, it was observed that the sample treated with 150 J/mm^2 the weight percentage of copper has been increased as compared with the other treated samples. Similar observation were made by Rayn et al., [119, 120] . Iron was absent as in the laser melted layer, can be depicted from the EDAX analysis and also from the elemental mapping. It also worth mention that the composition of the matrix of untreated and laser treated were remain almost same.

The results of low angle X-ray diffraction of the after LSM were illustrated in figure 5.4. As mentioned earlier that as-received alloys contains large number of second phase particles such as $MgZn_2$, $AlCuMg_4$, AlCuFe, $CuAl_2$ and Mg_2Si, which are responsible for initiation of galvanic effect when interacted with matrix in corrosive medium. After the laser treatment, no significantly high peaks from large second phases were observed which substantiates absence of phases as were present in the untreated sample. There absence might be due to this particle re-dissolve in to solution during the laser melting and stayed in solution during solidification. Except $MgZn_2$ phase has been observed after LSM.

From the above discussions, observed that the high cooling rate of lasers, with the existence of varying alloying elements that have different physical properties in the solid solution of the melted layer, influence the solidification microstructure by formation of small-dispersed phases, which are enriched or depletion of alloying elements.

Overall, laser melting resulted in complete Fe and partially eliminating Cu primary constituent particles present in wrought structure with vast refinement in microstructures. It is well known that these Cu and Fe rich phases can presumably act cathodic to the matrix and thereby tend to promote surrounding matrix dissolution leading to severe galvanic corrosion effect [118]. Indeed, various studies also reported the possibility of enhancing corrosion resistance by elimination of large constituent particles that generally induce surface defects to initiate SCC.

5.3 Hardness Distribution

Figure 5.10 illustrate cross-sectional micro-hardness distribution across the depth of the laser melted layer with identification of various zones of interest as depicted in Figure 5.2. It is clear that hardness reduced to 121 – 132 HV in the melted region as against the unaffected substrate hardness of 160 – 165 HV. The reduction in hardness in between 1.5-2 mm deep melted region could be attributed to the elimination of hard primary precipitates previously present in wrought microstructure. With further increase in depth, hardness reduced to the range of 115-120 HV representing the interface zone of the treated layer. Indeed further reduction of hardness in the interface zone could be due to absence of not only primary precipitates but also secondary hardening precipitates as evident from the mushy microstructure with planar growth. Further with increase in case depth (near Heat Affected zone), gradual increase in hardness could be observed. As laser treatment cycle induces temperature gradients with variation in cooling rate along its depth, different zones experience different thermal conditions and as a result of microstructure variation is anticipated. As the cooling rate will be highest at the featureless mushy interface zone, it may be plausible that temperature experienced could be sufficiently low to suppress precipitation and there by retaining virgin hardness of Al-rich matrix grains. Thus, variation in hardness across the depth of laser treated layer is found to be convergent with

microstrucural changes experienced by the laser treatment thermal cycle. Similar reduction in hardness due to melting and heat affected zones was observed in the laser treated layers processed with different lasers and different conditions[121]. Overall, hardness of the affected microstructure either due to melting or due to heating is found to be governed by the amount of hardening precipitates present in the microstructure.
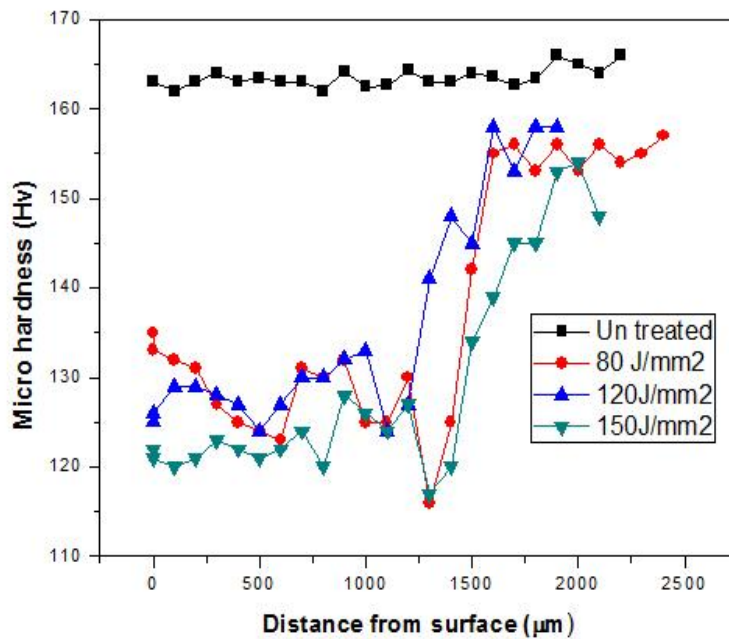
Figure 5.10: Hardness distribution across the depth of LSM samples

5.4 Corrosion Behavior

5.4.1 Potentiodynamic Polarization Test

Figure 5.11 and table 5.3 shows the potentiodynamic polarization plots and corrosion test data respectively for the laser-treated and untreated 7075-T6 alloy tested in 3.5% NaCl solution. Result evidently indicates substantial reduction in corrosion rate of laser melted surface as compared to untreated one. The pitting potential in case of untreated specimen was found to be closer to the corrosion potential indicating virtually immediate commencement of anodic polarization with no build up of any passive film. It was observed that the sample treated with laser energy density of 80 and 120 J/mm^2 resulted in vast decrease in corrosion current of about 9.54 X10^{-7} μA and 3.06 X10^{-7} μA respectively as compared with the un treated sample current which is reported to be 3.4X10^{-6} μA. The decrease in corrosion currents in laser treated surface was attributed due to decrease in constituent elements such as copper and iron and their phases formed with the combinations other elements in the alloys. Whereas, the sample treated with energy density of 150 J/mm^2 has resulted in increase in corrosion currents as compared to samples treated with 80 and 120 J/mm^2. The increase in the corrosion current in this case may attributes to the presence of copper in the dispersed phase in the treated layer, which was evident from the SEM EDAX studies as shown in table 5.2.

Furthermore, laser melted surfaces, significant passive film formation could be observed. It is well known that presence of constituent particles such as Al-Cu-Fe and AlCu$_2$ etc. can easily promote galvanic effects across their boundaries and thereby nucleate corrosion pits formation. As laser melting substantially reduced these constituent particulates, promotion of corrosion attack at the particle-to-grain boundary leading to pit formation were substantially reduced. More details are giving on the physical properties of the intermetallic particles at 7xxx alloys in Appendix 1(a). Similar studies conducted with different laser treated conditions also reported vast reduction in corrosion currents of melted layers produced with precipitate-free surface [38].

The potentiodynamic curve of laser-melted samples showed a longer region of passivity spanning around 0.2-0.23 V range indicating vast reduction in anodic current. This could be attributed to the homogenous passive stable film formation and thereby enhance pitting corrosion resistance. Comparing cathodic part of the polarization curves in both laser melted and untreated surfaces provide further insight into the effect of constituent cathodic particles on corrosion behavior. Indeed presence of high amounts of such phases in untreated surface contributed to increase in cathodic activity and thereby enhancing corrosion attack.
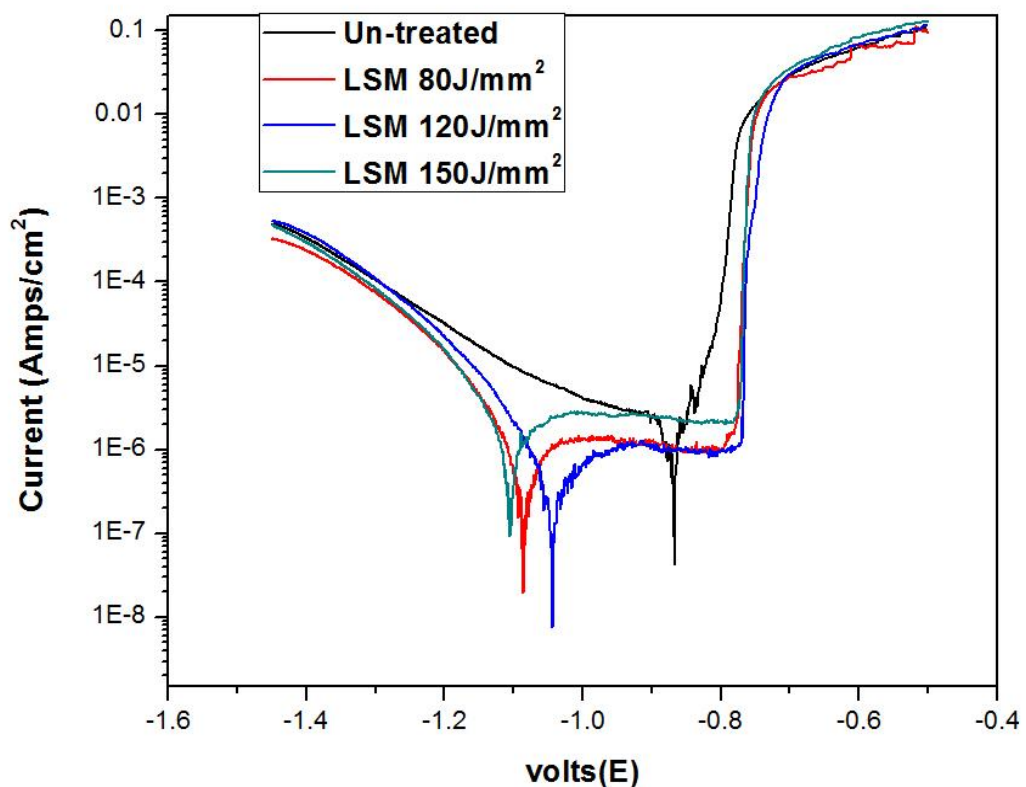

Figure 5.11: Shows the potentiodynamic polarization plots for the laser-treated and the as-received

From the EDS analysis, the formation of zinc in solid solution in the LSM layer creates a relatively active layer, and act as anodic with respect to the matrix alloy and determines the electrochemical behavior [122]. The decrease in the cathodic reactivity and the increase in the anodic activity of the melted treated layer may attributes for the change in the electrochemical behavior of the surface, which revealed only one breakdown potential.

Indeed XRD results previously reported, indicating vast reduction in such precipitates due to laser melting, corroborated these aspects. In a similar study characterizing corrosion behavior of Al-7075-T651, development of pitting at the particle-matrix interface was found primarily responsible for pitting corrosion [118]. Thus, formation of continuous passive film in the laser-melted layer improved overall corrosion resistance.

5.4.2 Electrochemical Impedance Measurements.

In order to understand and analyze possible mechanisms and reactions of electrochemical corrosion in case of both laser-melted and untreated conditions, impedance measurements of the EIS experiment are evaluated and depicted in form of *Nyquist* and bode plots plotted. The EIS plots suggest well-defined loop in high-frequency range and poorly defined one in the low-frequency range. The EIS plots show one time constraint with inductive effect for the untreated Aluminum sample show in Figure 5.12. The C_{dl} is the capacitance of the electric double layer formed after electrode/electrolyte interface and R_{ct} is the charge transfer resistance. The circuit used for LSM sample shows two-time constraint, where C_{coat} and R_{coat} give the capacitance and resistance of the treated part along with the electrode/electrolyte interface. The Equivalent circuits for untreated and laser surface melted sample shown in Figure 5.13**.** The data obtained after fitting is given in the table 5.3. The R_{ct} charge transfer resistance of the bare sample is 790.7 $\Omega.cm^2$ and it is improved after laser surface melting. As compared with the untreated sample, the total resistance (Rcoat + Rct) of laser surface melted sample has been increased by 4-8 times. The results obtained are in concurrence with previously obtained with potentiodynamic polarization test. For the untreated specimen, due to presence significant amounts of coarse constituent particles, the initial oxide film may not provide adequate protection due to discontinuous film formation and the particles themselves can promote localized corrosion

attacks. For the laser melted specimen, the elimination of coarse primary constituent particles definitely inhibited localized corrosion and improved the continuity of the film. As a result, film resistance increased and thereby imparting good corrosion resistance.

sample	Rs $\Omega.Cm^2$	Ccoat F/Cm^2	n1	R coat $\Omega.Cm^2$	Ccdl F/Cm^2	n2	Rct $\Omega.Cm^2$	$\chi 2$	Icorr $(A.Cm^2)$	Ecorr (V vs SCE)	Corrosion rate (MPY)
									Data from polarization plots		
Un-treated	0.957	-	-	-	3.23E-5	0.94	790.7	0.027	3.42E-6	-0.88	1.50
80 J/mm^2	1.985	2.4E-5	0.88	1395	0.000357	0.81	1618	0.005	9.54E-7	-1.08	0.42
120J/mm^2	1.858	2.1E-5	0.9	1878	0.00043	0.67	4644	0.004	4.15E-7	-1.04	0.194
150 J/mm^2	2.047	2.4E-5	0.89	2095	0.00054	0.97	1981	0.008	7.23E-7	-1.09	0.31822

Table 5.3: Corrosion rates of untreated and laser treated samples in potentiodynamic polarization test done in 3.5 wt% NaCl solution and calculated values for the various equivalent circuit elements at OCP
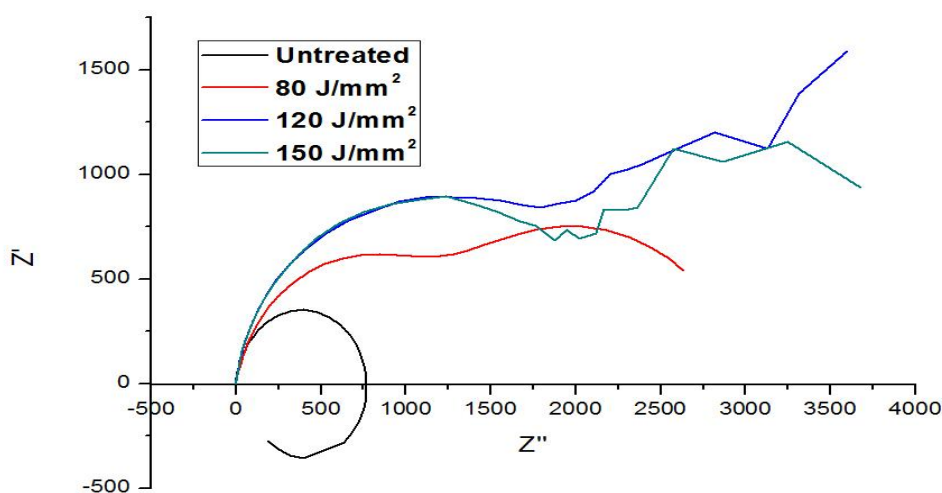
Figure 5.12: The Nyquist plots of untreated and laser treated samples
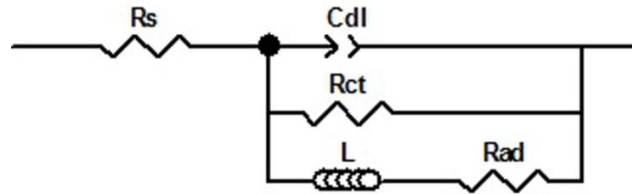
(a)
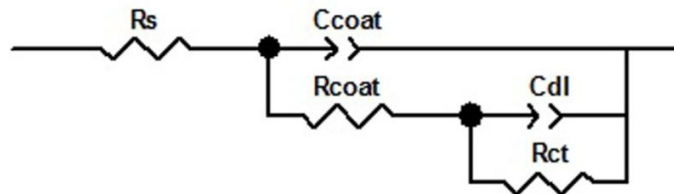
(b)

Figure 5.13: Equivalent circuits for insertion reactions; where R_S is the electrolyte resistance, R_{coat} is the film resistance, L inductance, R_{ct} is the charge-transfer resistance, C_{coat} is the film capacitance, C_{dl} is the double-layer capacitance.(a) Equivalent circuits for as received material (b) Equivalent circuits for laser treated samples.

5.5 Chapter Summary

HPDL surface melting of 7075-T651 alloy processed with wide range of energy density (80 -200 J/mm^2) produced defect-free layer. The re-solidified laser-melted layer got refined with elimination of detrimental constituent particles and grain boundary network present in wrought structure. From SEM–EDS analysis after LSM observed that fine structure about 3–5, μm dispersed uniformly throughout the surface. After laser surface melting all the constituent particles such as Mg$_2$Si, AlCuMg and Al7Cu$_2$Fe were absent. The corrosion resistance of aluminum alloy increased about 4 to 8 times owing to laser melting and is attributed to high

resistance of the film and its adequate passive film formation. Elimination of coarse constituent particles in refined melted microstructure indeed could provide adequate protection against corrosion attack at particle–matrix boundaries. Electrochemical impedance measurements taken during the corrosion test showed high film resistance in laser-melted layer as compared to untreated substrate specimen

CHAPTER 6

(c) Results and Discussion on Influence laser Surface Cladding on Surface Hardness and Corrosion Properties of 7075 Aluminum alloy

6.1 Introduction

In the process of laser surface melting the hardness has reduced to 121 – 132 HV in the melted region as against the unaffected substrate hardness of 160 – 165 HV. The reduction in hardness in between 1.5-3 mm deep melted region could attribute to the elimination of hard primary precipitates previously present in wrought microstructure. This work intended to increase the surface hardness as well as the corrosion properties by incorporating the refractory materials such as B_4C, graphite and Al_2O_3 to produce a surface composite like structure and to enhance the surface hardness.

6.2 Laser cladding

Laser cladding has done to improve the surface hardness properties of Al 7075, which were declined in the laser surface melting process. In addition, the purpose of adding ceramic powders as cladding material behave like insulators, which serve barrier for the charge transfer from the corrosion media to the surface of the material thereby, enhancing the corrosion properties. In this work, it has been observed that cladding done with nano powders resulted poor surface finish over the surface as shown in figure 6.1.

Figure 6.2 shows the SEM image of cladded sample with B_4C micron powder resulted in a uniform clad layer of 200 micron thick. In addition, cladding with graphite powder resulted in homogeneous layer. Figure 6.3 shows the SEM –EDS line scan on the treated sample, which shows the presence of the boron and carbon along with the alloying elements present in the clad layer. In addition, the SEM image reviles the aluminum alloy matrix has sound bonding with the B_4C particles
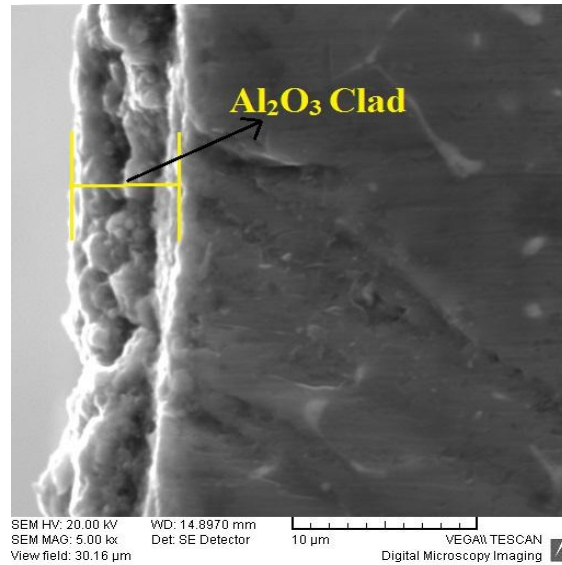
Figure 6.1: SiC cladding over the 7075 Al alloy substrate.
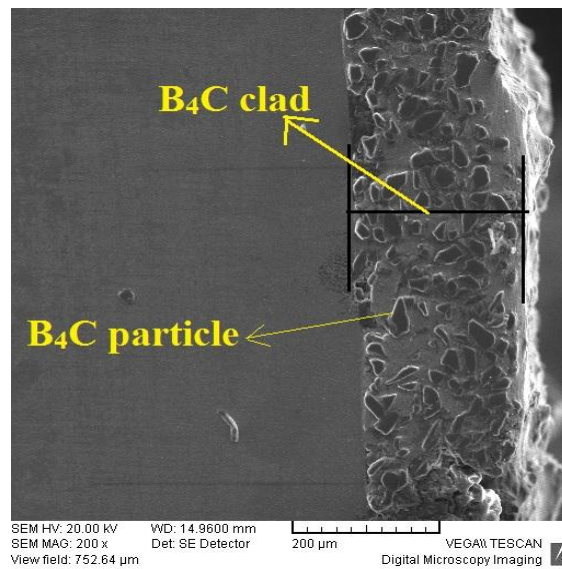
Figure 6.2 : SEM image of laser cladding of AL 7075 with B4C powders
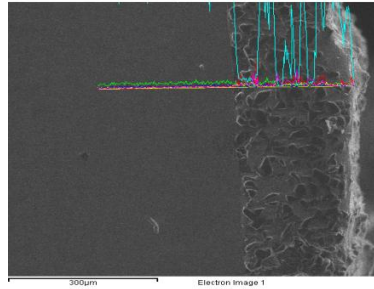
(a)
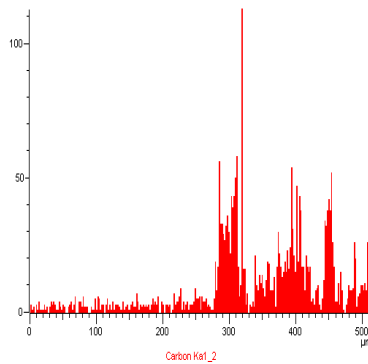
(b)
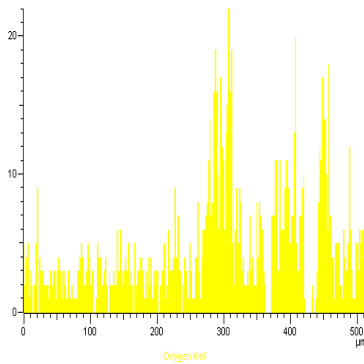
(c)
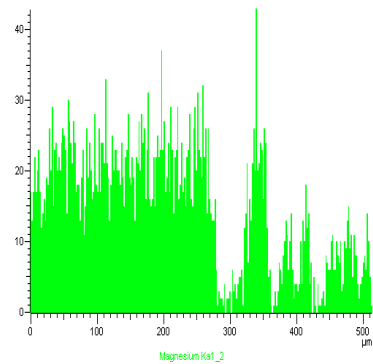
(d)
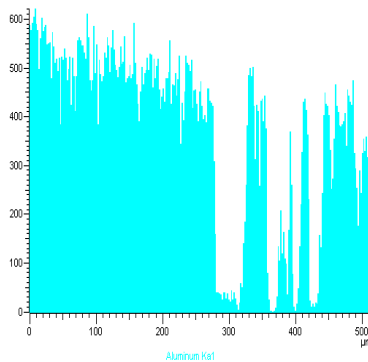
(e)
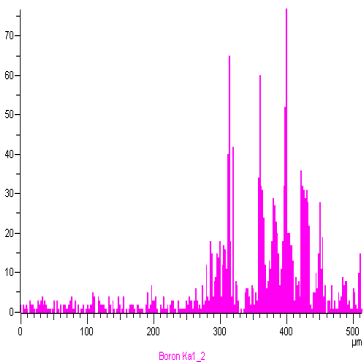
(f)
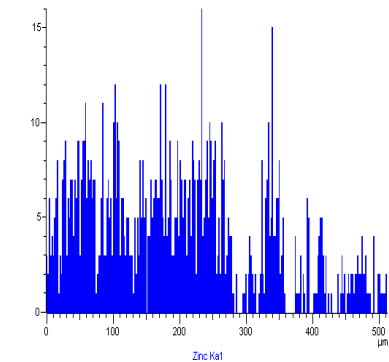
(g)

Figure 6.3: Shows the SEM- EDS line scan of cross-section of (a) B_4C clad layer (b) Carbon (c) Oxygen, (d) Magnesium, (e) Aluminum, (f) Zinc, (g) Boron.

6.3 XRD analysis

Figure 6.4 illustrates the XRD analysis of the sample cladded with graphite, Al_2O_3 and B_4C particles. A high intensity of peak was observed in the low angle X-ray diffraction of the graphite coated sample. This intensity was high due to the presence of carbon in the laser melted region. The constituent intermetallic phases such as Mg_2Si, AlCuMg and Al_7Cu_2Fe which were present in untreated sample observed to be absent in all the clad samples. Their absence might be due to re-dissolve into solution during the laser melting and arrested in solution during solidification. Similarly, in XRD analysis of Al_2O_3 laser clad on 7075 aluminum alloy shows the presence of the Al_2O_3 phase along with the Aluminum matrix. While in B_4C laser claddings on the matrix show the presence of B_4C phase along the formation of Al_3BC phases on the cladded surface.
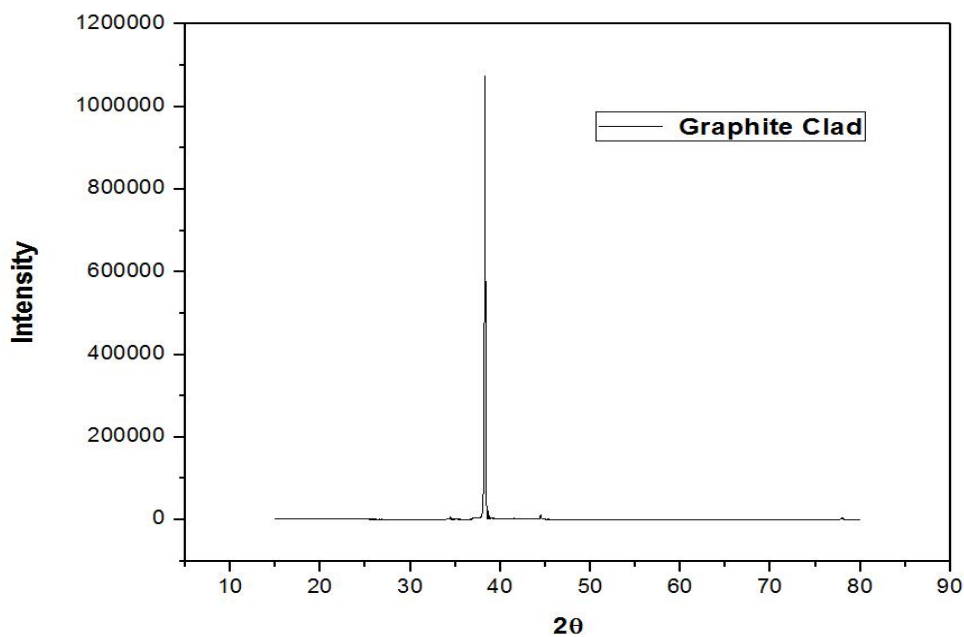
(a)
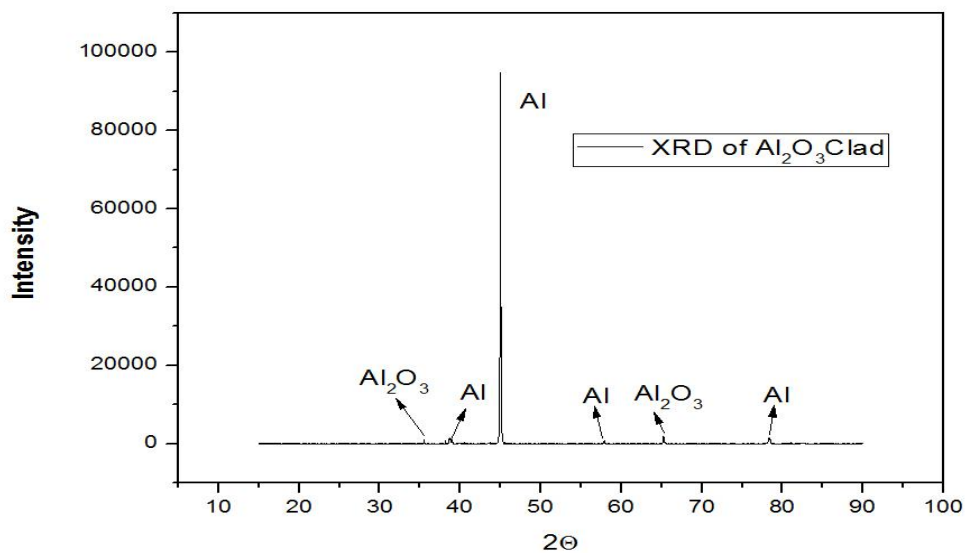
(b)
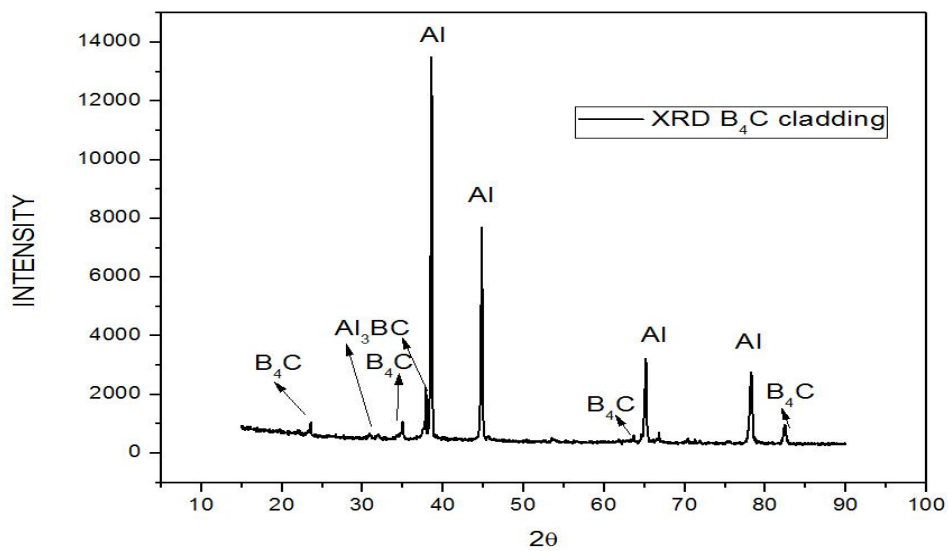
(c)

Figure 6.4: XRD analysis of laser cladded sample (a)graphite clad(b) Al_2O_3 clad(c)B_4C clad.

6.4 Hardness distribution

Hardness profiles of the laser surface melted and laser clad sample are illustrated in figure 6.5. The surface hardness of the clad sample vastly improved when compared laser surface melted samples. The increase in hardness attributed due to formation of hard layer over the surface of the treated sample. The surface hardness of the B_4C clad sample are equal to the untreated surface hardness.
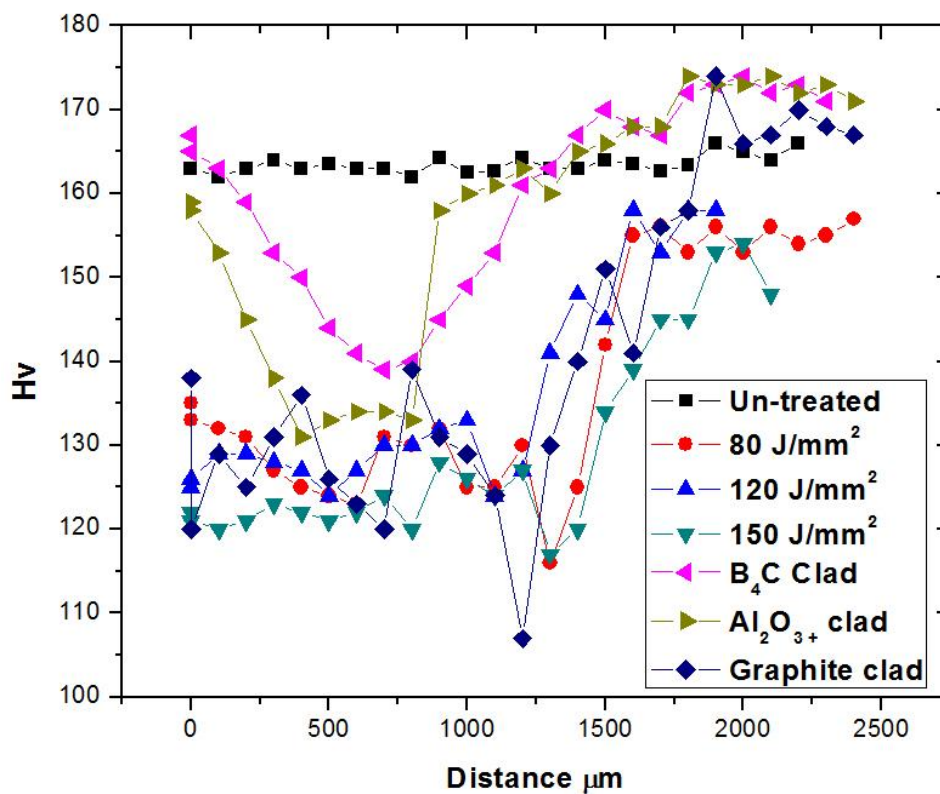
Figure 6.5: Micro Hardness on the untreated, laser treated and laser Cladded samples.

6.5 Corrosion test

Figure 6.6 and Table 6.1 shows the polarization plots and polarization data of untreated, laser surface melted and laser clad samples respectively. It was observed that the laser cladding has shown improvement in corrosion resistance to some extent. It was observed that the corrosion resistance has been increased about 5 times in B_4C laser clad sample whereas sample Al_2O_3 clad layer has resulted in 6 times increase in corrosion resistance as compared with the unrelated sample. The drop in corrosion rates were attributes due to presence of hard-insulated layers, which restrict the transfer of charge resulting in enhancement of corrosion resistance.

Figure 6.7 and table 6.1 shows the nyquist plots and impedance data respectively. It is clear from the loop contours that laser melted surface samples and laser clad with Al_2O_3 and B_4C samples depicted a remarkable enhancement in corrosion resistance as compared to untreated substrate. The increase in corrosion resistance in clad samples may attribute to high electric resistance offered by clad layer on the 7075 Al alloys. In addition, the microstructure of the laser cladding are compact and Al_2O_3 and B_4C particles are nonmetallic material also, these particles over the surface of the alloy minimizes the actual corrosion area/activity of the alloy. While in case of graphite cladding, shows a drop in corrosion resistance (Rcoat+Rct) compared to other clad system as graphite act as a conductor and helps in charge transfer from the electrolyte to alloy surface the same phenomenon was also observed from the potentiodynamic polarization data.
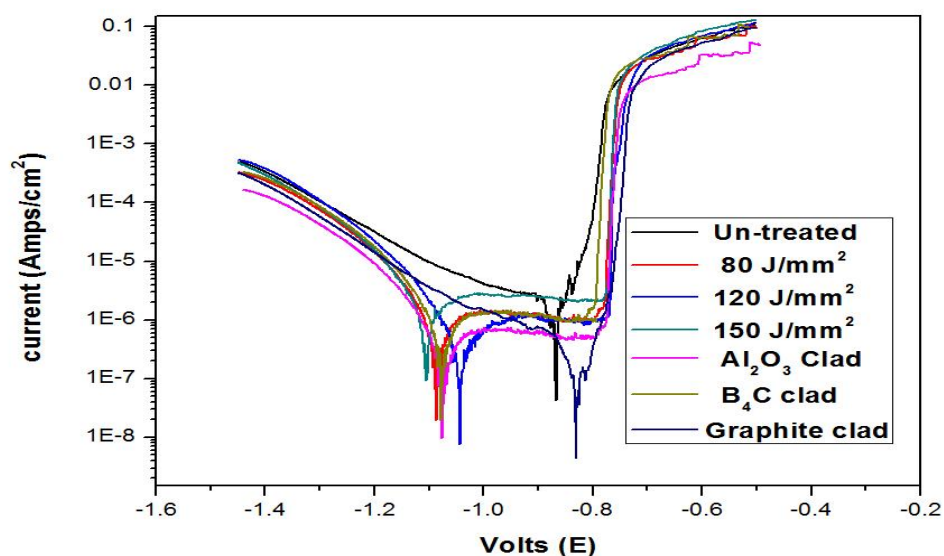
Figure 6.6: Shows the potentiodynamic polarization plots for the as –received and laser surface melting and are compared with the laser cladded samples.

Sample	Icorr (A.Cm^2)	Ecorr (V vs SCE)	Corrosion rate (MPY)
Un-treated	3.42E-06	-0.88	1.5
80 J/mm^2	9.54E-07	-1.08	0.42
120J/mm^2	4.15E-07	-1.04	0.194
150 J/mm^2	7.23E-07	-1.09	0.318
Graphite clad	2.093-6	-0.83	0.92
B$_4$C clad	6.70E-07	-1.06	0.295
Al$_2$O$_3$ clad	5.76E-07	-1.07	0.252

Table 6.1: Corrosion rates of untreated and laser treated samples in potentiodynamic polarization test done in 3.5 wt% NaCl solution
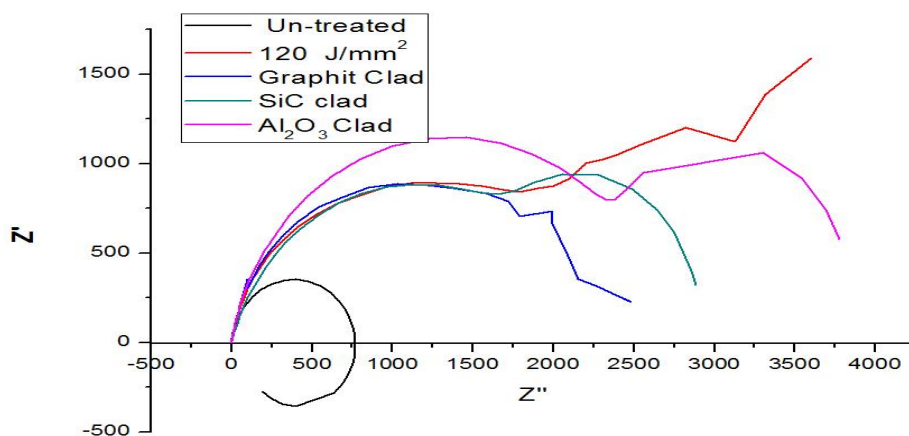
Figure 6.7: The Nyquist plots of laser-clad samples, compared with untreated and laser treated samples

Sample	R_s $\Omega.Cm^2$	C_{coat} F/Cm^2	n_1	R_{coat} $\Omega.Cm^2$	C_{cdl} F/Cm^2	n^2	R_{ct} $\Omega.Cm^2$	χ^2	$R_{coat}+R_{ct}$
Un-treated	0.957	-	-	-	3.23E-5	0.94	790.7	0.027	709
80 J/mm^2	1.985	2.4E-5	0.88	1395	0.000357	0.81	1618	0.005	3013
120J/mm^2	1.858	2.1E-5	0.9	1878	0.00043	0.67	4644	0.004	6522
150J/mm^2	2.047	2.4E-5	0.89	2095	0.00054	0.97	1981	0.008	4076
Graphite clad	2.016	2.88E-5	0.92	1868	0.00032	0.82	548	2.016	2416
B^{4}C clad	0.16	9.2 E-5	0.83	2211	0.00101	0.98	861.1	0.004	3072
Al$_2$O$_3$ clad	0.99	2.81 E-5	0.89	2637	0.0006	0.98	1423	0.002	4060

Table 6.2: Calculated values for the various equivalent circuit elements at OCP
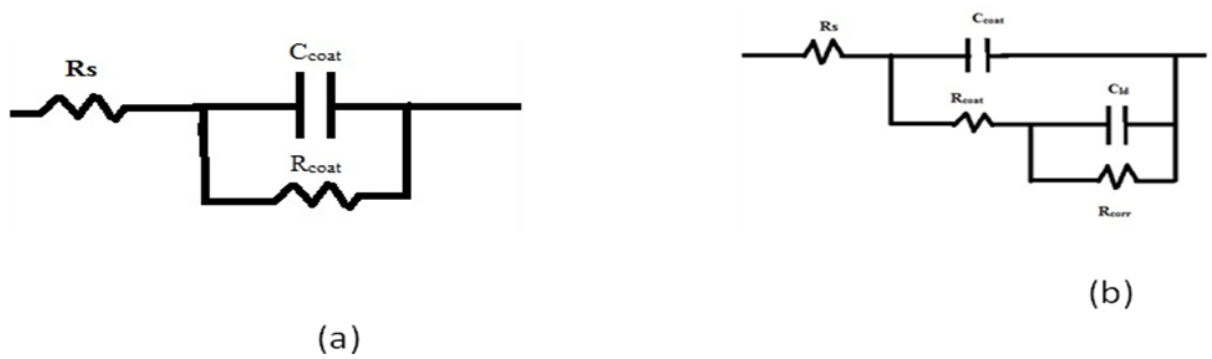
Figure 6.8: Equivalent circuits for insertion reactions; where R_S is the electrolyte resistance, R_{coat} is the film resistance, R_{corr} is the charge-transfer resistance, C_{coat} is the film capacitance, C_{dl} is the double-layer capacitance.(a) Equivalent circuits for as received material (b) Equivalent circuits for laser treated samples.

6.6 Chapter summary

The main aim of this work is to increase the surface properties such as hardness, which was lacking in the laser surface melting process. By incorporating the ceramic material, such as Al_2O_3 and B_4C not only increased the surface hardness but also corrosion properties also well maintained as that of laser surface treated samples.

CHAPTER 7

(d) Results and Discussion on COMSOL Realization of Laser Surface Melting

7.1 Introduction

This chapter present the effect analytical model of laser source on the melt pool profiles and thermal stress generated during the melting process were predicted and are compared with the actual experimental data.

7.2 COMSOL Realization of Laser Surface Melting

Using COMSOL multiphysics analytical model of laser source was constructed which resembles the actual High Power Diode Lasers (HPDL) source used in the experimentation of laser surface melting process. The temperature evolution and thermal stresses generated during surface treatment were predicted through this simulation. In this work, the process parameters were chosen exactly same as that of the actual parameters used in LSM experiments. The various results from this simulation are calculated on the reference lines as shown in figure 7.1.
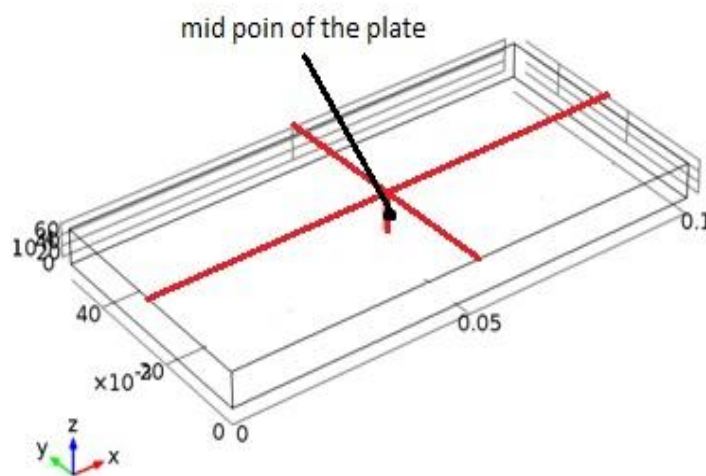
Figure 7.1: The temperature and the thermal stress profile are calculated reference lines as shown.

In laser surface-melting process has extremely short interaction time between material surface and laser beam thus LSM involves highly chemical, metallurgical and physical phenomena which includes fast melting and solidification process and solid liquid transformations. The duration time from the surface in the laser incident region starts to melt to the eventually solidification process is known as liquid lifetime, is introduced to analyze the molten pool dynamics. It was observed that the peak temperature decreased with the increase of scan speeds. This is because when the scan speed of laser beam increases, the interaction time between surface and laser beam decreases and thus results in a lower peak temperature.

Figure 7.2 represents the temperature evolution with respect to time at a particular point on the model surface. The sample simulation carried out with heat input of 1000 J/mm (3000W,3 mm/s ; laser energy density of 200 J/mm^2) observed to have extended cooling curve and time taken to reach ambient temperature is high as compared with simulation carried out with other parameters. Owing to the slow scan speeds in this particular simulation provides larger interaction time between the laser source and the modeled sample surface and tends to absorb more heat energy from the laser source and retain in the model for some extent. Further, the dissipation of heat depends on the thermal properties of the material and ambient condition. The retained heat for long duration increase the internal energy resulting in prolonged phase change and further delay the solidification process. In addition, from figure 7.6 (d) observed that spread of thermal stress over the surface are high when compared with the other simulation shown in figure 7.6. From the above observation due to larger interaction periods, the life time of the melt pool is increased which may produce too much liquid and form a large molten pool that was difficult to control owing to surface irregularities after solidification. The same observation were made when the Al 7075 sample was laser surface treated with heat input of 1000 J/mm which has been illustrated in figure 6.1 in section 6.2.

In the mid region of the all the laser treated surfaces exhibited temperature above the melting temperatures. The laser heat input of 800 J/mm (4000W, 5 mm /s; laser energy density of 100 J/mm2) recorded high temperatures as compared with the other laser intensities which has depicted from figure 7.2 and 7.3(a). It was also, observed that the temperature in this energy density was experiencing near vaporization temperature. Various physical properties of the elements in 7xxx alloys are shown in appendix 1B. It has been reported that material experiencing high heat input for the short duration of time (or rapid cooling) results larger thermal gradients. The larger the thermal gradients the larger will be the thermal stresses [117, 124]. Upon rapid cooling of high temperature laser spot, the entire region of the laser-treated track will be in tension. Specifically, the laser track receives tensile hydrostatic pressure stresses. The high stresses generated over the model surface can be observed from figure 7.6(b) the von-mises stresses recorded high values as compared with the other simulated parameters, similar observation were made from figure 7.3 (b). These tensile hydrostatic pressure stresses upon cooling will result in the shrinking of the laser track as compared with surrounding substrate resulting surface and subsurface cracks. This phenomenon was observed as in sample experimentally treated with mentioned laser parameters and has been illustrated in figure 6.1 in section 6.2.

In a summary, it has observed that the with slow scanning speeds resulting in heavy undulation on the surface. Whereas, the sample with high temperature at the surface and with rapid or fast cooling resulted in the surface and sub-surface cracks. Therefore, with the application of this computer simulation a proper process parameters can chosen to attain a sound laser modified Surface.

Figure 7.5 (a) illustrate the temperature profiles at the midpoint of the treated surfaces for different laser energy densities. The results were simulated when laser treatment carried out along the lasing direction. It has been observed that the there is gradual decay of temperature profile behind the laser spot. This attributes to the fast cooling due to boundary condition such as conduction, convection and radiation heat transfer properties applied over surface in this work. The von mises stress represents residual stress developed over the surface of the processed material. Figure 7.5 (b) shows von misses stress along the midpoint of the plate with respective to the lasing direction. The von-mises stress increases to reach its maximum and remains high up

to the region where the heat source is located. Generally, the von mises stress follows almost the temperature gradient that is it attains high values in the region where the temperature gradient is high the same has been observed in this work.
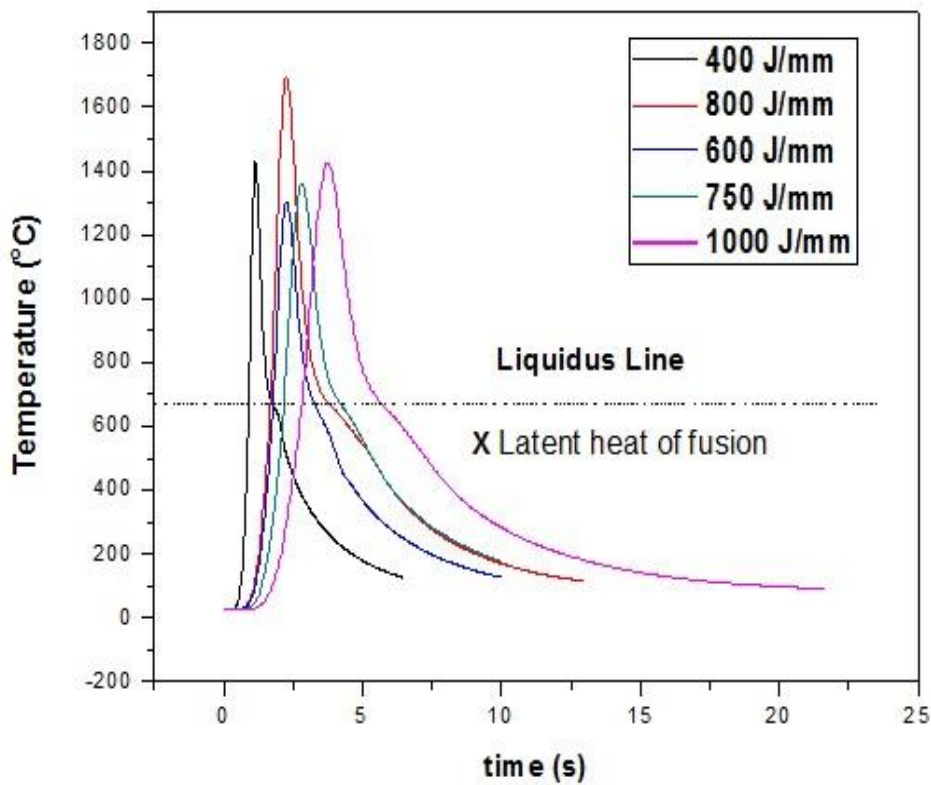
figure 7.2: Variations of temperature with time at the centre point of the laser track for different laser energy densities. Point X shows increase in temperature owing to the latent heat released during the phase change from liquid to solid.
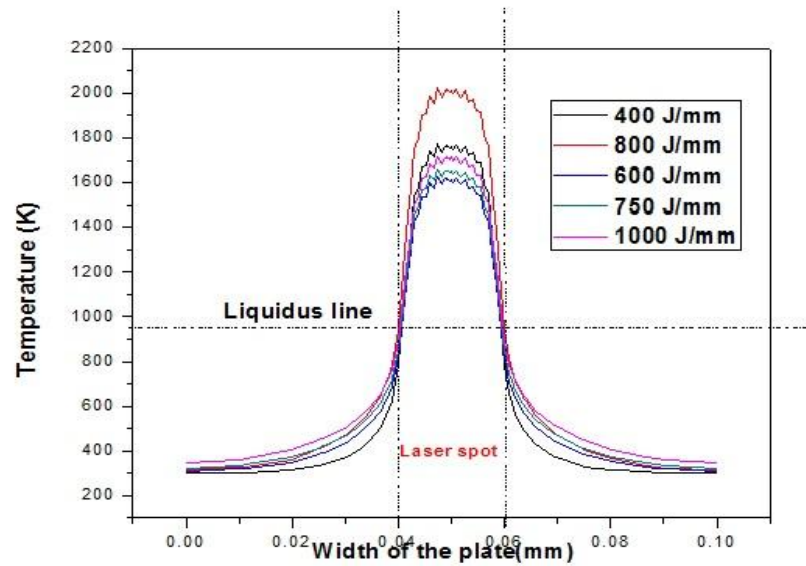
(a)
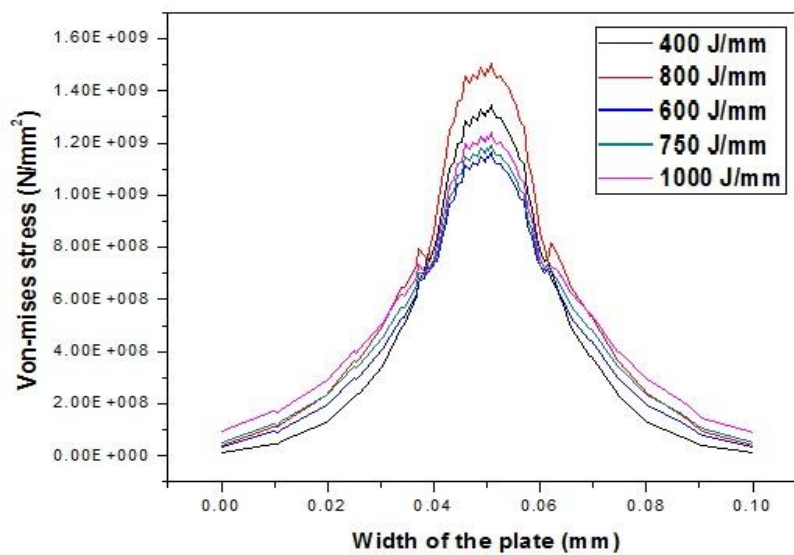
(b)

Figure 7.3 : (a) Variation in temperature along the width of the laser track and (b)
corresponding variation of Thermal stress generated across the laser track

(a)

(b)

(c)

(d)
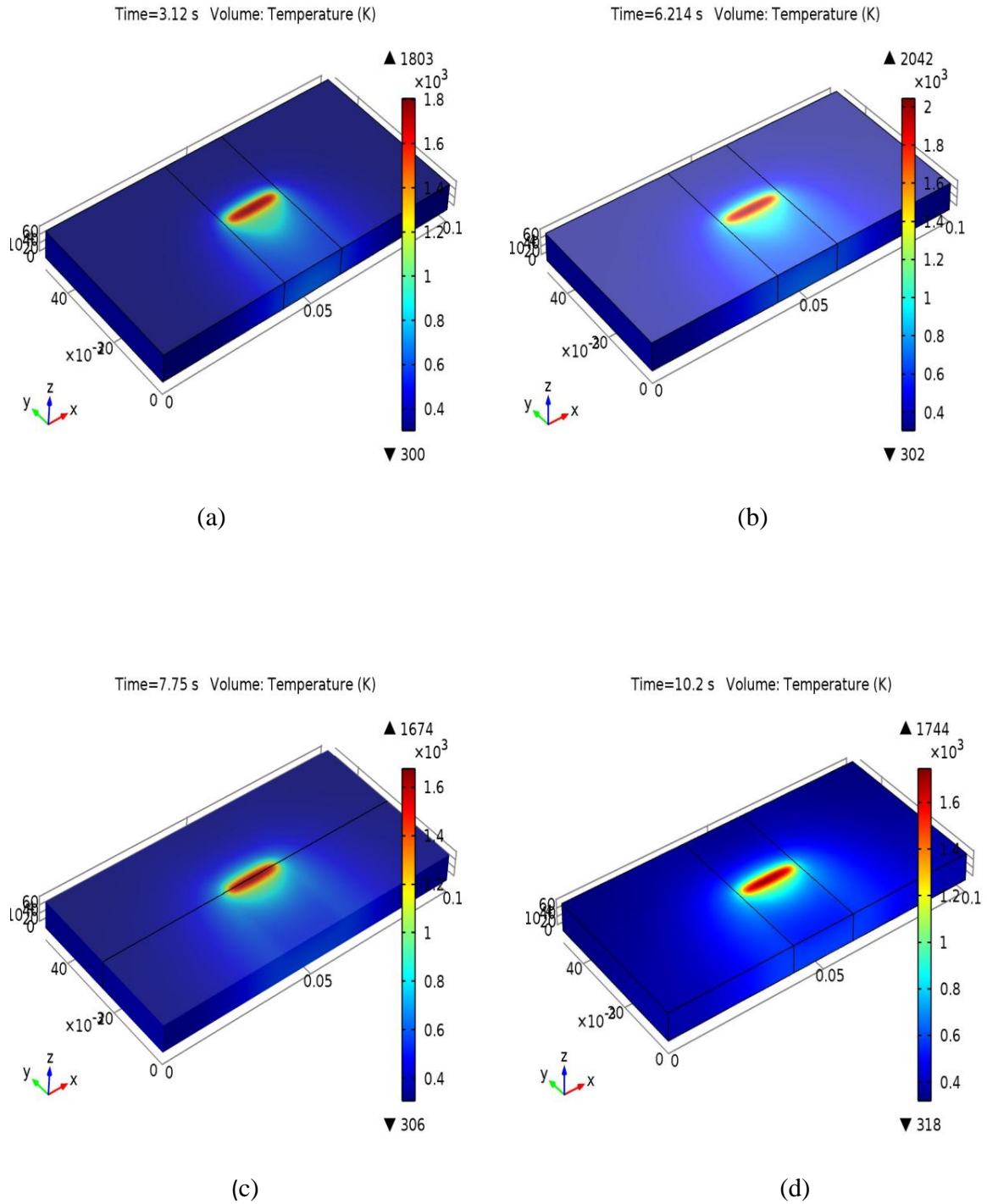
Figure 7.4 : Temperature distribution on domain of the work piece (a)400 J/mm, (b) 800 J/mm , (c) 750 J/mm (d) 1000 J/mm along the lasing direction.

The sharp transformation of von-mises stress behind the peak laser density is due to the sharp drop of the temperature gradient. The second peak from figure 7.5(b) behind the peak (laser spot) developed because of high thermal strains formation in this region due to rapid solidification, as the substrate material does not expand or solidify freely. Therefore, thermal expansion or solidifications are much difficult due variation in temperature gradient, which resulted in residual stresses. This condition is also observable from plane view of the residual stress shown in figure 7.6.

Figure 7.7 illustrate the variation of the temperature and von mises along the thickness of the plate. It has observed that the sharp decay in the temperature at the surface region and temperature drop becomes steady as the depth below the surface increases towards the solid bulk figure 7.7 (a). The sharp decay at the surface is because of convection cooling at the surface region as it is exposed to the ambient conditions. In addition, the large temperature gradient at the surface increases the conductivity heat transfer rate from the surface area into the solid mass of the material, which contributes to sharp drop of temperature in the surface region.

From figure 7.7(b) it has observed that the von mises stress distribution pursues nearly similar as the temperature distribution in the surface region. Von-mises stress decreases sharply from its high value as the depth below the surface increases. Furthermore, the decline von-mises stress becomes gradual as the depth below the surface increases due to the thermal strain developed in this region. Thus, in this region, von-mises stress does not pursue temperature distribution. At the final depth of the bulk sample stresses tends to increase due model was fixed constrained. The laser intensity has significant influence on von-mises stress developed especially in the surface region. Increasing intensity raises the temperature gradient which in turn increases von Mises stress levels.
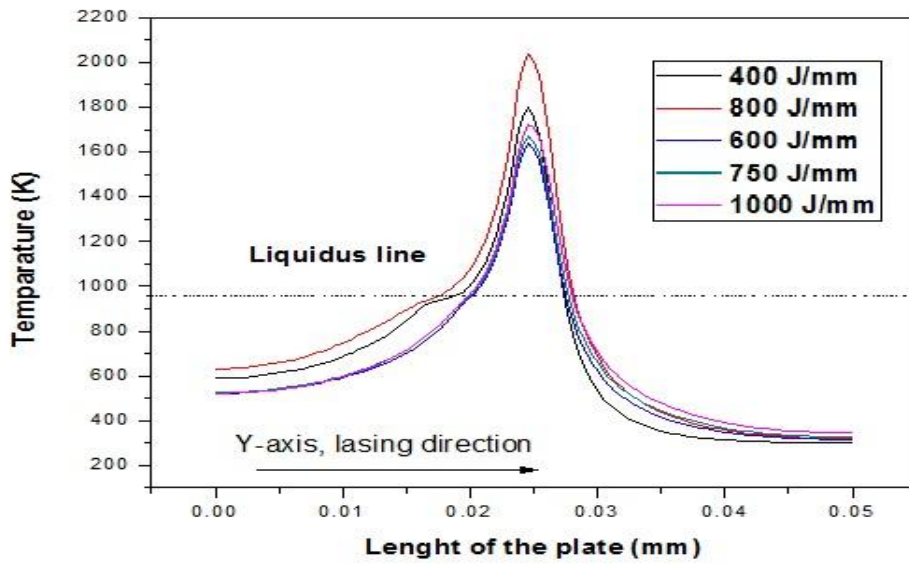
(a)
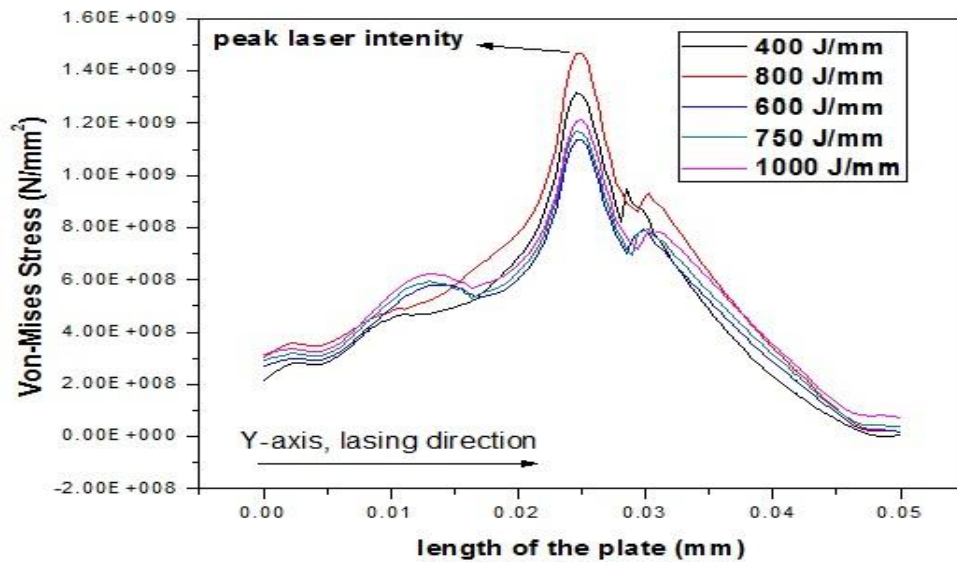
(b)

Figure 7.5: (a) Temperature and (b) von-Mises stress variation at the surface midpoint of the plate .

(a)

(b)

(b)

(d)
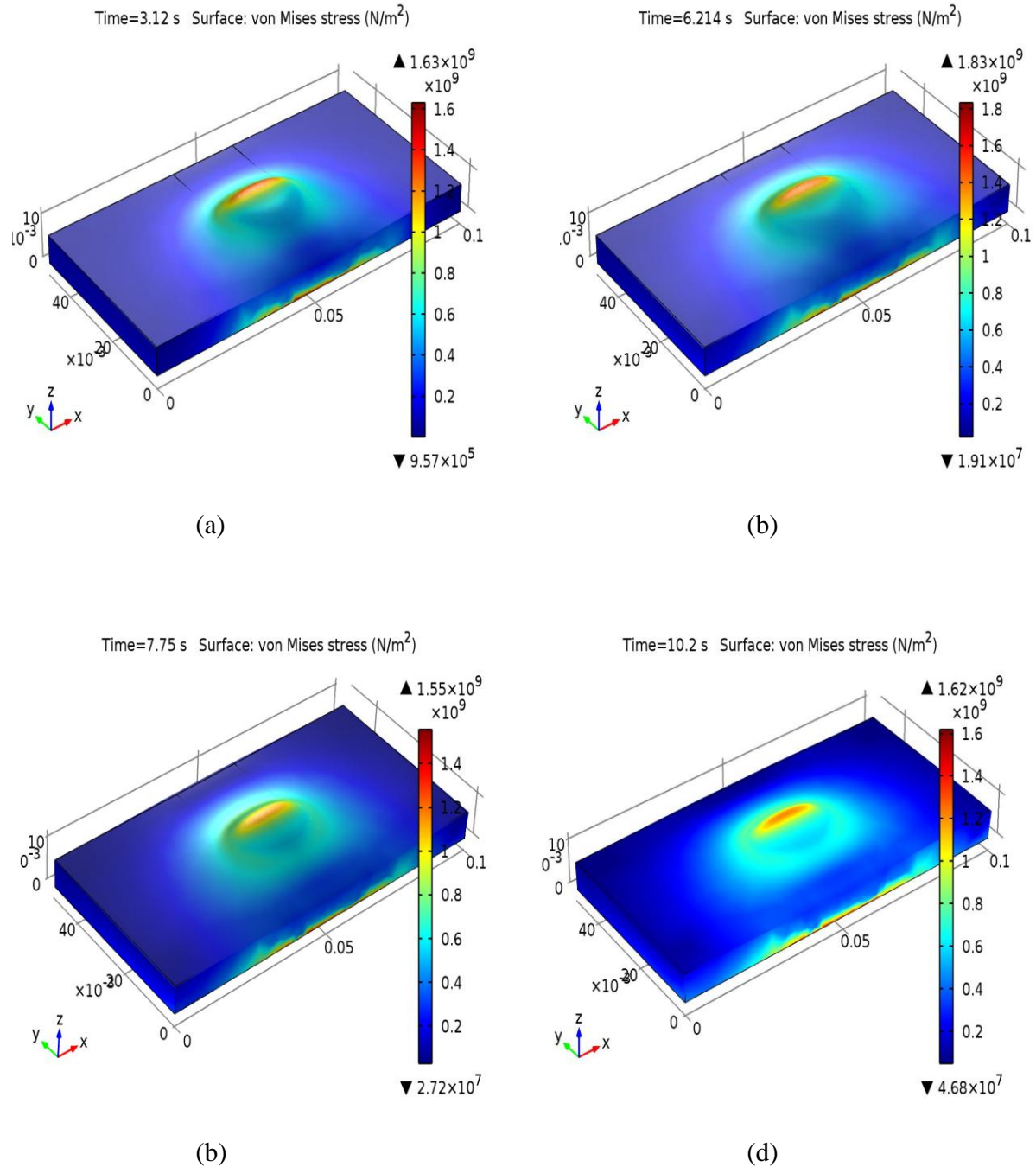
Figure 7.6 : Von Mises stress contours in the half surface domain of the work piece (a)400 J/mm, (b) 800 J/mm , (c) 750 J/mm (d) 1000 J/mm along the lasing direction.
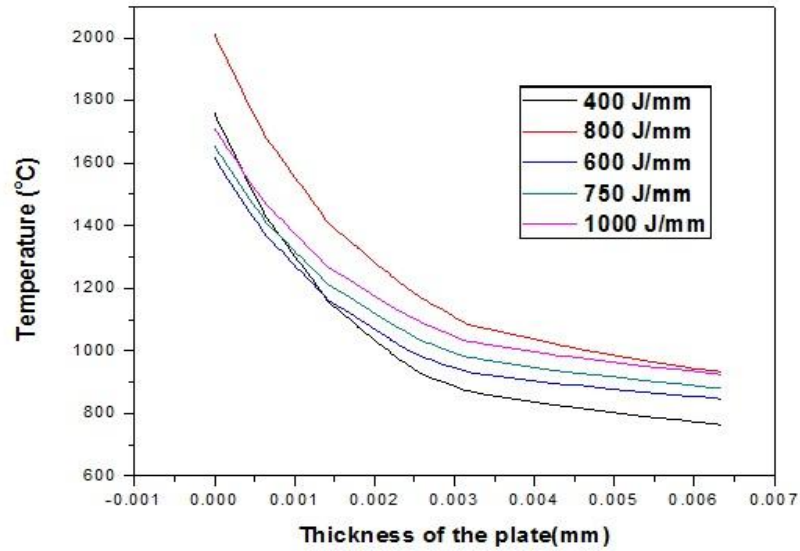
(a)
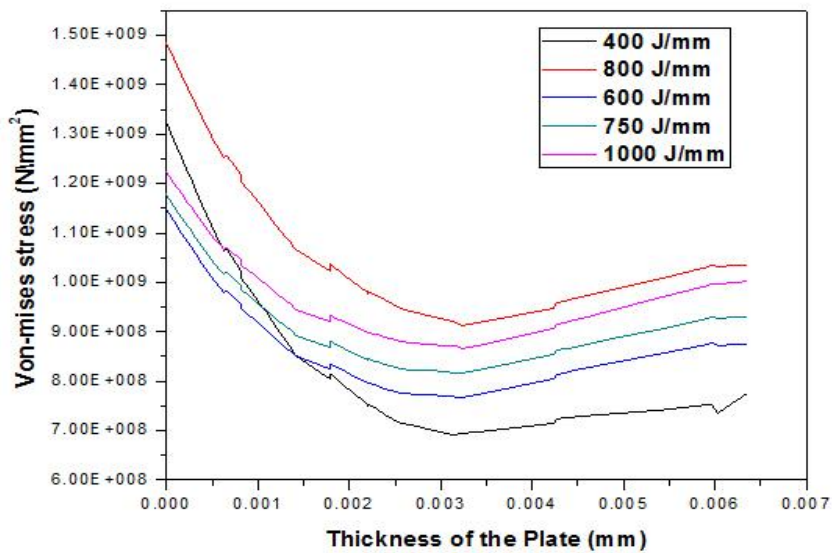
(b)

Figure 7.7 : Illustrate the variation of the (a) temperature and (b) von mises along the thickness
of the plate in the mid region of the plate i.e., along the z-axis.

The various melt depths in the COMSOL Multiphysics computational model and actual experimental depth are summarized in figure 7.8. The cross-sections images of the simulation results are shown next to the experimental results (same scale). The three zones in the cross-section that are melt zone, interface zone and heat affected zone are clearly observed. In simulated model lased with energy density of 80 J/mm^2, the measured melt depth (1.7 mm) is deeper than the experimental value (1.5 mm). Whereas sample simulated with the energy density of 120 J/mm^2 has a melt depth of 2.2 mm as compared with the experimental value (1.8 mm). The measured melt depth (2.5 mm) is deeper than the experimental value (2.3 mm) in the case of sample lased with energy density of 150 J/mm^2. This is attributed to many factors, among which the underestimated absorptivity and heat transfer coefficients are the most significant. Using COMSOL Multiphysics the melt depth, temperatures developed with various lasers intensities and the stress developed can be predicted successfully.
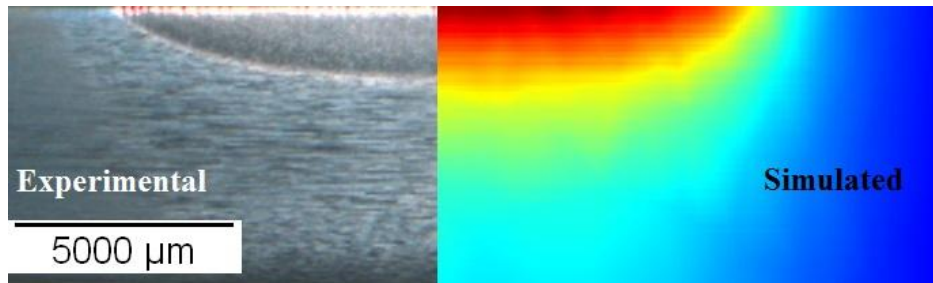
(a)
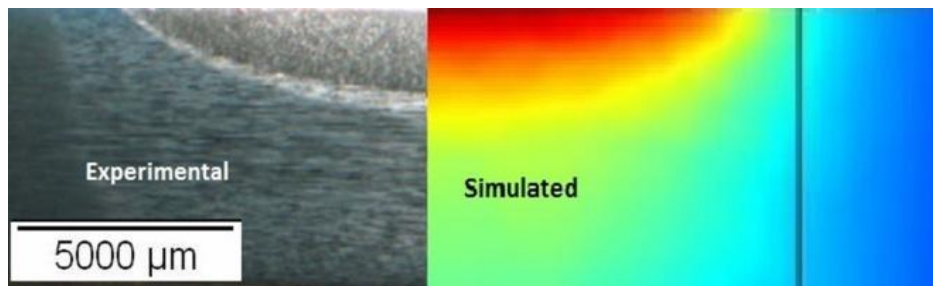
(b)
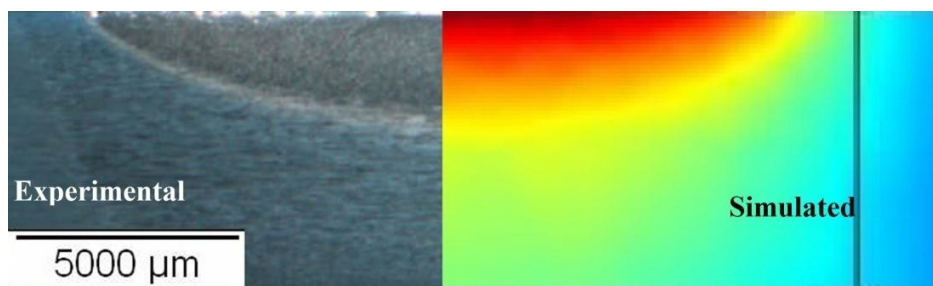
(c)

Figure 7.8: Comparison of experimental laser melted depths with that of COMSOL simulated laser melted depths. (a)400 J/mm, (b) 600 J/mm , (c) 750 J/mm.

7.3 Chapter summary

The COMSOL simulated model given a reasonable prediction of melt pool shape and can be successfully employed to help optimize overlap required for laser surface processing applications. Using COMSOL multiphysics, the melt depth, temperature developed with various laser intensities and residual stresses generated were predicated and are well validated with the experimental data.

CHAPTER 8

Conclusion and Scope of Future Work

8.1 Conclusions

- In the thermo-mechanically treatment of 7075 Al alloys, It was observed that the sample with high cold reduction and annealed at high temperatures has resulted in high corrosion resistance both in SSRT and potentiodynamic polarization tests.

- The corrosion products were formed over the surface of the sample during test due to prolong immersion in alkaline media. The formed corrosion products will act as the barriers for the further hydrogen diffusion and anodic dissolution.

- Diode laser surface melting of 7075-T651 alloy processed with an energy density of 80-200 J/mm^2 produced 1.8-3 mm deep defect-free layer with complete elimination of coarse primary constituent particles previously present in untreated substrate.

- The refined microstructure of the melted layer comprised of uniformly distributed fine secondary hardened precipitates of MgZn$_2$ in a matrix of Al-rich cellular/dendrite grains.

- The pitting corrosion resistance increased four to eight folds owing to laser melting and attributed to high resistance of the film and its adequate passive film formation.

- Elimination of coarse constituent particles in refined melted microstructure indeed could provide adequate protection against corrosion attack at particle-matrix boundaries.

- Electrochemical impedance measurements taken during the corrosion test showed high film resistance in laser melted layer as compared to untreated substrate specimen.

- Laser cladding has shown improvement in corrosion resistance and in surface hardness which was lacking in the laser surface melting. The improvement was due to presence of hard and compact non-conducting clad layer over the Al 7075 alloy.

- Using COMSOL multiphysics the melt depth, temperature developed with various laser intensities and residual stresses generated were predicated and are well validated with the experimental data.

8.2 Scope of Future Work

- Results of the studies on the corrosion properties of thermo-mechanical treated samples shown the improvement in corrosion behavior. Scope for research exists in finding out by carrying out various other thermo-mechanical treatments implementing varying degree of cold rolling and final annealing temperatures.

- The corrosion properties were evaluated in the pH of 12, Scope for research exists in studying the effect of various pH values on the SCC and corrosion properties.

- As the HPDL provides the wider and long laser treated surface areas. Scope for research exists in carrying out SCC studies on Laser surface melted samples by innovating the use of machining the thin micro- tensile specimen, which can be utilized in SSRT tests.

- Laser cladding with mention powders in this work resulted in increase in hardness as well as corrosion properties, scope for research exists to use various non-conducting powders to study the corrosion and surface properties.

- In this work, using COMSOL multiphysics the temperature profiles and melt pool depth and thermal stress has been predicted well. The COMSOL work can be extended to conduct the laser surface cladding simulation to study the marangoni effect and the iteration of molten alloy with the added powders with various process parameters.

REFERENCES

References

[1] Davis JR, Davis JR. Aluminum and aluminum alloys: ASM international; 1993.

[2] Holroyd N. Environment-induced cracking of high-strength aluminum alloys. Environment-induced cracking of metals 1990:311.

[3] Birbilis N, Buchheit R. Electrochemical characteristics of intermetallic phases in aluminum alloys an experimental survey and discussion. Journal of The Electrochemical Society 2005;152:B140-B51.

[4] Gao M, Feng C, Wei RP. An analytical electron microscopy study of constituent particles in commercial 7075-T6 and 2024-T3 alloys. Metallurgical and Materials Transactions A 1998;29:1145-51.

[5] Muller IL, Galvele JR. Pitting potential of high purity binary aluminium alloys—II. AlMg and AlZn alloys. Corrosion Science 1977;17:995-1007.

[6] Ramgopal T, Gouma P, Frankel G. Role of grain-boundary precipitates and solute-depleted zone on the intergranular corrosion of aluminum alloy 7150. Corrosion 2002;58:687-97.

[7] Liu Q, Barter S, Clark G. Internal cracking during surface treatment of 7050-T74 aluminium alloy using laser shock peening. Structural Integrity and Fracture: Proceedings of the International Conference, SIF 2002, Perth, Australia, 25-28 September 2002: CRC Press; 2002. p. 177.

[8] Fooladfar H, Hashemi B, Younesi M. The effect of the surface treating and high-temperature aging on the strength and SCC susceptibility of 7075 aluminum alloy. Journal of materials engineering and performance 2010;19:852-9.

[9] Reda Y, Abdel-Karim R, Elmahallawi I. Improvements in mechanical and stress corrosion cracking properties in Al-alloy 7075 via retrogression and reaging. Materials Science and Engineering: A 2008;485:468-75.

[10] Gao J, Quesnel DJ. Enhancement of the stress corrosion sensitivity of AA5083 by heat treatment. Metallurgical and Materials Transactions A 2011;42:356-64.

[11] RHJARE R. Stress-corrosion cracking1987.

[12] Turnbull A, Horner D, Connolly B. Challenges in modelling the evolution of stress corrosion cracks from pits. Engineering Fracture Mechanics 2009;76:633-40.

[13] Speidel MO. Stress corrosion cracking of aluminum alloys. Metallurgical Transactions A 1975;6:631-51.

[14] Albrecht J, Thompson A, Bernstein I. The role of microstructure in hydrogen-assisted fracture of 7075 aluminum. Metallurgical Transactions A 1979;10:1759-66.

[15] Talianker M, Cina B. Retrogression and reaging and the role of dislocations in the stress corrosion of 7000-type aluminum alloys. Metallurgical Transactions A 1989;20:2087-92.

[16] Burleigh T. The postulated mechanisms for stress corrosion cracking of aluminum alloys: A review of the literature 1980-1989. Corrosion 1991;47:89-98.

[17] Bobby-Kannan M, Raja V, Raman R, Mukhopadhyay A. Influence of multistep aging on the stress corrosion cracking behavior of aluminum alloy 7010. Corrosion 2003;59:881-9.

[18] Sprowls D, Brown R. Resistance of Wrought High-Strength Aluminum Alloys to Stress Corrosion: Aluminum Company of America; 1962.

[19] Haynie FH, Boyd WK. Stress-Corrosion Cracking of Aluminum Alloys. DTIC Document; 1966.

[20] Speidel MO, Hyatt MV. Stress-corrosion cracking of high-strength aluminum alloys. Advances in corrosion science and technology: Springer; 1972. p. 115-335.

[21] Rinker J, Marek M, Sanders J. Microstructure, toughness and SCC behavior of 2020. Second International Aluminum-Lithium Conference: Monterey, California; 1983.

[22] Vasudevan A, Ziman P, Jha S, SANDERS T. Stress Corrosion Resistance of Al-Cu-Li-Zr Alloys. Aluminium-lithium alloys III 1986:303-9.

[23] Holroyd N, Gray A, Scamans G, Hermann R. Environment-Sensitive Fracture of Al--Li--Cu--Mg Alloys. Aluminium--Lithium Alloys III 1985:310-20.

[24] Knight S, Birbilis N, Muddle B, Trueman A, Lynch S. Correlations between intergranular stress corrosion cracking, grain-boundary microchemistry, and grain-boundary electrochemistry for Al–Zn–Mg–Cu alloys. Corrosion Science 2010;52:4073-80.

[25] Robson J, Prangnell P. Predicting recrystallised volume fraction in aluminium alloy 7050 hot rolled plate. Materials Science and Technology 2002;18:607-14.

[26] Tsai W, Duh J, Yeh J, Lee J, Chang Y. Effect of pH on stress corrosion cracking of 7050-T7451 aluminum alloy in 3.5 wt% NaCl solution. Corrosion 1990;46:444-9.

[27] Lin J-C, Liao H-L, Jehng W-D, Chang C-H, Lee S-L. Effect of heat treatments on the tensile strength and SCC-resistance of AA7050 in an alkaline saline solution. Corrosion Science 2006;48:3139-56.

[28] Deng Y, Peng B, Xu G, Pan Q, Ye R, Wang Y, et al. Stress corrosion cracking of a high-strength friction-stir-welded joint of an Al–Zn–Mg–Zr alloy containing 0.25 wt.% Sc. Corrosion Science 2015;100:57-72.

[29] Steen WM. Laser surface treatment. Laser Material Processing: Springer; 1991. p. 172-219.

[30] Ion J. Laser processing of engineering materials: principles, procedure and industrial application: Butterworth-Heinemann; 2005.

[31] Steen W, Powell J. Laser surface treatment. Materials & Design 1981;2:157-62.

[32] Haag M, Rudlaff T. Assessment of different high-power diode lasers for material processing. Lasers and Optics in Manufacturing III: International Society for Optics and Photonics; 1997. p. 583-91.

[33] Liu Q, Yang C, Ding K, Barter S, Ye L. The effect of laser power density on the fatigue life of laser-shock-peened 7050 aluminium alloy. Fatigue & Fracture of Engineering Materials & Structures 2007;30:1110-24.

[34] Watkins K, Liu Z, McMahon M, Vilar R, Ferreira M. Influence of the overlapped area on the corrosion behaviour of laser treated aluminium alloys. Materials Science and Engineering: A 1998;252:292-300.

[35] Peyre P, Merrien P, Lieurade R, Fabbro R. Laser induced shock waves as surface treatment for 7075–T7351 aluminium alloy. Surface Engineering 1995;11:47-52.

[36] Clauer AH. Laser shock peening for fatigue resistance. Surface performance of titanium 1996:217-30.

[37] Chan C, Yue T, Man H. The effect of excimer laser surface treatment on the pitting corrosion fatigue behaviour of aluminium alloy 7075. Journal of Materials Science 2003;38:2689-702.

[38] Yue T, Yan L, Chan C. Stress corrosion cracking behavior of Nd: YAG laser-treated aluminum alloy 7075. Applied Surface Science 2006;252:5026-34.

[39] Yue T, Yan L, Dong C, Chan C. Stress corrosion cracking behaviour of laser treated aluminium alloy 7075 using a slow strain rate test. Materials science and technology 2005;21:961-6.

[40] Yue T, Yan L, Chan C, Dong C, Man H, Pang G. Excimer laser surface treatment of aluminum alloy AA7075 to improve corrosion resistance. Surface and Coatings Technology 2004;179:158-64.

[41] Gruhl W. The stress-corrosion behavior of high-strength Al-Zn-Mg alloys. Aluminium alloys in the aircraft industries 1978:171-4.

[42] Gruhl W. Stress corrosion cracking of high strength aluminum alloys. Zeitschrift fuer Metallkunde 1984;75:819-26.

[43] Gruhl W. Stress corrosion cracking of high strength aluminum alloys. Chemischer Informationsdienst 1985;16.

[44] Sarkar B, Marek M, Starke E. The effect of copper content and heat treatment on the stress corrosion characteristics of Ai-6Zn-2Mg-X Cu alloys. Metallurgical Transactions A 1981;12:1939-43.

[45] Birnbaum HK. Mechanisms of hydrogen related fracture of metals. DTIC Document; 1989.

[46] Song R, Tseng M, Zhang B, Liu J, Jin Z, Shin K. Grain boundary segregation and hydrogen-induced fracture in 7050 aluminium alloy. Acta materialia 1996;44:3241-8.

[47] Xu D, Birbilis N, Rometsch P. Effect of S-phase dissolution on the corrosion and stress corrosion cracking of an as-rolled Al-Zn-Mg-Cu alloy. Corrosion, The Journal of Science and Engineering 2012;68:035001-1--10.

[48] Wu X-z, Xiao D-h, Zhu Z-m, Li X-x, Chen K-h. Effects of Cu/Mg ratio on microstructure and properties of AA7085 alloys. Transactions of Nonferrous Metals Society of China 2014;24:2054-60.

[49] Scamans GM, Alani R, Swann PR. Pre-exposure embrittlement and stress corrosion failure in Al Zn Mg Alloys. Corrosion Science 1976;16:443-59.

[50] Chen K, Fang H-C, Zhang Z, Chen X, Liu G. Effect of of Yb, Cr and Zr additions on recrystallization and corrosion resistance of Al–Zn–Mg–Cu alloys. Materials Science and Engineering: A 2008;497:426-31.

[51] Li Z, Xiong B, Zhang Y, Zhu B, Wang F, Liu H. Ageing behavior of an Al-Zn-Mg-Cu alloy pre-stretched thick plate. Journal of University of Science and Technology Beijing, Mineral, Metallurgy, Material 2007;14:246-50.

[52] Ying-ying L, Chang-qing X, Xiao-min P. Effect of heat treatment on microstructures and mechanical properties of Al-6Zn-2Mg-1.5 Cu-0.4 Er alloy. 中南大学学报 (英文版) EI SCI 2010;17.

[53] Deng Y, Yin Z, Zhao K, Duan J, Hu J, He Z. Effects of Sc and Zr microalloying additions and aging time at 120 C on the corrosion behaviour of an Al–Zn–Mg alloy. Corrosion Science 2012;65:288-98.

[54] Fang H, Chao H, Chen K. Effect of Zr, Er and Cr additions on microstructures and properties of Al–Zn–Mg–Cu alloys. Materials Science and Engineering: A 2014;610:10-6.

[55] Au H. Pitting and crack initiation in high strength aluminum alloys for aircraft applications: Massachusetts Institute of Technology; 1996.

[56] Handbook A. Aluminum and aluminum alloys. ASM international 1993:117.

[57] Murray G, Lamb H, Godard H. Role of Iron in Aluminium on the Initiation of Pitting in Water. British Corrosion Journal 1967;2:216-8.

[58] Huan S, Wei C, Da S, Jun W, Sun B-d. Effects of silicon content on microstructure and stress corrosion cracking resistance of 7050 aluminum alloy. Transactions of Nonferrous Metals Society of China 2014;24:2307-13.

[59] Holroyd N. Environment-induced cracking of high-strength aluminum alloys. Environment-Induced Cracking of Metals (Houston, TX: NACE International, 1990) 1990:311.

[60] Song R, Dietzel W, Zhang B, Liu W, Tseng M, Atrens A. Stress corrosion cracking and hydrogen embrittlement of an Al–Zn–Mg–Cu alloy. Acta Materialia 2004;52:4727-43.

[61] Song M, Chen K. Effects of the enhanced heat treatment on the mechanical properties and stress corrosion behavior of an Al–Zn–Mg alloy. Journal of Materials Science 2008;43:5265-73.

[62] Buha J, Lumley R, Crosky A. Secondary ageing in an aluminium alloy 7050. Materials Science and Engineering: A 2008;492:1-10.

[63] De Ardo A, Townsend R. The effect of microstructure on the stress-corrosion susceptibility of a high purity Al− Zn− Mg alloy in a NaCl solution. Metallurgical Transactions 1970;1:2573-81.

[64] Puiggali M, Zielinski A, Olive J, Renauld E, Desjardins D, Cid M. Effect of microstructure on stress corrosion cracking of an Al-Zn-Mg-Cu alloy. Corrosion science 1998;40:805-19.

[65] Vasudevan AK, Doherty R. Grain boundary ductile fracture in precipitation hardened aluminum alloys. Acta metallurgica 1987;35:1193-219.

[66] Tsai T, Chuang T. Role of grain size on the stress corrosion cracking of 7475 aluminum alloys. Materials Science and Engineering: A 1997;225:135-44.

[67] Tsai T, Chuang T. Atmospheric stress corrosion cracking of a superplastic 7475 aluminum alloy. Metallurgical and Materials Transactions A 1996;27:2617-27.

[68] B C. Reducing the susceptibility of alloys, particularly aluminium alloys, to stress corrosion cracking. Google Patents; 1974.

[69] Park J. Influence of retrogression and reaging treatments on the strength and stress corrosion resistance of aluminium alloy 7075-T6. Materials Science and Engineering: A 1988;103:223-31.

[70] Viana F, Pinto A, Santos H, Lopes A. Retrogression and re-ageing of 7075 aluminium alloy: microstructural characterization. Journal of Materials Processing Technology 1999;92:54-9.

[71] Robinson J, Whelan S, Cudd R. Retrogression and re-aging of 7010 open die forgings. Materials science and technology 1999;15:717-24.

[72] Baydogan M, Cimenoglu H, Kayali ES, Rasty J. Improved resistance to stress-corrosion-cracking failures via optimized retrogression and reaging of 7075-T6 aluminum sheets. Metallurgical and Materials Transactions A 2008;39:2470-6.

[73] Li W-b, Pan Q-l, Xiao Y-p, He Y-b, Liu X-y. Microstructure and mechanical properties of Al-Zn-Cu-Mg-Sc-Zr alloy after retrogression and re-aging treatments. Journal of Central South University of Technology 2011;18:279-84.

[74] Rajan K, Wallace W, Beddoes J. Microstructural study of a high-strength stress-corrosion resistant 7075 aluminium alloy. Journal of Materials Science 1982;17:2817-24.

[75] Ferrer C, Koul M, Connolly B, Moran A. Improvements in strength and stress corrosion cracking properties in aluminum alloy 7075 via low-temperature retrogression and re-aging heat treatments. Corrosion 2003;59:520-8.

[76] Oliveira A, De Barros M, Cardoso K, Travessa D. The effect of RRA on the strength and SCC resistance on AA7050 and AA7150 aluminium alloys. Materials Science and Engineering: A 2004;379:321-6.

[77] Shastry C, Levy M, Joshi A. The effect of solution treatment temperature on stress corrosion susceptibility of 7075 aluminium alloy. Corrosion Science 1981;21:673-88.

[78] Joshi A, Shastry C, Levy M. Effect of heat treatment on solute concentration at grain boundaries in 7075 aluminum alloy. Metallurgical Transactions A 1981;12:1081-8.

[79] Li J-F, Peng Z-w, Li C-X, Jia Z-Q, Chen W-j, Zheng Z-Q. Mechanical properties, corrosion behaviors and microstructures of 7075 aluminium alloy with various aging treatments. Transactions of Nonferrous Metals Society of China 2008;18:755-62.

[80] Silva G, Rivolta B, Gerosa R, Derudi U. Study of the SCC Behavior of 7075 Aluminum Alloy After One-Step Aging at 163° C. Journal of materials engineering and performance 2013;22:210-4.

[81] Ou B-L, Yang J-G, Wei M-Y. Effect of homogenization and aging treatment on mechanical properties and stress-corrosion cracking of 7050 alloys. Metallurgical and Materials Transactions A 2007;38:1760-73.

[82] Magnin T. Recent advances in the environment sensitive fracture mechanisms of aluminium alloys. Materials Science Forum: Trans Tech Publ; 1996. p. 83-94.

[83] Hoeppner DW, Arriscorreta CA. Exfoliation corrosion and pitting corrosion and their role in fatigue predictive modeling: state-of-the-art review. International Journal of Aerospace Engineering 2012;2012.

[84] Braun R. Slow strain rate testing of aluminum alloy 7050 in different tempers using various synthetic environments. Corrosion 1997;53:467-74.

[85] Mueller M, Thompson A, Bernstein I. Stress corrosion behavior of 7075 aluminum in 1N aluminum chloride solutions. Corrosion 1985;41:127-36.

[86] Onoro J, Ranninger C. Stress-corrosion-cracking behavior of heat-treated Al− Zn− Mg− Cu alloy with temperature. Materials Science 1999;35:509-14.

[87] Kannan MB, Raja V, Mukhopadhyay A. Determination of true stress corrosion cracking susceptibility index of a high strength Al alloy using glycerin as the non-corrosive atmosphere. Scripta Materialia 2004;51:1075-9.

[88] Rout PK, Ghosh M, Ghosh K. Effect of solution pH on electrochemical and stress corrosion cracking behaviour of a 7150 Al–Zn–Mg–Cu alloy. Materials Science and Engineering: A 2014;604:156-65.

[89] Tromans D, Pathania R. The Electrochemical Society. Extended Abstracts1969.

[90] Liao H-L, Lin J-C, Lee S-L. Effect of pre-immersion on the SCC of heat-treated AA7050 in an alkaline 3.5% NaCl. Corrosion Science 2009;51:209-16.

[91] Deschamps A, Livet F, Brechet Y. Influence of predeformation on ageing in an Al–Zn–Mg alloy—I. Microstructure evolution and mechanical properties. Acta Materialia 1998;47:281-92.

[92] Waterloo G, Hansen V, Gjønnes J, Skjervold S. Effect of predeformation and preaging at room temperature in Al–Zn–Mg–(Cu, Zr) alloys. Materials Science and Engineering: A 2001;303:226-33.

[93] Wang D, Ni D, Ma Z. Effect of pre-strain and two-step aging on microstructure and stress corrosion cracking of 7050 alloy. Materials Science and Engineering: A 2008;494:360-6.

[94] Wang D, Ma Z, Gao Z. Effects of severe cold rolling on tensile properties and stress corrosion cracking of 7050 aluminum alloy. Materials Chemistry and Physics 2009;117:228-33.

[95] Nguyen D, Thompson A, Bernstein I. Microstructural effects on hydrogen embrittlement in a high purity 7075 aluminum alloy. Acta Metallurgica 1987;35:2417-25.

[96] Yue T, Dong C, Yan L, Man H. The effect of laser surface treatment on stress corrosion cracking behaviour of 7075 aluminium alloy. Materials Letters 2004;58:630-5.

[97] Venugopal A, Panda R, Manwatkar S, Sreekumar K, Krishna LR, Sundararajan G. Effect of micro arc oxidation treatment on localized corrosion behaviour of AA7075 aluminum alloy in 3.5% NaCl solution. Transactions of Nonferrous Metals Society of China 2012;22:700-10.

[98] Venugopal A, Panda R, Manwatkar S, Sreekumar K, Ramakrishna L, Sundararajan G. Effect of Microstructure on the Localized Corrosion and Stress Corrosion Behaviours of Plasma-Electrolytic-Oxidation-Treated AA7075 Aluminum Alloy Forging in 3.5 wt.% NaCl Solution. International Journal of Corrosion 2012;2012.

[99] Lim S, Kim S, Lee C-G, Kim S. Stress corrosion cracking behavior of friction-stir-welded Al 6061-T651. Metallurgical and Materials Transactions A 2005;36:1977-80.

[100] Surekha K, Murty B, Rao KP. Microstructural characterization and corrosion behavior of multipass friction stir processed AA2219 aluminium alloy. Surface and Coatings Technology 2008;202:4057-68.

[101] Paglia C, Carroll M, Pitts B, Reynolds T, Buchheit R. Strength, Corrosion and Environmentally Assisted Cracking of a 7075-T6 Friction Stir Weld. Materials Science Forum: Trans Tech Publ; 2002. p. 1677-84.

[102] Hu W, Meletis EI. Corrosion and environment-assisted cracking behavior of friction stir welded Al 2195 and Al 2219 alloys. Materials science forum: Trans Tech Publ; 2000. p. 1683-8.

[103] Ciompi E, Lanciotti A. Susceptibility of 7050-T7451 electron beam welded specimens to stress corrosion. Engineering fracture mechanics 1999;62:463-76.

[104] Hatamleh O, Singh PM, Garmestani H. Corrosion susceptibility of peened friction stir welded 7075 aluminum alloy joints. Corrosion Science 2009;51:135-43.

[105] Srinivasan PB, Dietzel W, Zettler R, Dos Santos J, Sivan V. Stress corrosion cracking susceptibility of friction stir welded AA7075–AA6056 dissimilar joint. Materials Science and Engineering: A 2005;392:292-300.

[106] Lumsden J, Mahoney M, Pollock G, Rhodes C. Intergranular corrosion following friction stir welding of aluminum alloy 7075-T651. Corrosion 1999;55:1127-35.

[107] Lucas KA, Clarke H. Corrosion of aluminium-based metal matrix composites: Research Studies Press; 1993.

[108] Monticelli C, Zucchi F, Brunoro G, Trabanelli G. Stress corrosion cracking behaviour of some aluminium-based metal matrix composites. Corrosion science 1997;39:1949-63.

[109] Shimizu Y, Nishimura T, Matsushima I. Corrosion resistance of Al-based metal matrix composites. Materials Science and Engineering: A 1995;198:113-8.

[110] Winkler S, Flower H. Stress corrosion cracking of cast 7XXX aluminium fibre reinforced composites. Corrosion science 2004;46:903-15.

[111] Tajally M, Huda Z, Masjuki H. A comparative analysis of tensile and impact-toughness behavior of cold-worked and annealed 7075 aluminum alloy. International journal of impact engineering 2010;37:425-32.

[112] Sundararajan G, Phani PS, Jyothirmayi A, Gundakaram RC. The influence of heat treatment on the microstructural, mechanical and corrosion behaviour of cold sprayed SS 316L coatings. Journal of materials science 2009;44:2320-6.

[113] Fjellsted J. Continuous casting. Model documentation COMSOL multiphysics Web 2011.

[114] Bartl J, Baranek M. Emissivity of aluminium and its importance for radiometric measurement. Measurement of Physical Quantities 2004;4:31-6.

[115] Panigrahi SK, Jayaganthan R. Effect of rolling temperature on microstructure and mechanical properties of 6063 Al alloy. Materials Science and Engineering: A 2008;492:300-5.

[116] Kassner M. Taylor hardening in five-power-law creep of metals and Class M alloys. Acta materialia 2004;52:1-9.

[117] Lawrence J, Evans D. An analysis of crack and porosity formation in laser surface treated magnesia partially stabilized zirconia (MgO-PSZ) and methods for alleviation. Lasers in Engineering 2007;17:255-71.

[118] Birbilis N, Cavanaugh M, Buchheit R. Electrochemical behavior and localized corrosion associated with Al 7 Cu 2 Fe particles in aluminum alloy 7075-T651. Corrosion Science 2006;48:4202-15.

[119] Ryan PJ, Prangnell S. Surface Treatment of Aluminium Aerospace Alloys Using Pulsed Laser and Electron Beam Systems: University of Manchester; 2007.

[120] Ryan P, Prangnell P. Grain structure and homogeneity of pulsed laser treated surfaces on Al-aerospace alloys and FSWs. Materials Science and Engineering: A 2008;479:65-75.

[121] Fribourg G, Deschamps A, Bréchet Y, Mylonas G, Labeas G, Heckenberger U, et al. Microstructure modifications induced by a laser surface treatment in an AA7449 aluminium alloy. Materials Science and Engineering: A 2011;528:2736-47.

[122] Padovani C, Davenport AJ, Connolly BJ, Williams SW, Siggs E, Groso A, et al. Corrosion protection of AA7449-T7951 friction stir welds by laser surface melting with an Excimer laser. Corrosion Science 2011;53:3956-69.

[123] Cheng Y, Chen Z, Wu H, Wang H. The corrosion behaviour of the aluminum alloy 7075/SiCp metal matrix composite prepared by spray deposition. Materials and Corrosion 2007;58:280-4.

[124] Yilbas B, Gbadebo S, Sami M. Laser heating: an electron-kinetic theory approach and induced thermal stresses. Optics and lasers in engineering 2000;33:65-79.

A- Corrosion behavior of the intermetallic particles on AA 7075-T6 alloy after immersion test in 0.1 M NaCl

Intermetallic Particles	Phase	E_{corr} (mV) (SCE)	I_{corr} (A/cm^2)	Behavior with respect to matrix	Comments
Al$_7$Cu$_2$Fe	S-phase	-551	-3.1 x 10-4	Cathodic	Constituent Particles
Al$_2$Cu	θ	-665	-4.7 x 10-4	Cathodic	Constituent
Al$_3$Fe	β	-539	-9.9 x 10-5	Cathodic	Constituent
Mg$_2$Si	β	-1538	1.9 x 10-4	Anodic	Precipitates and Constituent
MgZn$_2$	η	-1029	1.0 x 10-3	Anodic	Precipitates along grain boundaries
Matrix	α	-799	-8.1 x 10-5	Anodic	----

B- Physical properties of the elements in 7xxx alloys

Element	Zn	Mg	Cu	Fe	Cr	Si	Mn	Ti	Al
Wt. %	5.83	2.45	1.56	0.24	0.21	0.12	0.08	0.03	Bal.
Melting Point (K)	693	923	1358	1811	2180	1687	1519	1914	933.5
Boiling Point (K)	1180	1363	2835	3134	2944	3538	2334	3560	2792
Vapour Pressure.(Pa/K)	610	701	1509	1728	1656	1908	1228	1982	1482
Heat.of Vap.(kJ/mol)	123.6	128	300	340	339.5	359	221	425	294
Crystal Structure	HCP	HCP	FCC	BCC	BCC	DC	BCC	HCP	FCC

LIST OF PUBLICATIONS

International conferences

1. **International Conference on Advances in Manufacturing and Materials Engineering**, AMME, **NITK,** 2014, Influence of Cold Rolling and Annealing on the Tensile Properties of Aluminium 7075 Alloy .

2. **International Colloquium on Materials, Manufacturing and Metrology, ICMMM 2014**, August 8-9, 2014, **IIT Madras**, Chennai, India. Effect of Laser Surface Melting on Corrosion Behaviour of 7075 Aluminium Alloy.

3. **5th International and 26th All India Manufacturing Technology, Design and Research Conference AIMTDR 2014**, Department of Mechanical Engineering, **IIT Guwahati**, India. Improvement of Corrosion Resistance by Laser Surface Melting of 7075 Aluminum Alloy.

International Journal Publication

1. Rao, AC Umamaheshwer, et al. "**Influence of Cold Rolling and Annealing on the Tensile Properties of Aluminum 7075 Alloy.**" *Elesvier -Procedia Materials Sciences* (2014): 86-95.

2. RAO, AC UMAMAHESHWER, et al. "**Stress corrosion cracking behaviour of 7xxx aluminum alloys: A literature review**." *Transactions of Nonferrous Metals Society of China* 26.6 (2016): 1447-1471. (SCI Index)

3. Rao, AC Umamaheshwer, et al. "**Influence of diode laser surface melting on microstructure and corrosion resistance of 7075 aluminium alloy**." *International Journal of Microstructure and Materials Properties* 11.1-2 (2016): 85-104. (Scopus Index)

4. **Effect of Cold Rolling and subsequent Annealing on the Stress Corrosion Cracking Behavior of 7075 Aluminum Alloy**, *Iranian Journal of Science and Technology*.(under review). (SCI Index)

5. **Effect of Graphite Coating on Microstructure and Corrosion Properties of High Power Diode Laser Surface Melting of 7075 Aluminum Alloy**, *International journal of materials and product technology, Inderscience publishers* .(under review) (SCI Index)

6. **Experimental and Computational Analysis of High Power Laser Diode Beam Shape on the Thermal Stress and Melt Pool Characteristics,** *World Journal of Engineering*, .(under review) (Scopus Index).

CURRICULAM VITAE

1	Name	A C UMAMAHESHWER RAO
2	Date of birth	10 th July 1988
3	Educational qualifications	
	B.tech (2009)	Sri Indu College of Engg. & Tech, Sheriguda, Ibrahimpatnam, R.R.Dist.
	Specialization	Mechanical Engineering
	M.Tech (2012)	National Institute of Technology, Warangal
	Specialization	Materials technology
	Pursuing PhD	National Institute of Technology, Warangal
4	Research Interests	Materials Characterizations, Laser Surface Processing , Welding, Corrosion Behavior of metals, Numerical Simulations
5	Permanent Address	H.No:12-1-78, Plot No-14/A, Shivani Nagar colony, Bandlaguda, GSI post, Nagole, L.B.Nagar Hyderabad-500068.
	Email	Umamaheswar4@gmail.com Umamaheswar7@nitw.ac.in
	Contact number	9885696023